学位論文

Electronic Structure of Layered Transition-metal Dichalcogenide Superconductor $Ir_{1-x}Pt_xTe_2$ Studied by Photoemission Spectroscopy

(光電子分光による層状遷移金属ダイカルコゲナイド超伝導体 $Ir_{1-x}Pt_xTe_2$ の電子状態)

平成 27 年 12 月博士（理学）申請

東京大学大学院理学系研究科

物理学専攻　大槻　太毅

Electronic Structure of Layered Transition-metal Dichalcogenide Superconductor $Ir_{1-x}Pt_xTe_2$ Studied by Photoemission Spectroscopy

Thesis

Daiki Ootsuki

Department of Physics,
Graduate School of Science,
University of Tokyo

December 2015

Abstract

In transition-metal dichalcogenides, strong hybridization between d orbital of transition-metal and p orbital of ligand leads to rich and interesting physical properties such as unique charge modulation, excitonic insulator, and unconventional superconductivity. $IrTe_2$ exhibits a structural phase transition around 280K from a trigonal to a triclinic structure. At the low temperature phase, the stripe-type charge ordering with Ir - Ir dimers occurs. Pyon *et al.* and Yang *et al.* have discovered superconductivity in $Ir_{1-x}Pt_xTe_2$ when the stripe-type charge ordering is suppressed by Pt doping.

In this thesis, we have studied the electronic structure of layered transition-metal dichalcogenides superconductor $Ir_{1-x}Pt_xTe_2$ by core-level x-ray photoemission spectroscopy and angle-resolved photoemission spectroscopy. In Chapter 4, we have performed x-ray photoemission spectroscopy in order to investigate the core-level electronic structure of $Ir_{1-x}Pt_xTe_2$. At high temperature phase, the core-level photoemission spectra show that the valences of Ir and Te are close to Ir^{3+} and $Te^{1.5-}$, respectively. This indicates the strong hybridization between the Ir $5d$ and Te $5p$ orbitals. In going from the high temperature phase to the low temperature phase, the Ir $4f$ core-level splitting is clearly observed, suggesting the appearance of Ir^{4+}/Ir^{3+} charge ordering. In Chapter 5, we have performed the photon energy dependence of the angle-resolved photoemission spectroscopy using a synchrotron light source in order to investigate the valence-band electronic structure of $Ir_{1-x}Pt_xTe_2$ above and below the structural phase transition. At the high temperature phase, the three-dimensional Fermi surfaces of $Ir_{1-x}Pt_xTe_2$ derived from the Ir $5d$ and Te $5p$ orbitals are observed. Across the structural phase transition, the dimensionality of the Fermi surface drastically changes from three-dimensional to two-dimensional, which is basically consistent with the band structure calculation. In addition to the bulk state, we have found a novel one-dimensional band dispersion, which originates from the surface state. In Chapter 6, we have studied the spatial distribution of the electronic structure in $IrTe_2$ accompanied by the structural phase transition. The stripy domains are clearly observed at the low temperature phase. The domains consist of the dark and bright regions which can be assigned to the two phases with and without the stripe-type charge order, respectively. In Chapter 7, we have investigated the superconducting gap structure of $Ir_{0.95}Pt_{0.05}Te_2$, which shows the superconductivity at 3.1K, using a laser-based angle-resolved photoemission spectroscopy

and succeeded in directly observing the superconducting gap. The Fermi surface dependence of the superconducting gap clearly shows the anisotropic superconducting gap of $Ir_{0.95}Pt_{0.05}Te_2$. The unconventional superconductivity in $Ir_{0.95}Pt_{0.05}Te_2$ would be induced by the inter or intra band interaction and/or the spin-orbit interaction of Ir $5d$ and Te $5p$ orbitals.

Contents

Chapter 1

Introduction

The discovery of high-T_c superconductivity in cuprates and iron pnictides or chalcogenides has generated interest in understanding the interplay between the superconductivity and the other ordered states, for example antiferromagnetism, orbital or charge order, and structural transition, etc. These ordered states in the vicinity of the superconductivity imply the importance of spin-charge-orbital degrees of freedom. In many of the high-Tc superconductors, chemical doping suppresses the ordered state and induces superconductivity. The important issues of how these other ordered states compete or coexist with superconductivity is still being debated.

Transition-metal (TM) dichalcogenides with MX_2, where M is a transition-metal in group 4-12 elements, and X is a chalcogen in group 16 elements, are typical examples that the charge modulation such as charge density wave competes or coexists with superconductivity. 1T-type (CdI_2-type) and 2H type (MoS_2-type) are well known as crystal structures of the transition-metal dichalcogenides. The 1T- and 2H-type transition-metal dichalcogenides are layered compounds which are made up of edge-sharing MX_6 octahedra and face-sharing MX_6 prisms as shown in Figs. 1.1(a) and (b). Both of them consist of a triangular lattice of M ions. Considering the octahedral coordination for the M ion of the 1T-type structure, the five TM d orbitals degenerate in spherical symmetry are split into doubly degenerate e_g ($x^2 - y^2$, $3z^2 - r^2$) orbitals and triply degenerate t_{2g} (xy, yz, zx) orbitals in octahedral symmetry. In the octahedral symmetry, the t_{2g} orbitals are located in lower energy than the e_g orbitals as shown in Fig. 1.1 (a). On the other hand, the d orbitals in the 2H-type structure are split into single a_{1g} ($3z^2 - r^2$) orbital, doubly degenerate e_g ($x^2 - y^2$, xy) orbitals, and doubly degenerate e_g (xz, yz) orbitals as shown in Fig 1.1 (b). These d orbitals hybridize with the p or s orbitals of ligand. Figures 1.1 (c) and (d) show the schematics of band dispersions of typical transition metal dichalcogenides 1T-MX_2 (M= Ti and Ta, X= S, Se, and Te). According

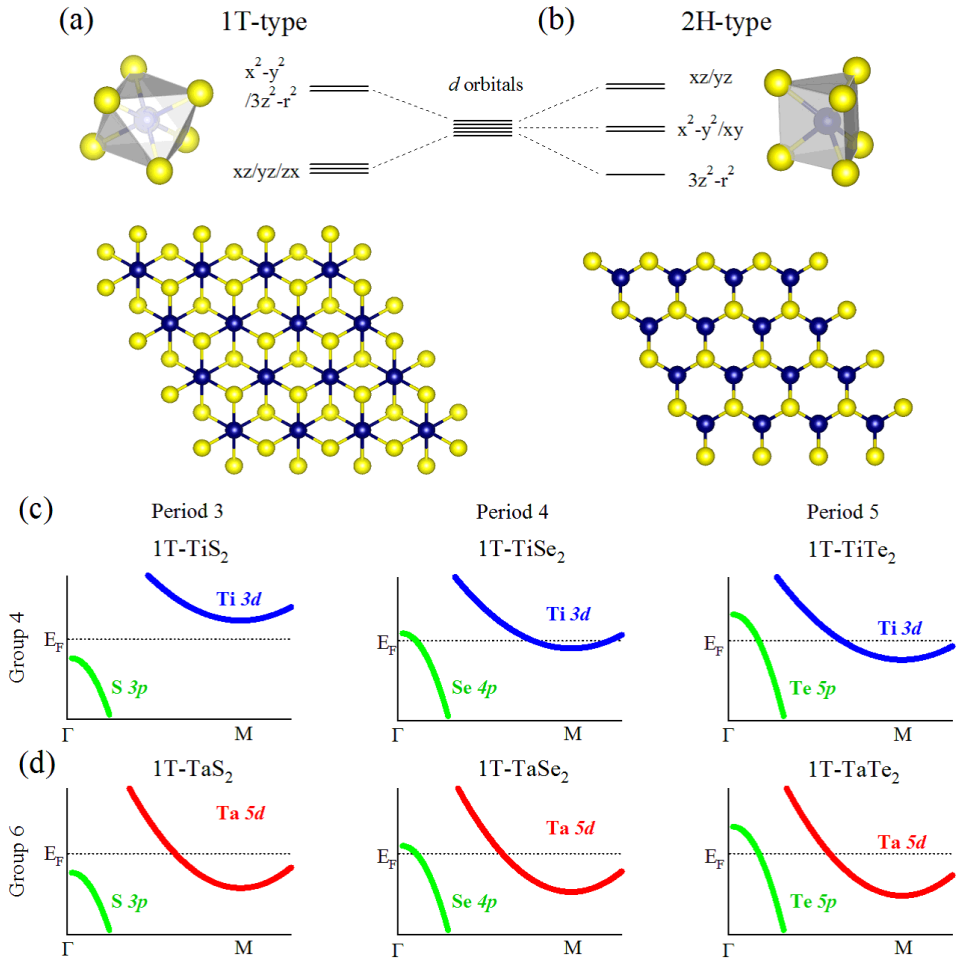

Figure 1.1: Schematics of ligand field effect and crystal structures of (a) 1T-type and (b) 2H-type transition-metal dichalcogenide. Schematics of band dispersions of (c) 1T-TiX_2 and (d) 1T-TaX_2 (X= Ligand).

to the ligand elements, the overlap between the d orbitals of transition metal and the p orbitals of ligand increases in going from S to Se to Te. The strength of hybridization can be tuned by a charge-transfer energy Δ from the ligand p orbitals to the transition-metal d orbitals. In general, the charge-transfer energy Δ tends to decrease in going from oxides to chalcogenides [1]. As a result, the density of states near the Fermi level is contributed by the p orbtials of ligand as well as the d orbtials of transition-metal. Therefore, the inter or intra band interaction, which includes not only the d orbitals of transition-metal but also the p orbitals of ligand, leads to rich and interesting physical properties such as unique charge modulation, excitonic insulator, and unconventional superconductivity. Here, we summarize the physical properties of transition-metal dichalcogenides in Table 1.1.

Table 1.1: Transition-metal dichalcogenides with charge density wave and superconductivity. Here, T_{CDW} and T_{SC} are the transition temperature of charge density wave and superconductivity, respectively.

Group	Compound	T_{CDW}	Superstructure	T_{SC}	Ref.
4	1T-$TiSe_2$	202K	$2a \times 2a \times 2c$	1.8K[1],4.1K[2]	[2–4]
5	1T-VS_2	305K	$3\sqrt{3}a \times 3\sqrt{3}a$	-	[5]
5	1T-VSe_2	112K	$4a \times 4a \times 3.3c$	-	[6]
5	1T-TaS_2	543,350,183K	$\sqrt{13}a \times \sqrt{13}a$	-	[7]
5	1T-$TaSe_2$	473K	$\sqrt{13}a \times \sqrt{13}a$	-	[8]
5	1T-$TaTe_2$	170K	$3a$	-	[9]
5	2H-TaS_2	70K	$3a \times 3a$	0.8K, 4.5K[2]	[10–12]
5	2H-$TaSe_2$	122, 90K	$3a \times 3a$	-	[13]
5	2H-$NbSe_2$	33K	$3a \times 3a$	7.2K	[13,14]
6	1T-$CrSe_2$	190K	$3a \times 3a \times 3c$	-	[15]
9	1T-$IrTe_2$	280K	$5a \times b \times 5c$	- ,3.1K[2]	[16,17]
10	1T-$PdTe_2$	-	-	1.7K, 2.4K[2]	[18,19]
11	1T-$AuTe_2$	-	$2.1a \times b \times 2.2c$	2.3K[1], 4.0K[2]	[20,21]

[1]Under high pressure, [2] Chemical doping or intercalation

In this thesis, we focus on the transition-metal dichalcogenide superconductor $Ir_{1-x}Pt_xTe_2$. The parent material $IrTe_2$ exhibits the structural phase transition accompanied by the stripe-type charge modulation with Ir-Ir dimers [17,22,23].

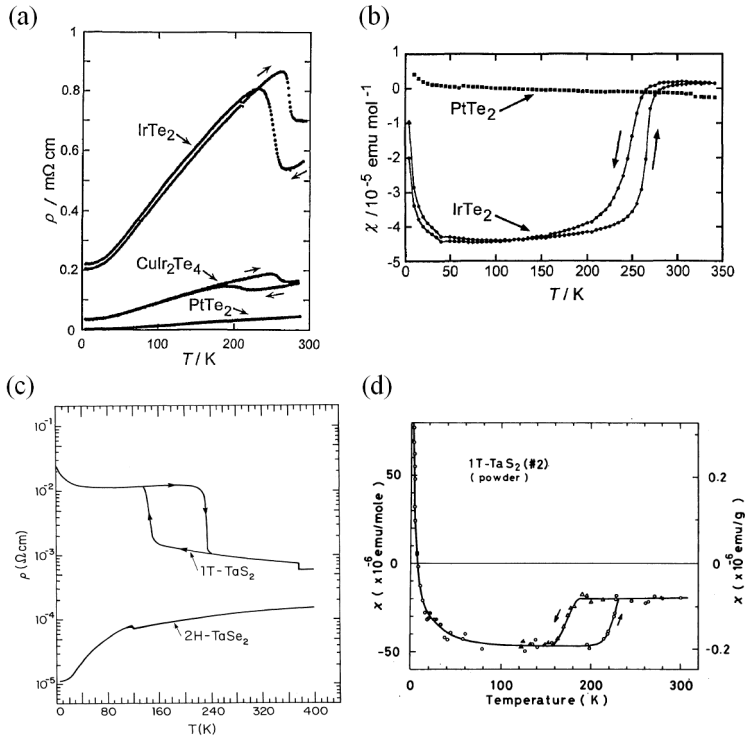

Figure 1.2: Electronic resistivity of (a) $IrTe_2$ and (c) 1T-TaS_2. Magnetic susceptibility of (b) $IrTe_2$ and (d) 2H-$TaSe_2$. [16, 25, 26]

In Figs. 1.2 (a) and (b), the temperature dependences of electronic resistivity and magnetic susceptibility for $IrTe_2$ show a hump and a step-like reduction across the structural phase transition, respectively [16]. These behaviors are interpreted in terms of CDW instability and often observed in the typical transition-metal dichalcogenides in Figs. 1.2 (c) and (d) [16, 25, 26]. Furthermore, the superconductivity is observed in $IrTe_2$, when the structural phase transition is suppressed by chemical substitution or intercalation [17, 21, 24]. The chemical intercalated $IrTe_2$ is very similar to the superconductor Cu_xTiSe_2 [4].

In the transition-metal disulfides/diselenides such as TaS_2, $TaSe_2$, $TiSe_2$, the charge density wave can be described by three modulation vectors. By contrast, the stripe-type charge-orbital ordering of $IrTe_2$ is sufficiently characterized by a single modulation vector $q = (1/5, 0, -1/5)$. Interestingly, the stripe-type charge modulation of $IrTe_2$ is robust under high pressure. This behavior of $IrTe_2$ is completely different from the other transition-metal disulfides or diselenides. Thus, the unique charge modulation with Ir-Ir dimers is realized in $Ir_{1-x}Pt_xTe_2$.

Since the spin-orbit interaction is proportional to the atomic number Z, the effect of spin-orbit interaction cannot be ignored in $Ir_{1-x}Pt_xTe_2$ and may introduce exotic superconducting state. Moreover, $Ir_{1-x}Pt_xTe_2$ has the small charge-transfer energy as we discussed above. Therefore, the density of states near the Fermi level could be contributed by the Te $5p$ orbtials of ligand as well as the Ir $5d$ orbtials.

In order to investigate the electronic structure of $Ir_{1-x}Pt_xTe_2$, we have performed core-level x-ray photoemission spectroscopy (XPS) and angle-resolved photoemission spectroscopy (ARPES). First, the other experimental and theoretical studies for $Ir_{1-x}Pt_xTe_2$ and the general principles of experimental methods will be briefly reviewed in Chapters 2 and 3. In Chapter 4, we present the results of the core-level photoemission spectroscopy. In Chapter 5, we show the ARPES results of $Ir_{1-x}Pt_xTe_2$. We discuss the 3-dimensional nature of $Ir_{1-x}Pt_xTe_2$ and the effects of spin-orbit interaction. In Chapter 6, we show the spatial distribution of the photoemission spectrum for $IrTe_2$ with the structural phase transition. The stripe domains are clearly observed below the structural phase transition. In Chapter 7, we show the Laser-ARPES results of $Ir_{1-x}Pt_xTe_2$. We observed the anisotropic superconduting gap. Unifying those results, summary and concluding remarks are given in Chapter 8.

References

[1] A. E. Bocquet, A. Fujimori, T. Mizokawa, T. Saitoh, H. Namatame, S. Suga, N. Kimizuka, Y. Takeda, and M. Takano, Phys. Rev. B **45** 1561 (1992).

[2] F. J. Di Salvo, D. E. Moncton, and J. V. Waszczak Phys. Rev. B **14**, 4321 (1976).

[3] A. F. Kusmartseva, B. Sipos, H. Berger, L. Forro, and E. Tutis Phys. Rev. Lett. **103**, 236401 (2009).

[4] E. Morosan, H. W. Zandbergen, B. S. Dennis, J. W. G. Bos, Y. Onose, T. Klimczuk, A. P. Ramirez, N. P. Ong and R. J. Cava, Nature Physics **2**, 544-550 (2006)

[5] T. Tsuda, H. Yasuoka, Y. Kitaoka, and F. J. Di Salvo, J. Magn. Magn. Mater. $\mathbf{31-34}$, 1101 (1983).

[6] A. H. Thompson and B. G. Silbernagel, Phys. Rev. B **19**, 3420 (1979).

[7] S. C. Bayliss, A. M. Ghorayeb, and D. R. P. Guy, J. Phys. C : Solid State Physics, **17**, 21 (1984).

[8] J. A. Wilson, F.J. DiSalvo, and S. Mahasan, Adv. Phys. **24**, 117 (1975).

[9] T. Sörgel, J. Nuss, U. Wedig, R.K. Kremer, M. Jansen, Materials Research Bulletin **41** 987-1000 (2006).

[10] J. P. Tidman, O. Singh, A. E. Curzon, and R. F. Frindt, Philosophical Magazine, **30** 5, (1975).

[11] 9S. Nagata, T. Aochi, T. Abe, S. Ebisu, T. Hagino, Y. Seki, and K. Tsutsumi, J. Phys. Chem. Solids **53**, 1259 (1992).

[12] K. E. Wagner, E. Morosan, Y. S. Hor, J. Tao, Y. Zhu, T. Sanders, T. M. McQueen, H. W. Zandbergen, A. J. Williams, D. V. West, and R. J. Cava, Phys. Rev. B **78**, 104520 (2008).

[13] D. E. Moncton, J. D. Axe, and F. J. Di Salvo, Phys. Rev. B **16** 801 (1977).

[14] J. A. Wilson, F. J. Di Salvo, and S. Mahajan, Adv. Phys. **24**, 117 (1975).

[15] S. Kobayashi, H. Ueda, D. Nishio-Hamane, C. Michioka, and K. Yoshimura, Phys. Rev. B **89**, 054413 (2014).

[16] N. Matsumoto, K. Taniguchi, R. Endoh, H. Takano, and S. Nagata, J. Low Temp. Phys. **117**, 1129 (1999).

[17] S. Pyon, K. Kudo, and M. Nohara, J. Phys. Soc. Jpn. **81**, 053701 (2012).

[18] C. J. Raub, V. B. Compton, T. H. Geballe, B. T. Matthias, J. P. Maita, and G. W. Hull, J. Phys. Chem. Solids **26**, 2051 (1965).

[19] Gihun Ryu, J. Supercond. Nov. Magn. **28**, 3275-3280 (2015)

[20] G. Tunell and L. Pauling, Acta Crystallogr. **5**, 375 (1952).

[21] K. Kudo, H. Ishii, M. Takasuga, K. Iba, S. Nakano, J. Kim,A. Fujiwara, and M. Nohara, J. Phys. Soc. Jpn. **82**, 063704 (2013).

[22] T. Toriyama, M. Kobori, T. Konishi, Y. Ohta, K. Sugimoto, J. Kim, A. Fujiwara, S. Pyon, K. Kudo, and M. Nohara, J. Phys. Soc. Jpn. **83**, 033701 (2014).

[23] G. L. Pascut, K. Haule, M. J. Gutmann, S.A. Barnett, A. Bambardi, S. Artyukhin, T. Birol, D. Vanderbilt, J. J. Yang, S-W. Cheong, and V. Kiryukhin, Phys. Rev. Lett. **112**, 086402 (2014).

[24] M. Kamitani, . S. Bahramy, . Arita, S. Seki, T. Arima, Y. Tokura, and S. Ishiwata Phys. Rev. B **87**, 180501 (R) (2013)

[25] R. V. Coleman, B. Drake, P. K. Hansma, and G. Slough, Phys. Rev. Lett. **55**, 4 (1985)

[26] R. Inada, Y. Onuki, S. Tanuma, J. Phys. Soc. Jpn. **50**, 4 (1981)

Chapter 2

Physical properties of $Ir_{1-x}Pt_xTe_2$

2.1 Structural phase transition of $IrTe_2$

A layered transition-metal (TM) dichalcogenide $IrTe_2$ is a typical layered compound, which has a triangular lattice of Ir ions by edge-sharing $IrTe_6$ octahedra as shown in Fig. 2.1. $IrTe_2$ exhibits a structural phase transition from a trigonal CdI_2-type structure to a triclinic $P\bar{1}$ structure accompanied by anomalies of electronic resistivity and magnetic susceptibility [1–3]. The temperature dependence of the electronic resistivity and the magnetic susceptibility are displayed in Fig. 2.2 [3]. The electronic resistivity shows a hump-structure at 275K on cooling, and at 280K on heating, indicating the metal to metal transition. On the other hands, the magnetic susceptibility shows a step-like structure and a broad range hysteresis between 100K and 280K. Toriyama *et al.* and Pascut *et al.* have revealed the presence of Ir-Ir dimers with a modulation vector $q_{1/5} = (1/5, 0, -1/5)$ by synchrotron radiation x-ray diffraction [4, 6, 7]. Figure 2.1 (b) shows the crystal structure of $IrTe_2$ at the low temperature phase.

Recently, x-ray diffraction, scanning tunneling microscopy (STM), and de Haas-van Alphen (dHvA) oscillation have observed the different dimer patterns from the known $q_{1/5}$ type. K. -T. Ko *et al.* have proposed that the periodicity of superstructure changes from $q_{1/5}$ to $q_{1/8}$ with decrease of temperature using the x-ray diffraction measurement [12]. The dHvA oscillation study has revealed the $q_{1/5}$ and $q_{1/8}$ type superstructures [13, 14]. In addition to these results, the various superstructures of the charge modulation vector $q_n = (3n+2)^{-1}$ are identified by the STM measurements [16–18]. The periodicity of the modulation vector at the low temperature phase depends on the postcooling procedures in the crystal growth, either quenching or slow cool-

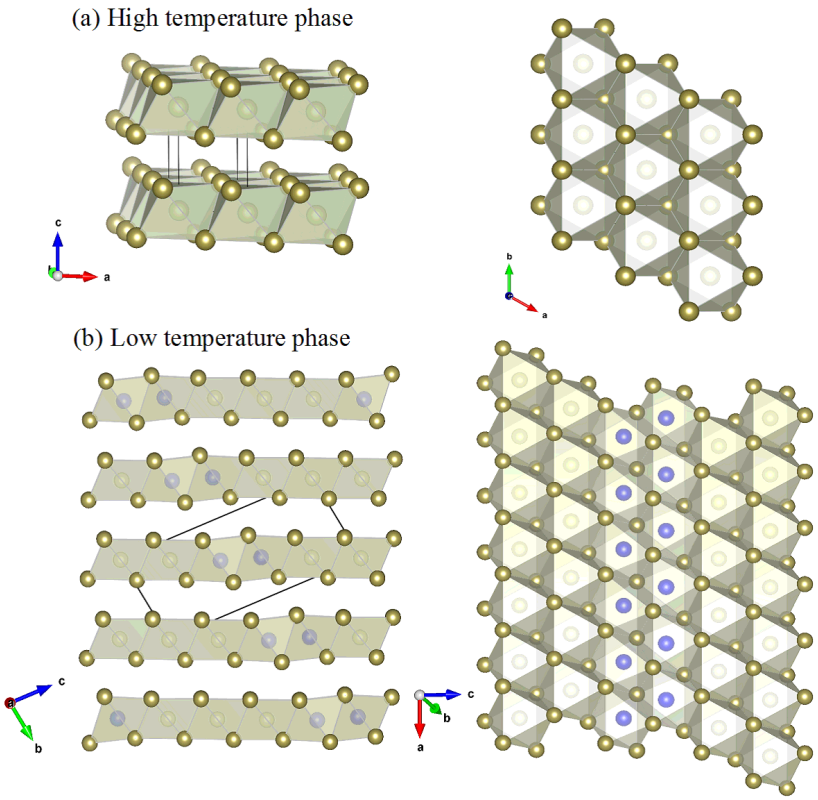

Figure 2.1: (a) Crystal structure of high temperature phase. (b) Crystal structure of low temperature phase [2, 4] visualized by using the software package VESTA [5]. Black box line indicates the unit cell.

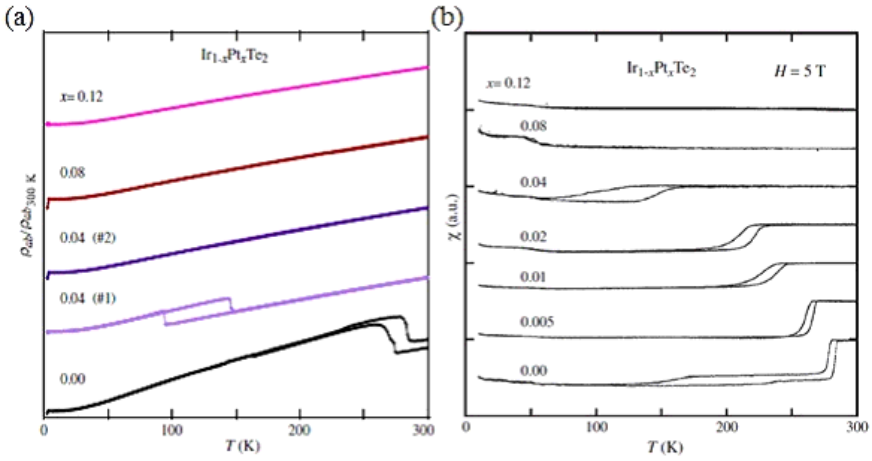

Figure 2.2: Temperature dependence of (a) electronic resisitivity and (b) magnetic susceptibility of $Ir_{1-x}Pt_xTe_2$ [3]

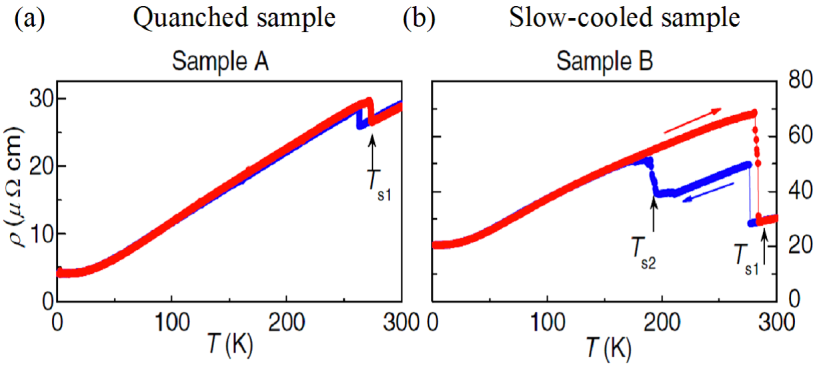

Figure 2.3: Electronic resistivities of (a) Quanched sample and (b) Slow cooled sample [13].

ing, while these samples are synthesized the Te-flux method [13]. These two types of $IrTe_2$ show the completely different electronic resistivity as shown in Fig. 2.3. It should be noted that the electronic resistivity of our sample, which we used in this study, is close to that of the quenched sample.

2.2 Band-structure calculation of $IrTe_2$

Figures 2.4 (a) and (b) show the band structure calculation of the high temperature phase and the low temperature phase, respectively [4]. The calculated Fermi surfaces of $IrTe_2$ at the high temperature phase consist of two hole-like bands and reveal the strongly three-dimensional structure, suggesting the rich dispersion along the k_z direction. The three-dimensionality of Fermi surface implies that the large Te - Te interaction between the layers. Indeed, Te $5p$ orbitals mainly contribute to the density of states at Fermi level [15]. Cao *et al.* have proposed that the calculated phonon dispersion of $IrTe_2$ at the high temperature phase does not show the Kohn anomalies [21]. By contrast, the tilted two-dimensional Fermi surfaces emerge at low temperature phase, which indicates the switching of the conducting planes by the formation of Ir-Ir dimers as shown in Fig. 2.4. Fermi surfaces of the low temperature phase are composed of the warped quasi-one dimensional sheets and the small cylindrical sheets in Fig. 2.4. The partial density of states at low temperature phase exhibits the bonding and anti-bonding states derived from the Ir-Ir dimers [7].

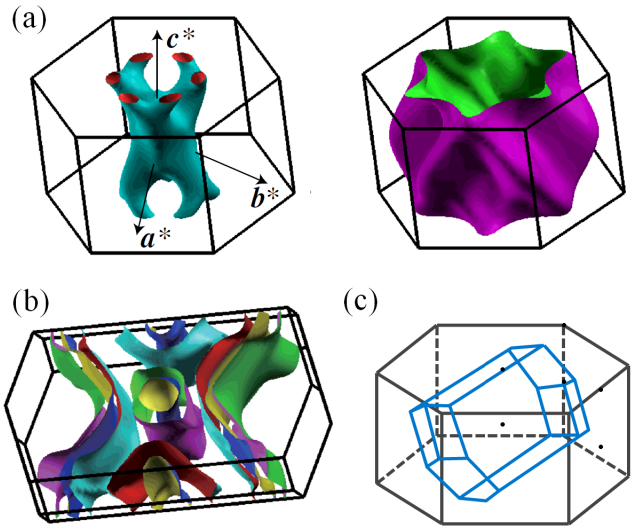

Figure 2.4: Calculated Fermi surfaces for (a) the high temperature phase and (b) the low temperature phase. Relation between the high temperature phase (black) and the low temperature phase (blue). [4]

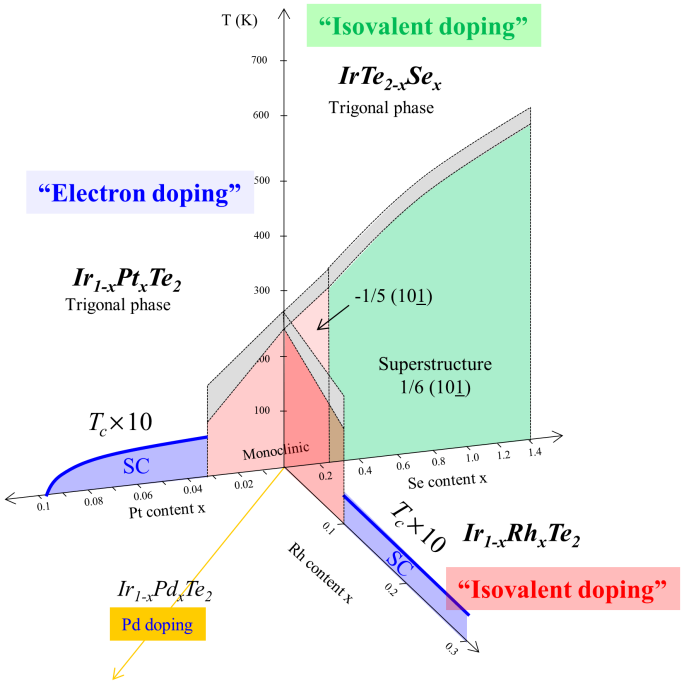

Figure 2.5: Schematic phase diagram of $IrTe_2$

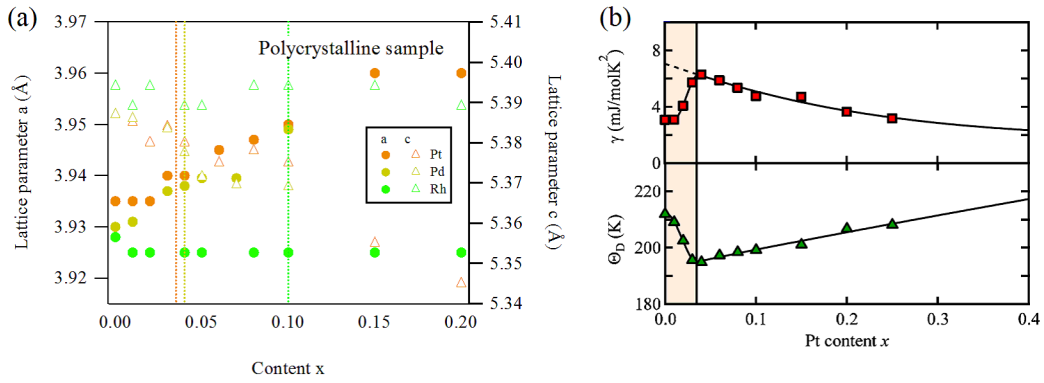

Figure 2.6: (a) Lattice parameters at 300K as a function of x for $Ir_{1-x}Pt_xTe_2$, $Ir_{1-x}Pd_xTe_2$, and $Ir_{1-x}Rh_xTe_2$ [2,3,6,8]. (b) Electronic specific heat coefficient γ and Debye temperature Θ_D for $Ir_{1-x}Pt_xTe_2$ as a function of x [2].

2.3 Mechanism of structural phase transition in $IrTe_2$

$IrTe_2$ exhibits the structural phase transition with the anomalies of electronic resistivity and magnetic susceptibility. The hump structure of electronic resistivity and the step-like reduction of the magnetic susceptibility with the structural phase transition are often observed in the charge density wave (CDW) materials. Yang *et al.* have suggested that the structural phase transition is driven by Fermi surface instabilities of Ir $5d$ orbitals [6]. However, the gap opening expected for the CDW was not observed in optical conductivity and angle-resolved photoemission spectroscopy [2, 22] which is consistent with NMR spectra [19]. A number of different mechanisms, including the orbital-induced Peierls instability [20, 22], the local bonding instabilities of Te $5p$ orbitals [2,9,11,21], the van Hove singularity at the Fermi level [23],the formation of Ir-Ir dimers [4,7,17], and the order-disorder transition [24], have been proposed to explain the origin of the structural phase transition. However, the driving force of the structural phase transition is still controversial.

2.4 Superconductivity in $Ir_{1-x}Pt_xTe_2$

Pyon *et al.* and Yang *et al.* have discovered superconductivity in $IrTe_2$ when the structural phase transition is suppressed by Pt or Pd substitution for Ir or intercalation of Pd [2,3,6]. Superconductivity also emerges by Rh substitution or Cu intercalation [8,9]. The superconducting temperature T_c of $Ir_{1-x}Pt_xTe_2$

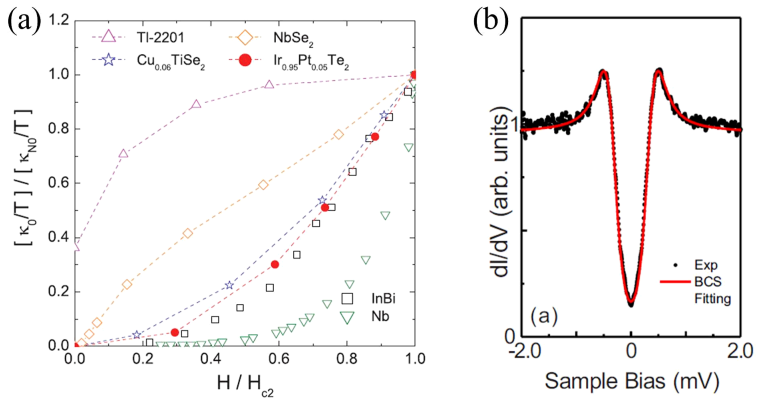

Figure 2.7: (a) Field dependence of normalized residual liner term κ_0/T, (b) Typical STS spectrum at 0.4K [25, 26]

reaches maximum of $\sim$ 3.1K for x=0.04. In contrast, the intercalation of Mn, Fe, Co, and Ni destroys not only superconductivity but also the structural transition [10]. The structural phase transition temperature increases with the anion-substitution or the application of hydrostatic pressure [11]. This behavior contrasts with $TiSe_2$, which shows that the pressure suppresses the structural phase transition and induces superconductivity. A phase diagram of the substituted or intercalated $IrTe_2$ is schematically presented in Fig. 2.5. Figure 2.6 (a) shows the lattice parameters a and c of polycrystalline $Ir_{1-x}Pt_xTe_2$, $Ir_{1-x}Pd_xTe_2$, and $Ir_{1-x}Rh_xTe_2$ as a function of x. The lattice parameters a (c) for $Ir_{1-x}Pt_xTe_2$ and $Ir_{1-x}Pd_xTe_2$ increase (decrease) monotonically, while that of $Ir_{1-x}Rh_xTe_2$ does not change appreciably with x. Interestingly, the doping level of Rh is three times higher than that of Pt in order to suppress the structural phase transition [8]. This suggests that the suppression of the structural phase transition is related to the change of the volume of the unit cell. The electronic specific heat coefficient γ and the Debye temperature Θ_D show the peak and the dip structure, indicating the phonon softening. In addition, the value of $\Delta C_p(T_c)/\gamma T_c$ $\sim$1.5 for $Ir_{1-x}Pt_xTe_2$ estimated by specific heat jump at T_c is comparable to the BCS weak coupling limit $\sim$1.43. Thermal conductivity measurement shows that the field dependence of normalized residual liner term κ_0/T is similar to that of s-wave superconductor $Cu_{0.06}TiSe_2$, suggesting the nodeless superconductivity in Ir_{1-x} Pt_x Te_2 [25]. These results are consistent with the superconducting gap measurement by scanning tunneling microscopy and spectroscopy (STM/STS) [26].

References

[1] N. Matsumoto, K. Taniguchi, R. Endoh, H. Takano, and S. Nagata, J. Low Temp. Phys. **117**, 1129 (1999).

[2] S. Pyon, K. Kudo, and M. Nohara, J. Phys. Soc. Jpn. **81**, 053701 (2012).

[3] S. Pyon, K. Kudo, and M. Nohara, Physica C **494**, 80-84 (2013)

[4] T. Toriyama, M. Kobori, T. Konishi, Y. Ohta, K. Sugimoto, J. Kim, A. Fujiwara, S. Pyon, K. Kudo, and M. Nohara, J. Phys. Soc. Jpn. **83**, 033701 (2014).

[5] K. Homma and F. Izumi, J. Appl. Crystallogr. **44**, 1272 (2011).

[6] J. J. Yang, Y. J. Choi, Y. S. Oh, A. Hogan, Y. Horibe, K. Kim, B. I. Min, and S-W. Cheong, Phys. Rev. Lett. **108**, 116402 (2012).

[7] G. L. Pascut, K. Haule, M. J. Gutmann, S.A. Barnett, A. Bambardi, S. Artyukhin, T. Birol, D. Vanderbilt, J. J. Yang, S-W. Cheong, and V. Kiryukhin, Phys. Rev. Lett. **112**, 086402 (2014).

[8] K. Kudo, M. Kobayashi, S. Pyon, and M. Nohara, J. Phys. Soc. Jpn. **82** 085001 (2013)

[9] M. Kamitani, . S. Bahramy, . Arita, S. Seki, T. Arima, Y. Tokura, and S. Ishiwata Phys. Rev. B **87**, 180501 (R) (2013)

[10] J. -Q. Yan, . B. Saparov, A. S. Sefar, H. Yang, H. . Cao, H. D. Zhou, B. C. Sales, and D. G. Mandrus, Phys. Rev. B **88**, 134502 (2013)

[11] Yoon Seok Oh, J. J. Yang, Y. Horibe, and S. -W. Cheong, Phys. Rev. Lett. **110**, 127209 (2013)

[12] K. -T. Ko, H. -H. Lee, D.-H. Kim, J.J. Yang, S. -W. Cheong, M. J. Eom, J. S. Kim, R. Gammag, K. -S. Kim, T. -H. Kim, H. -W. Yeom, T. -Y. Koo, H. -D. Kim, and J. -H. Park, Nature Communications **6**, 7342 (2015)

[13] Man Jin Eom, Kyoo Kim, Y. J. Jo, J. J. Yang, E. S. Choi, B. I. Min, J. -H. Park, S. -W. Cheong, and Jun Sung Kim, Phys. Rev. Lett. **113**, 266406 (2014)

[14] S. F. Blake, M. D. Watson, A. McCollam, S. Kasahara, R. D. Johnson, A. Narayanan, G. L. Pascut, K. Haule, V. Kiryukhin, T. Yamashita, D. Watanabe, T. Shibauchi,Y. Matsuda, and A. I. Coldea, Phys. Rev. B **91**,121105 (R) (2015)

[15] A. F. Fang, G. Xu, T. Dong, P. Zheng, and N. L. Wang, Sci. Rep. **3**, 1153(2012).

[16] Pin-Jui. Hsu, Tobias Mauerer, Matthias Vogt, J. J. Yang, Yoon Seok Oh, S. -W. Cheong, Matthias Bode, and Weida Wu, Phys. Rev. Lett. **111**, 266401 (2013)

[17] H. S. Kim, T. Kim, J. J. Yang, S. -W. Cheong, and H. W. Yeom, Phys. Rev. B **90**, 201103 (R) (2014)

[18] Q. Li, W. Lin, J. Yan, Z. Chen, A. G. Gianfrancesco, D. J. Singh, D. Mandrus, S. V. Kalinin, and M. Pan, Nature Communications **5**, 5358 (2014)

[19] K. Mizuno, K. Magishi, Y. Shinonome, T. Saito, K. Koyama, N. Matsumoto, and S. Nagata, Physica B **312**, 818 (2002).

[20] D. Ootsuki, Y. Wakisaka, S. Pyon, K. Kudo, M. Nohara, M. Arita, H. Anzai, H. Namatame, M. Taniguchi, N. L. Saini, and T. Mizokawa, Phys. Rev. B **86**, 014519 (2012).

[21] H. Cao, B. C. Chakoumakos, X. Chen, J. Yan, M. A. McGuire, H. Yang, R. Custelcean, H. Zhou, D. J. Singh, and D. Mandrus, Phys. Rev. B **88**, 115122 (2013)

[22] D. Ootsuki, S. Pyon, K. Kudo, M. Nohara, M. Horio, T. Yoshida, A. Fujimori, M. Arita, H. Anzai, H. Namatame, M. Taniguchi, N. L. Saini, and T. Mizokawa, J. Phys. Soc. Jpn. **82**, 093704 (2013).

[23] T. Qian, H. Miao, Z. J. Wang, X. Shi, Y. B. Huang, P. Zhang, N. Xu, L. K. Zeng, P. Richard, M. Shi, G. Xu, X. Dai, Z. Fang, A. F. Fang, N. L. Wang, and H. Ding, New J. Phys. **16**, 123038 (2014)

[24] B. Joseph, M. Bendele, L. Simonelli, L. Maugeri, S. Pyon, K. Kudo, M. Nohara, T. Mizokawa, and N. L. Saini, Phys. Rev. B **88**, 224109 (2013).

[25] S. Y. Zhou, Z. L. Li, B. Y. Pan, X. Qiu, J. Pan, X. C. Hong, Z. Zhang, A. F. Fang, N. L. Wang, and S. Y. Li, EPL **104**, 27010 (2013)

[26] D. J. Yu, F. Yang, Lin Miao, C. Q. Han, Meng -Yu Yao, Fengfeng Zhu, Y. R. Song, K. F. Zhang, J. F. Ge, X.Yao, Z. Q. Zou, Z. J. Li,B. F. Gao, Canhua Liu, D. D. Guan, C. L. Gao, Dong Qian, and Jin-feng Jia, Phys. Rev. B **89**, 100501 (R) (2014)

Chapter 3

Experimental methods and principles

In this chaper, we describe the general principles and experimental setup of photoemission spectoscopy [1–3].

3.1 Principle of photoemission spectroscopy

Photoemission spectroscopy is a very effective technique of measurement that can directly observe the electronic structure of materials. The method of photoemission spectroscopy employs an external photoelectric effect that a solid emits electrons when the surface of solid is irradiated with sufficiently high energy photon $h\nu$. The energy conservation rule is held which gives a relationship between the kinetic energy E^v_{kin} of the emitted electron in the vacuum, the photon energy $h\nu$, the work function Φ of the surface, and the binding energy of the electron in the solid E_B. The kinetic energy E^v_{kin} is writtten as

$$E^v_{kin} = h\nu - E_B - \Phi. \tag{3.1}$$

In actural experiments, the kinetic energy E_{kin} measured from E_F rather than E^v_{kin} is directly observed. Therefore, it is convenient to use

$$E_{kin} = h\nu - E_B. \tag{3.2}$$

One can plot the count rate of photoelectrons as a function of E_B that corresponds to the energy distribution of occupied states such as valence band and core-levels as shown in Fig. 3.1. In the one-electron approximation, the binding energy E_B takes the form

$$E_B = -\epsilon_k \tag{3.3}$$

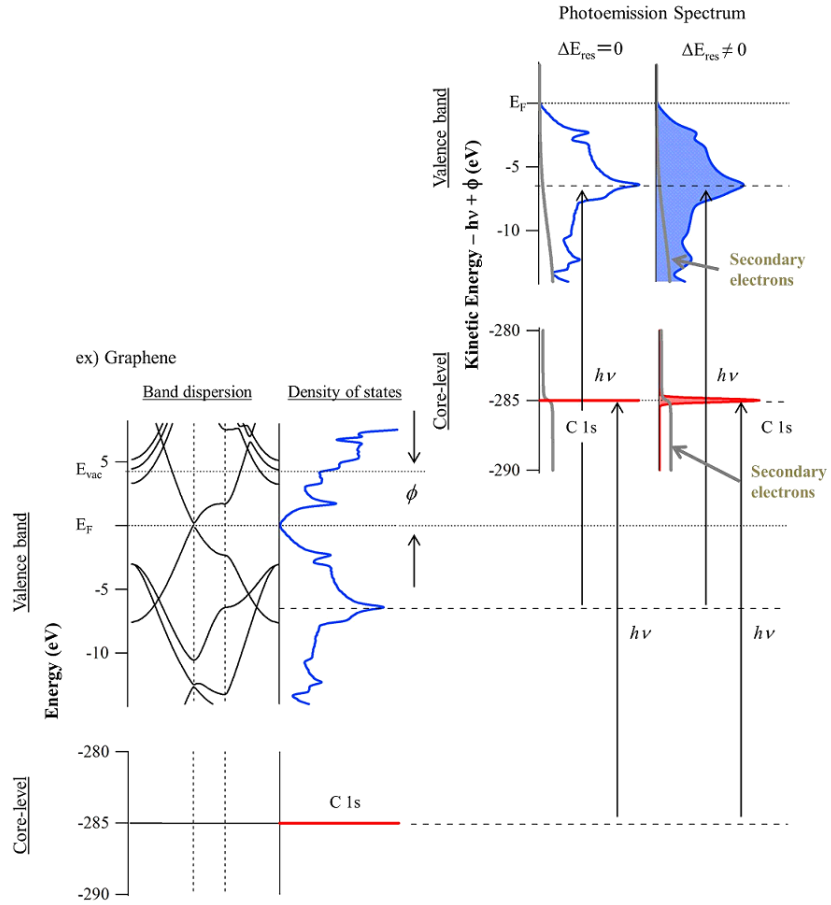

Figure 3.1: Schematic diagram of photoemission spectroscopy [1].

where ϵ_k is Hatree-Fock orbital energy. This relationship is called *Koopman's theorem*.

3.2 Spectral function and self-energy

The photoemission intensity is expressed by

$$I(\mathbf{k},\omega) \propto |M_{i,f}^{\mathbf{k}}|^2 A(\mathbf{k},\omega). \tag{3.4}$$

Here, the matrix element is $M_{i,f}^{\mathbf{k}}$, which will be mentioned in section 3.4, and the spectral function is $A(\mathbf{k},\omega)$. The spectral function is given by

$$A(\mathbf{k},\omega) = -\frac{1}{\pi}\mathrm{Im}G(\mathbf{k},\omega). \tag{3.5}$$

The *Green's* function $G_0(\mathbf{k},\omega)$ for free electrons is

$$G_0(\mathbf{k},\omega) = \frac{1}{\omega - \epsilon_{\mathbf{k}} + i\delta}, \tag{3.6}$$

where $\epsilon_{\mathbf{k}}$ is one-particle energy. The spectral function for free electrons is $A(\mathbf{k},\omega) = \delta(\omega - \epsilon_{\mathbf{k}})$. In general, the presence of electron correlation, the *Green's* function and the spectral function are expressed by the self-energy $\Sigma(\mathbf{k},\omega) = \Sigma'(\mathbf{k},\omega) + i\Sigma''(\mathbf{k},\omega)$:

$$G_0(\mathbf{k},\omega) = \frac{1}{\omega - \epsilon_{\mathbf{k}} - \Sigma(\mathbf{k},\omega)}, \tag{3.7}$$

$$A(\mathbf{k},\omega) = -\frac{1}{\pi}\frac{\Sigma''(\mathbf{k},\omega)}{\left[\omega - \epsilon_{\mathbf{k}} - \Sigma'(\mathbf{k},\omega)\right]^2 + \left[\Sigma''(\mathbf{k},\omega)\right]^2}. \tag{3.8}$$

The real part of the pole of Eq. 3.7, $\omega = \epsilon^*_{\mathbf{k}}$ is determined by solving the equation $\omega - \epsilon_{\mathbf{k}} - \Sigma'(\mathbf{k},\omega) = 0$, which gives the peak of $A(\mathbf{k},\omega)$ and the band dispersion of quasiparticles. Here, the renormalization factor is defined by

$$Z_{\mathbf{k}}(\omega) = \left[1 - \frac{\partial\Sigma'(\mathbf{k},\omega)}{\partial\omega}\right]^{-1}. \tag{3.9}$$

Considering the weak electron correlation, the spectral function becomes

$$A(\mathbf{k},\omega) = A_{coh}(\mathbf{k},\omega) + A_{incoh} \tag{3.10}$$

$$= -\frac{Z_{\mathbf{k}}(\epsilon^*_{\mathbf{k}})}{\pi}\frac{Z_{\mathbf{k}}(\epsilon^*_{\mathbf{k}})\Sigma''(\mathbf{k},\omega)}{\left[\omega - \epsilon^*_{\mathbf{k}}\right]^2 + \left[Z_{\mathbf{k}}(\epsilon^*_{\mathbf{k}})\Sigma''(\mathbf{k},\omega)\right]^2} + A_{incoh}. \tag{3.11}$$

Eq. 3.10 indicates that the spectral function has the spectral weight with $Z_{\mathbf{k}}(\epsilon^*_{\mathbf{k}})(<1)$ at $\epsilon = \epsilon^*_{\mathbf{k}}$, and the life time $1/\tau_{\mathbf{k}}$ represents the $-2Z_{\mathbf{k}}\Sigma''$.

Note that the above discription ignored the extrinsic effects such as the finite energy and momentum resolutions. The realistic photoemission intensity is expressed by

$$I_{exp}(\mathbf{k},\omega) \propto \int d\omega' d\mathbf{k}' I(\mathbf{k}',\omega') g_E(\omega - \omega') g_k(\mathbf{k} - \mathbf{k}') + B, \tag{3.12}$$

where $g(x - x')$ is the resolution function, and B is the background derived from the secondary electrons.

3.3 Angle-resolved photoemission spectroscopy

Angle-resolved photoemission spectroscopy is one of the most effective tool to investigate not only the density of states but also the band dispersion,

Fermi surface, and electron correlation. Here, we briefly review the principle of ARPES. In the photoexcitation process, the wave vector of electron should be conserved except for the reciprocal lattice vectors since the photon's momentum $h\nu/c$ is negligibly small compared with the electron's. Thus, we obtain

$$\mathbf{K}_f = \mathbf{K}_i + \mathbf{G} \tag{3.13}$$

where $\mathbf{K}_i$, $\mathbf{K}_f$ and $\mathbf{G}$ are the wave vector of the initial state in the solid, the final state of electron, and the reciprocal lattive vector $(2n_x\pi/a, 2n_y\pi/b, 2n_z\pi/c)$, respectively. When the photoelectron escapes from the solid to vaccum, the surface parallel component of the wave vector is conserved, while the surface perpendicular component is lost due to the work function Φ. therefore,

$$\mathbf{k}_{\parallel} = \mathbf{K}_{i\parallel} + \mathbf{G}_{\parallel} \tag{3.14}$$

where $\mathbf{k}$ is the wave vector of photoelectron outside the solid. Figure 3.2 shows the geometry of ARPES experiment. We define that the emission direction of photoelectron is specified by the polar θ and azimathal ϕ angles. The wave vector $\mathbf{k}$ of emitted photoelectron can be expressed by the kinetic energy E^v_{kin} of the emitted electron in the vaccum as

$$k_x = \frac{\sqrt{2mE^v_{kin}}}{\hbar}\sin\theta\cos\phi, \tag{3.15}$$

$$k_y = \frac{\sqrt{2mE^v_{kin}}}{\hbar}\sin\theta\sin\phi, \tag{3.16}$$

$$k_z = \frac{\sqrt{2mE^v_{kin}}}{\hbar}\cos\theta. \tag{3.17}$$

Finally, Eq. (3.15) and (3.16) may be rewritten by Eq.(3.1) as

$$k_x = \frac{\sqrt{2m(h\nu - \phi - E_B)}}{\hbar}\sin\theta\cos\phi + \frac{2n_x\pi}{a}, \tag{3.18}$$

$$k_y = \frac{\sqrt{2m(h\nu - \phi - E_B)}}{\hbar}\sin\theta\sin\phi + \frac{2n_y\pi}{b}, \tag{3.19}$$

where n_x and n_y are arbitrary integers. Figure 3.3 shows the schematic of the mapping of band dispersions. As for the component k_z of perpendicular to the surface, that is $\mathbf{k}_{\perp}$, it is not conserved during the photoemission process. However, one can obtain k_z using the method of perpendicular emission. This method assumes a nearly free electron dispersion modified by the potential barrier of the inner potential $V_0(= \Phi + \mu - E_0 = E_{vac} - E_0)$ as the final bulk state as shown in Fig. 3.4. Therefore, k_z $(= k_{\perp})$ can be expressed as

$$k_z = \frac{\sqrt{2m((h\nu - \phi - E_B)\cos^2\theta) + V_0}}{\hbar}. \tag{3.20}$$

Consequently, we can observe the whole band dispersion and Fermi surface by changing the polar θ, azimuthal ϕ angles, and photon energy.

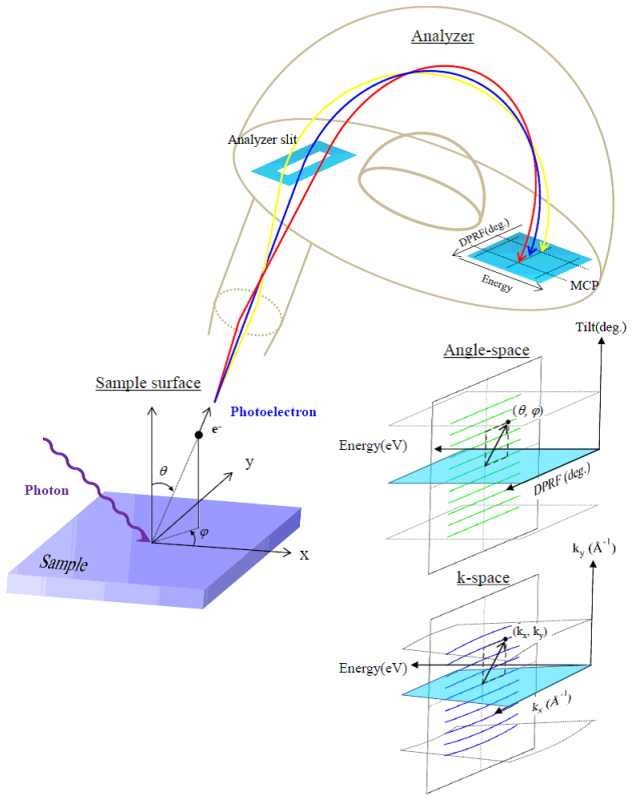

Figure 3.2: Geometry of an ARPES experiment in which the emission direction of the photoelectron is specified by the polar (θ) and azimuthal (ϕ) angles [1].

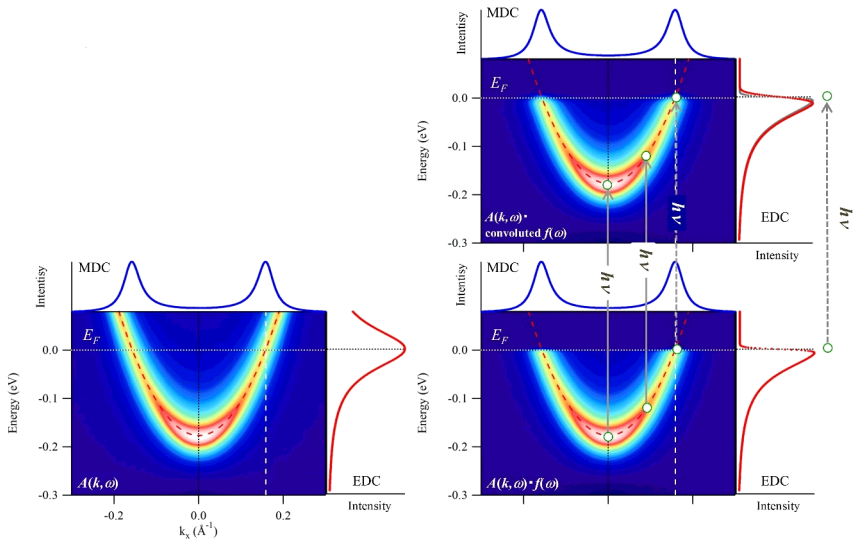

Figure 3.3: Schematic diagram showing the principle of ARPES. The band dispersion in the material is directly mapped by the ARPES spectra.

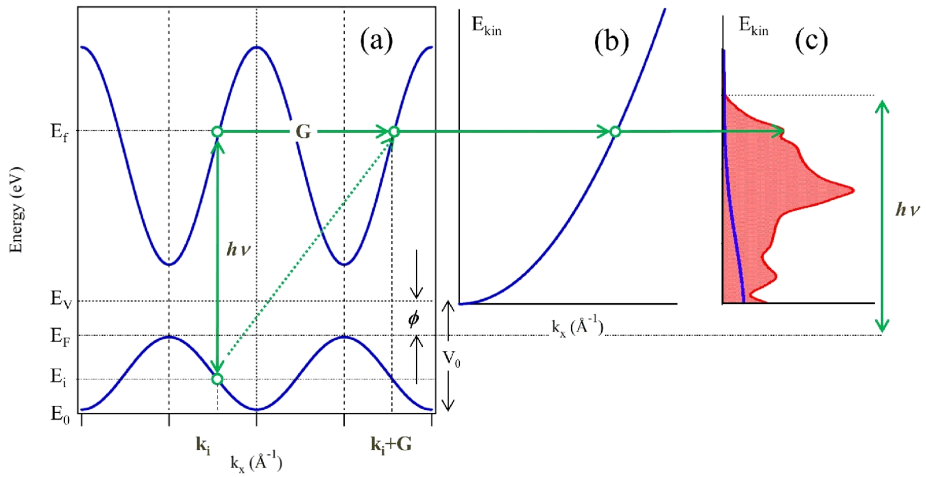

Figure 3.4: Kinematics of the photoemission process within the three-step nearly-free-electron final state model: (a) direct optical transition in the solid (the lattice supplies the required momentum); (b) free-electron final state in vacuum; (c) corresponding photoelectron spectrum, with a background due to the scattered electrons ($E_B = 0$ at E_F) [3].

3.4 Transition matrix element

In section 3.2, we discussed the photoemission intensity which includes the matrix element $M_{i,f}^{\mathbf{k}}$. The matrix element $M_{i,f}^{\mathbf{k}}$ strongly depends on the photon energy and the polarization of the incoming photon. The transition probability of the photoelectron in solids is expressed by *Fermi's golden rule*:

$$w_{fi} = \frac{2\pi}{\hbar} |\langle \Psi_f^N | \mathcal{H}_{int} | \Psi_i^N \rangle|^2 \delta(E_f^N - E_i^N - h\nu) \tag{3.21}$$

$$= \frac{2\pi}{\hbar} |M_{i,f}^{\mathbf{k}}|^2 \delta(E_f^N - E_i^N - h\nu) \tag{3.22}$$

Here, the electron-photon interaction is treated as a perturbation given by

$$\mathcal{H}_{int} = -\frac{e}{2mc}(\mathbf{A}\cdot\mathbf{p} + \mathbf{p}\cdot\mathbf{A}) = -\frac{e}{mc}\mathbf{A}\cdot\mathbf{p}. \tag{3.23}$$

Therefore, the matrix element is represented by

$$|M_{i,f}^{\mathbf{k}}|^2 = |\langle \phi_f^{\mathbf{k}} | \mathbf{A}\cdot\mathbf{p} | \phi_i^{\mathbf{k}} \rangle|^2 \tag{3.24}$$

$$\propto |\langle \phi_f^{\mathbf{k}} | \boldsymbol{\epsilon}\cdot\mathbf{r} | \phi_i^{\mathbf{k}} \rangle|^2, \tag{3.25}$$

where $\boldsymbol{\epsilon}$ is a unit vector along the polarization direction of the vector potential $\mathbf{A}$. The photoemission intensity increases when the wave functions of $\nabla\phi_i$ and

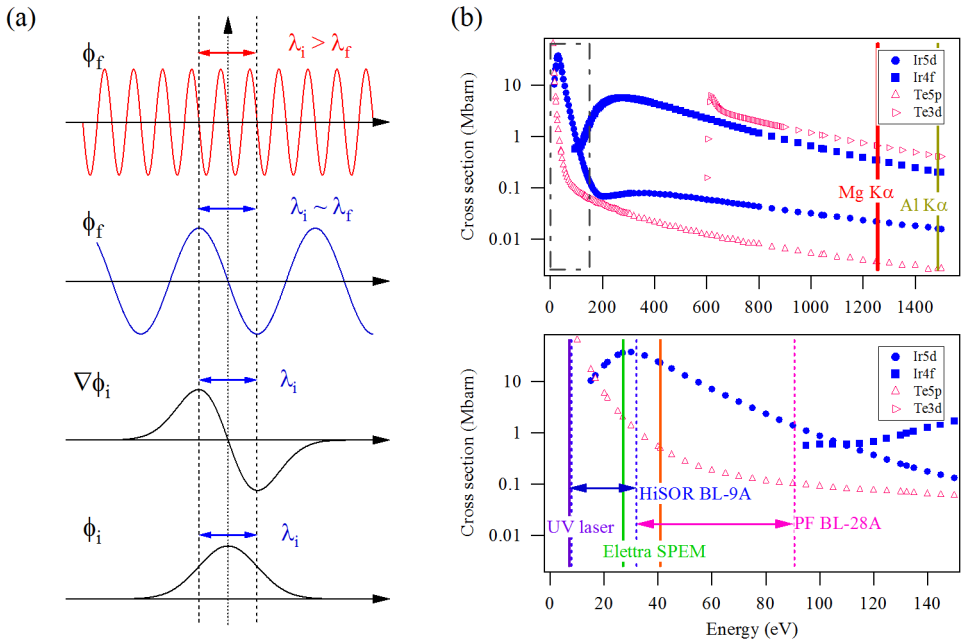

Figure 3.5: (a) Schematics of the overlap between the initial state and final state. (b) Calculation of the photoionization cross sections for Ir and Te atoms [4].

ϕ_f overlap each other. The schematics of the overlap between the initial state and final state are displayed in Fig. 3.5 (a). In case of the localized (iternelant) electrons such as d and f electrons (s and p electrons), the photoionization cross section should be larger (smaller) with increase of the photon energy. Figure 3.5 (b) shows the calculation of the photoionization cross sections for Ir and Te atoms [4].

3.5 Electron escape depth

When an electron in a solid absorb the photon energy $h\nu$, the electron move into a vacuum. In this prosess, the electron is inelasticallly scattered due to the electron-electron or electron-phonon interaction and has the finite escape depth of the electron λ. The electron-phonon scattering contributes to the escape depth below the phonon frequencies. Thus, the escape depth of the electron λ mainly depends on the inelastic electron-electron scattering. In general, the cross section of the inelastic scattering σ is represented by the dielectric function $\epsilon(q, \omega)$. The cross section σ of electron-electron interaction

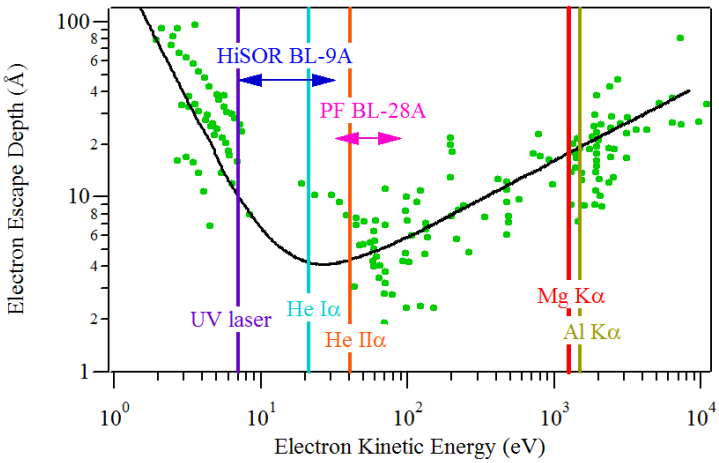

Figure 3.6: Mean free path of an electron in respect to its energy in various solids taken from [2].

is given by

$$\frac{d\sigma}{d\Omega dE} \propto \frac{1}{q^2}\mathrm{Im}\left[-\frac{1}{\epsilon(q,\omega)}\right], \tag{3.26}$$

where q is the momentum and ω is the energy loss of the electron. The electron in solid can be described as the free-electron gas within 10 $\sim$ 1000 eV. In the free-electron gas, the imaginary part of inverse dielectric function $\mathrm{Im}(-1/\epsilon(q,\omega))$ is determined by the plasma frequency, which is a function of the electron density or the mean electron-electron distance r_s, and the damping rate of plasmon. Therefore, the escape depth of the electron λ is described by the mean electron-electron distance r_s:

$$\lambda^{-1} \sim \sqrt{3}\frac{a_0 R}{E_{kin}} {r_s}^{-3/2} \log\left[\left(\frac{4}{9\pi}\right)^{3/2} \frac{E_{kin}}{R} {r_s}^2\right] \tag{3.27}$$

, where a_0=0.529 Å, R=13.6 eV, r_s is measured in units of Bohr radius a_0, and E_{kin} is the kinetic energy of photoelectrons. Figure 3.6 shows the mean free path of the photoelectron as a function of the electron energy. Here, the electron energies excited by typical photon sources are indicated by the vertical lines. The photoemission measurement often uses the excitation light with $h\nu$ = 10 $\sim$ 1000 eV. The mean free path is about 10 Å at the longest when the kinetic energy is $\sim$ 1000 eV. Thus, the photoemission spectroscopy is a surface sensitive measurement. However, we can investigate the bulk and the surface properties, in order to select the suitable photon energy.

3.6 Energy resolution

Photoemission measurements were performed using a hemispherical electron analyzer. The resolution of the electron analyzer is theoretically estimated by

$$\Delta E_{ana} = E_p \left(\frac{\Delta_{slit}}{2R} + \frac{\alpha^2}{4} \right) \sim E_p \frac{\Delta_{slit}}{2R}. \tag{3.28}$$

Here, E_p is the pass energy, Δ_{slit} is the slit width, R is the mean radius of the two hemispheres, and α is the acceptance angle of the entrance slit. We have performed the angle-resolved photoemission spectroscopy using VG-Scienta SES2002, R4000, and HR8000. The parameters and the estimated energy resolution of the electron analyzer is shown in table 3.1.

Table 3.1: Parameters and energy resolution of the electron analyzer

	SES2002	R4000	HR8000
Pass energy E_p	$\geq$ 1.0 eV	$\geq$ 1.0 eV	$\geq$ 0.5 eV
Radius of analyzer R	200 mm	200 mm	200 mm
Slit width Δ_{slit}	$\geq$ 200 μm	$\geq$ 100 μm	$\geq$ 50 μm
Energy resolution ΔE_{ana}	$\geq$ 500 μm	$\geq$ 250 μm	$\geq$ 62.5 μm

Table 3.2: Energy resolutions of the typical photon sources

Photon Source	Photon energy $h\nu$	Energy resolution $\Delta E_{h\nu}$
Mg Kα	1252.6 eV	700 meV
Al Kα	1486.6 eV	850 meV
He Iα	21.2 eV	1.1 meV
Xe Iα	8.4 eV	600 μeV
Synchrotron	$\geq$7 eV	$\geq$250 μeV
VUV laser	6.994 eV	260μeV

The total energy resolution is determined by the energy resolution of the electron analyzer ΔE_{ana}, the energy resolution of the photon source $\Delta E_{h\nu}$, and the external factors ΔE_{etc}:

$$\Delta E_{total} = \sqrt{{\Delta E_{ana}}^2 + {\Delta E_{h\nu}}^2 + {\Delta E_{etc}}^2}. \tag{3.29}$$

Table 3.2 shows the energy resolution of the photon source. Therefore, we can theoretically estimate the total energy resolution using equation (3.29).

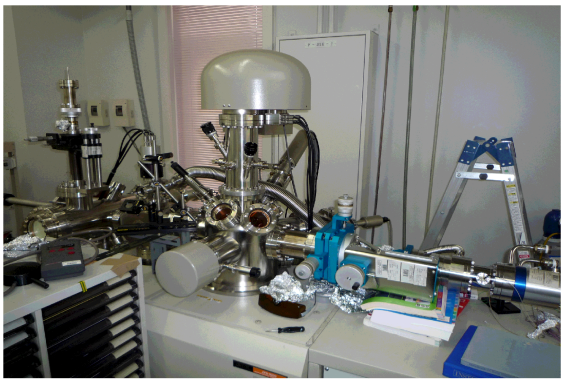

Figure 3.7: Photogragh of XPS setup.

The actual values of the total energy resolution are experimentally estimated using the observed photoemission spectrum near the Fermi level of the metallic sample such as gold. The observed Fermi-edge cuttoff is fitted by the Fermi-Dirac distribution function convoluted with a Gauss function of the full width at half maximum (FWHM). The FWHM is the adjustable parameter and corresponding to the total energy resolution.

3.7 Experimental setups

3.7.1 X-ray Photoemission Spectroscopy

X-ray photoemission spectroscopy (XPS) has been performed using JOEL JPS-9200 with a monochromatized Al $K\alpha$ (hν = 1486.6 eV) and Mg $K\alpha$ (hν = 1253.6 eV) x-ray sources. The picuture of the XPS set up is displayed in Fig. 3.7. The total energy resolution using the monochromatized Al $K\alpha$ (unmonochromatized Mg $K\alpha$) sources is about 0.6 eV (1.0 eV). The base pressure of the chamber was in the 10^{-7} Pa range. Measurement temperature can be varied from $\sim$ 20 to 300 K using dilution refrigerator.

3.7.2 ARPES at Hiroshima Syncrotron Light Source BL-9A

Angle-resolved photoemission spectroscopy (ARPES) has been performed at HiSOR BL-9A in Hiroshima Synchrotron Radiation Center (HSRC) in Hiroshima University [5]. The optical layout of the BL-9 beamline is displayed in Fig. 3.8. The beamline is a helical/linear switchable undulator beamline with a spherical greating (G) in the 4 - 40 eV energy range. The 3 m off-plane Ea-

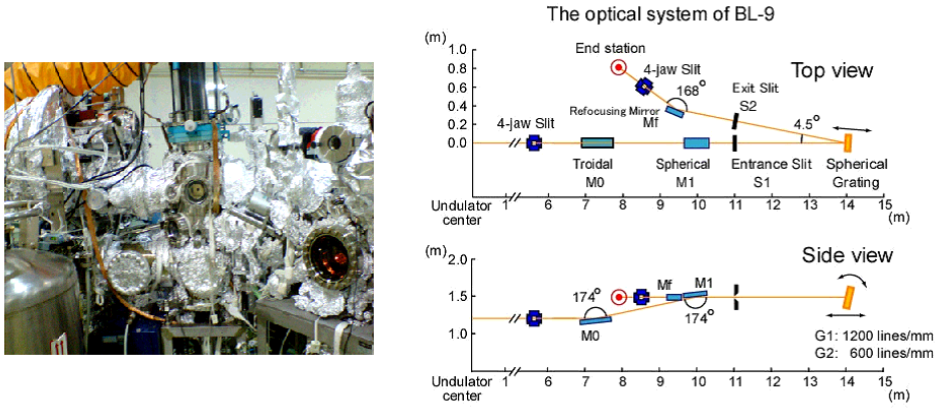

Figure 3.8: Photograph of HiSOR BL-9A main chamber and a schematics of the optical system of the 3 m off-plane Eagle monochromator at HiSOR BL-9.

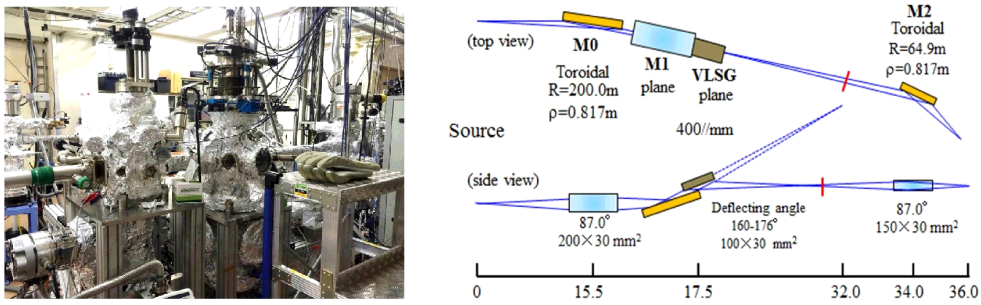

Figure 3.9: Photograph of PF BL-28 and a schematics of the optical system at PF BL-28A

gle monochromator is adopted as its main optical system. The photon-energy range available for photoemission experiment is 7-32 eV. The end station is equipped with a VG-SCIENTA R4000 analyzer for angle-resolved photoemission experiments, which is a 200 mm mean radius spectrometer. The base pressure of the spectrometer was 10^{-9} Pa range. The samples can be cooled using a liquid He refrigerator.

3.7.3 ARPES at Photon Factory BL-28A

Angle-resolved photoemission spectroscopy (ARPES) has been performed at Photon Factory BL-28A in High Energy Accelerator Research Organization (KEK). The beamline is a helical/linear switchable undulator beamline with

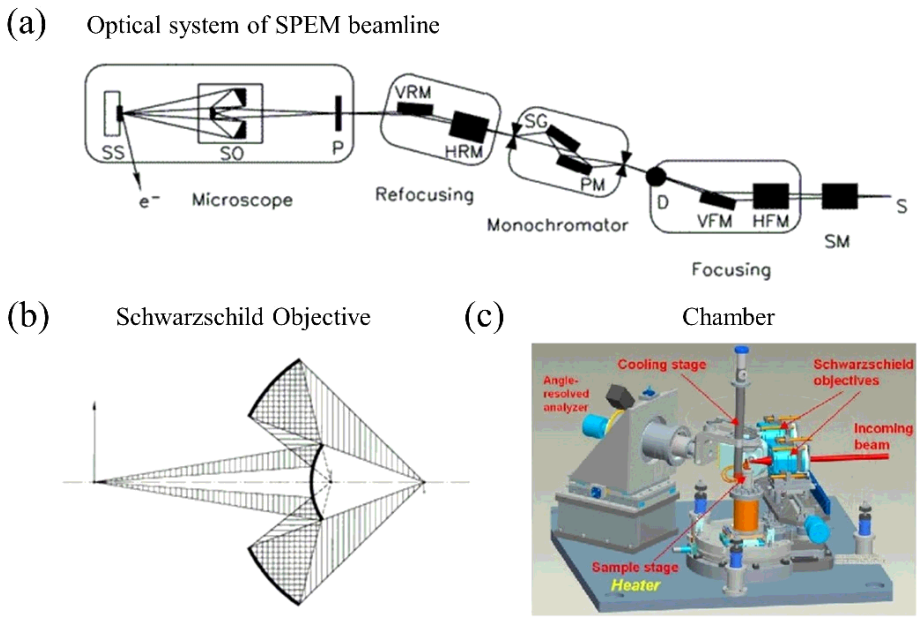

Figure 3.10: Schematics of Elettra beamline: (a) the optical system, (b) Schwarzchild objective and (c) Main chamber. [6]

a spherical greating Monochromator (SGM) in the 32 - 800 eV energy range, as shown in Fig. 3.9. The photon-energy range available for photoemission experiments is 32 - 90 eV The end station is equipped with a VG-SCIENTA SES2002 analyzer for angle-resolved photoemission experiments in Fig. 3.9. The angular resolution was set to $\sim 0.3°$. The base pressure of the spectrometer was 10^{-10} Torr range. The samples can be cooled from 9 to 300K using liquid He refrigerator.

3.7.4 Photoemission Microscopy at Elettra SPEM beamline

Photoemission microscopy is a powerful tool to observe the spacial distribution of photoemission spectrum. The photoemission microscopy has been performed at SPEM beamline in Elettra sincrotrone Trieste. The sub-micron size beam spot is obtained by a Schwarzschild objective as shown in Fig. 3.10(a-b). The photon-energy available for photoemission microscopy experiment is 27 and 74 eV. The sample focusing and imaging are carried out using the XYZR scanning stage in Fig. 3.10(c). The base pressure of main chamber was $10^{-}10$ Torr range. The samples can be cooled using liquid He or liquid N_2.

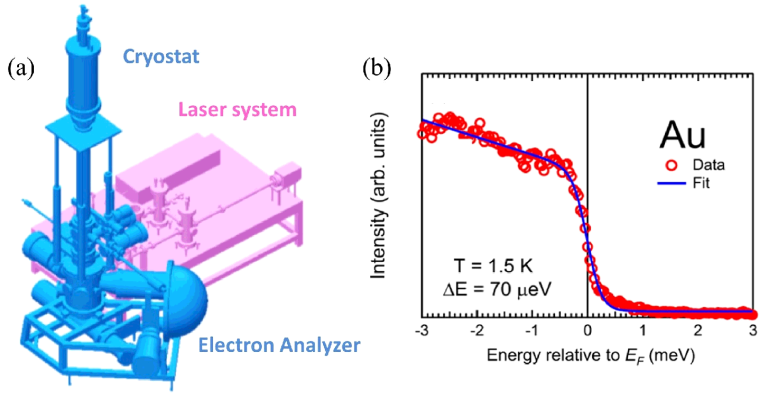

Figure 3.11: (a) Schematic of Laser-ARPES system at ISSP Shin group, (b) Photoemission spectrum of Au [7].

3.7.5 Laser-ARPES at ISSP, Shin-group #3

High energy resolution was realized by Laser light source, because of the sharpness of line width. Laser angle-resolved photoemission spectroscopy(Laser-ARPES) has been performed at Shin group in Institute of Solid States Physics (ISSP), University of Tokyo, using a VG-Scienta HR8000 analyzer and a VUV-laser of 6.994 eV as a photon source. The angular resolution was set to $\sim 0.1°$. All the polarization of the light is able to adjust a half-wave ($\lambda/2$) plate and a quarter-wave ($\lambda/4$) plate. Figure 3.11 shows the schematic of Laser-ARPES apparatus, which achieves the lowest temperature of 1.5K and the highest energy resolution of 70μeV by using a Fermi-Dirac distribution function convoluted with a Gaussian of FWHM as shown in Fig. 3.11.

References

[1] A. Damascelli, Z. Hussain, and Z.-X. Shen, Rev. Mod. Phys. **75**, 473 (2003).

[2] S. Hüfner, Photoelectron Spectroscopy, Springer-Verlag, Berlin, (2003).

[3] A. Damascelli, Physica Scripta T109, **61** (2004).

[4] J. J. Yeh and I. Lindau, Atomic Data and Nuclear Data Tables, 32, 1-155 (1985).

[5] T. Matsui, H. Sato, K. Shimada, M. Arita, S. Senba, H. Yoshida, K. Shirasawa, M. Morita, A. Hiraya, H. Namatame, and M. Taniguchi, Nucl. Istr. and Meth. A **467 − 468**, 537 (2001)

[6] Elettra sincrotrone Trieste, Home page, Last Updated on Wednesday, 05 June 2013. https://www.elettra.trieste.it/elettra-beamlines/spectromicroscopy.html

[7] T. Shimojima, K. Okazaki, and S. Shin, J. Phys. Soc. Jpn. **84**, 072001 (2015).

Chapter 4

Core-level electronic structure of $Ir_{1-x}Pt_xTe_2$

Before presenting the angle-resolved photoemission spectroscopy result, we describe the fundamental electronic structure of $IrTe_2$ and $Ir_{0.95}Pt_{0.05}Te_2$ using the x-ray photoemission spectroscopy (XPS).

4.1 Experimental Setups

Single crystal samples of $IrTe_2$ and $Ir_{0.95}Pt_{0.05}Te_2$ were prepared using a self-flux method [1, 2]. X-ray photoemission spectroscopy (XPS) measurements were performed using a JPS 9200 spectrometer equipped with a Mg Kα x-ray source (hν = 1256.6 eV). The total energy resolution was about 0.8 eV. The base pressure of the chamber was in the 10^{-7} Pa range. The single crystals of $IrTe_2$ and $Ir_{0.95}Pt_{0.05}Te_2$ were cleaved at 300K under the ultrahigh vacuum and the spectra were acquired within 24 hours after the cleavage. Binding energies were calibrated using the Au $4f$ core-level of the gold reference sample.

4.2 Results and Discussion

Core-level Ir $4f$ spectra for single crystals $IrTe_2$ and $Ir_{0.95}Pt_{0.05}Te_2$ show the Ir $4f_{7/2}$ and Ir $4f_{5/2}$ peaks due to the spin-orbit interaction as shown in Fig. 4.1 (a). The Ir $4f$ core-levels of $IrTe_2$ and $Ir_{0.95}Pt_{0.05}Te_2$ are compared with that of $CuIr_2S_4$ [3]. The formal valences of Ir for $IrTe_2$ and $CuIr_2S_4$ are Ir^{4+} and $Ir^{3.5+}$, respectively. At 300K, the Ir $4f_{7/2}$ peaks of $IrTe_2$ and $Ir_{0.95}Pt_{0.05}Te_2$ are located at the lower binding energy than that of $CuIr_2S_4$ with $Ir^{3.5+}$, indicating that the actual valences of Ir for $IrTe_2$ and $Ir_{0.95}Pt_{0.05}Te_2$ are close to Ir^{3+}. This is consistent with the Ir L_3-edge x-ray absorption spectroscopy and the band-

structure calculation for $IrTe_2$ by Kamitani *et al.* [4]. On the other hand, the line shapes of Ir $4f$ core-level peaks for $IrTe_2$ and $Ir_{0.95}Pt_{0.05}Te_2$ show the asymmetric line shape commonly due to the screening effect, indicating that the Ir $5d$ electrons contribute to metallic conductivity [5]. Therefore, the Ir $5d$ t_{2g} orbitals of $IrTe_2$ and $Ir_{0.95}Pt_{0.05}Te_2$ are almost fully occupied, but not completely. Since the valence of Ir is close to Ir^{3+}, the valence of Te should be $Te^{1.5-}$, suggesting that the Te $5p$ orbitals are partially unoccupied. This picture is consistent with the band structure calculation in which the density of states near the Fermi level mainly consists of the Te $5p$ orbitals. The Te $3d$ core-level spectra for $IrTe_2$ and $Ir_{0.95}Pt_{0.05}Te_2$ are displayed in Fig. 4.1 (c). The Te $3d_{5/2}$ and $3d_{3/2}$ peaks are clearly observed. The binding energy of Te $3d_{5/2}$ core-level is close to that of pure Te (573 eV), indicating that the Te $5p$ states are not fully occupied and contribute to the electronic states near Fermi level. The x-ray absorption spectroscopy confirmed the existence of Te $5p$ holes by the pre-edge structure of Te $3d$ [6]. Indeed, the valence-band spectra of $IrTe_2$ and $Ir_{0.95}Pt_{0.05}Te_2$ exhibit a peak around $\sim$2.5 eV below Fermi level, wheras the spectral weight near Fermi level is rather weak in Fig. 4.1 (c). At hν = 1253.6 eV, the photoionization cross section of Ir $5d$ is much larger than that of Te $5p$ at this photon energy as shown in Fig. 3.5 (b). This indicates that the electronic states at 2 - 3 eV below Fermi level are dominated by Ir $5d$, while that near Fermi level have more Te $5p$ character. These results indicate the strong hybridization between the Ir $5d$ and Te $5p$, namely that the charge-transfer energy from Ir $5d$ to Te $5p$ is small.

The Ir $4f$ peak width for $IrTe_2$ increases in going from 300K to 40K, while that for $Ir_{0.95}Pt_{0.05}Te_2$ does not change with temperature, which is consistent with the our previous XPS results using polycrystalline $IrTe_2$ [7]. On the other hand, the Te $3d$ peaks of $IrTe_2$ and $Ir_{0.95}Pt_{0.05}Te_2$ do not show any such changes with temperature as shown in Fig. 4.1 (c). The Ir $4f$ peak width increase of $IrTe_2$ is comparable to that of $CuIr_2S_4$, in which an Ir^{3+}/Ir^{4+} charge ordering was established with the metal to insulator transition [8]. The Ir $4f$ peaks for $IrTe_2$ at 40K can be decomposed into the two components, which are derived from Ir^{4+} and Ir^{3+} components, suggesting the mixed valence state. As shown in Fig. 4.1 (b), the solid curves indicate the results of Mahan's line shape fitting for $IrTe_2$ at 300K and 40K [9]. The Ir $4f$ peaks at 300K can be easily fitted using the single component of Ir^{3+}. In going from 300K to 40K, the Ir^{4+} components appear at higher binding energy than the Ir^{3+} components. The energy splitting between the Ir^{4+} and Ir^{3+} components for $IrTe_2$ is $\sim$0.39 eV, which is comparable to that of $CuIr_2S_4$ $\sim$0.4 eV. This is consistent with the previous reported value [11, 12]. In general, the binding energy shift ΔE is

represented by the formula below

$$\Delta E_B = K\Delta Q + \Delta V_M - \Delta E_R \tag{4.1}$$

where K is the coupling constant of coulomb interaction between the valence electrons and core hole, Q is the local charge on the ion, V_M is Madelung potential, and E_R is the screening of the core hole potential by conduction electrons or extra. In $IrTe_2$, the ΔE_R should be small, owing to that the Ir $5d$ electrons are almost occupied. If the difference of Madelung potential V_M is neglected, the binding energy shift becomes $\Delta E_B \sim K\Delta Q$. The coupling constant K is expected to be ~ 1, referred from the binding energy shift of the different compounds with Ir^{3+} and Ir^{4+}, respectively [10]. Therefore, the difference of local charge ΔQ between the Ir^{3+} and Ir^{4+} sites is $\sim$0.39, which agrees with the value $\sim$0.4 of Ir $4f$ core-level shift estimated by the band structure calculation [13].

4.3 Conclusion

We have performed the core-level photoemission spectroscopy of $IrTe_2$ and $Ir_{0.95}Pt_{0.05}Te_2$. At 300K, the valences of Ir and Te are close to Ir^{3+} and $Te^{1.5-}$, respectively. Therefore, the Te $5p$ and Ir $5d$ electrons contribute to the metallic conductivity, owing to the small charge transfer energy. The temperature dependence of Ir $4f$ core-level spectra shows that the Ir^{3+}/Ir^{4+} charge ordering established in the low temperature phase of $IrTe_2$ is suppressed by Pt doping. This indicates that the suppression of Ir^{3+}/Ir^{4+} charge ordering is related to the appearance of superconductivity.

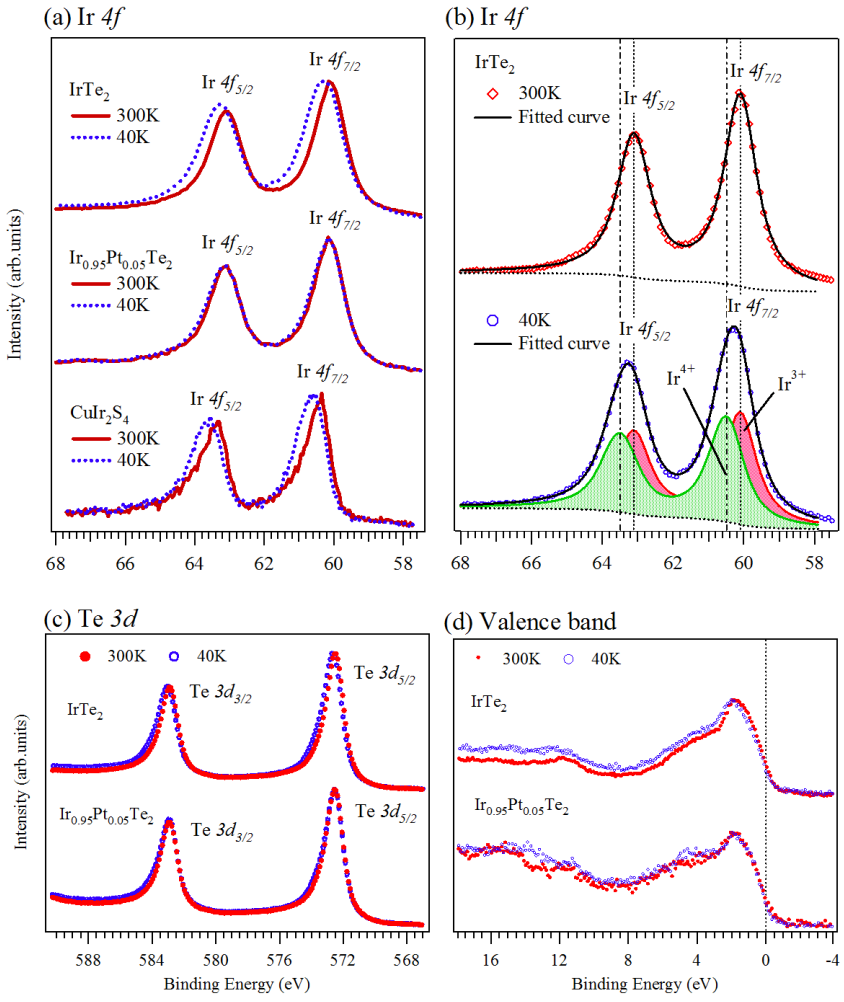

Figure 4.1: X-ray photoemission spectra taken at 300K and 40K. (a) Ir $4f$ core-level spectra for $IrTe_2$, $Ir_{0.95}Pt_{0.05}Te_2$ and $CuIr_2S_4$. (b) Temperature dependence of Ir $4f$ core-level for $IrTe_2$. Solid lines indicate the fitted results. (c) Te $3d$ core-level spectra for $IrTe_2$ and $Ir_{0.95}Pt_{0.05}Te_2$. (d) Valence band spectra for $IrTe_2$ and $Ir_{0.95}Pt_{0.05}Te_2$.

References

[1] S. Pyon, K. Kudo, and M. Nohara, Physica C **494**, 80-84 (2013)

[2] A. F. Fang, G. Xu, T. Dong, P. Zheng, and N. L. Wang, Sci. Rep. **3**, 1153 (2013).

[3] K. Takubo, S. Hirata, J. Y. Son, J. W. Quilty, T. Mizokawa, N. Matsumoto, and S. Nagata, Phys. Rev. Lett. **95**, 246401 (2005).

[4] M. Kamitani, . S. Bahramy, . Arita, S. Seki, T. Arima, Y. Tokura, and S. Ishiwata Phys. Rev. B **87**, 180501 (R) (2013).

[5] S. Doniach and M. Sunjic, J. Phys., **C3**, 385 (1970).

[6] K. Takubo, R. Comin, D. Ootsuki, T. Mizokawa, H. Wadati, Y. Takahashi, G. Shibata, A. Fujimori, R. Sutarto, F. He, S. Pyon, K. Kudo, M. Nohara, G. Levy, I. S. Elfimov, G. A. Sawatzky, and A. Damascelli, Phys. Rev. B **90**, 081104 (R) (2014)

[7] D. Ootsuki, Y. Wakisaka, S. Pyon, K. Kudo, M. Nohara, M. Arita, H. Anzai, H. Namatame, M. Taniguchi, N. L. Saini, and T. Mizokawa, Phys. Rev. B **86**, 014519 (2012).

[8] P. G. Radaelli, Y. Horibe, M. J. Gutmann, H. Ishibashi, C. H. Chen, R. M. Ibberson, Y. Koyama, Y. S. Hor, V Kirykhin, and S. W. Cheong, Nature **416**, 155 (2002).

[9] G. D. Mahan, Phys. Rev. B. **11**, 4814 (1975).

[10] V. I. Nefedov, Y. V. Salyn, I. B. Baranovskii, and A. B. Nikolskii, Zh. Neorg. Khim. **22**, 1715 (1977).

[11] T. Qian, H. Miao, Z. J. Wang, X. Shi, Y. B. Huang, P. Zhang, N. Xu, L. K. Zeng, P. Richard, M. Shi, G. Xu, X. Dai, Z. Fang, A. F. Fang, N. L. Wang, and H. Ding, New J. Phys. **16**, 123038 (2014)

[12] K.-T. Ko, H.-H. Lee, D.-H. Kim, J.-J. Yang, S.-W. Cheong, M.J. Eom, J.S. Kim, R. Gammag, K.-S. Kim, H.-S. Kim, T.-H. Kim, H.-W. Yeom, T.-Y. Koo, H.-D. Kim, and J.-H. Park, Nature Communications **6**, 7342 (2015)

[13] Kyoo Kim, Sooran Kim, K. —T. Ko, Hwangho Lee, J. —H. Park, J. J. Yang, S.-W. Cheong, and B. I. Min, Phys. Rev. Lett. **114**, 136401 (2015)

Chapter 5

Valence-band electronic structure of $Ir_{1-x}Pt_xTe_2$

In this chapter, we present the results of angle-resolved photoemission spectroscopy (ARPES) using the synchrotron light source in order to investigate the valence-band electronic structure of $Ir_{1-x}Pt_xTe_2$ above and below the structural phase transition. First, we discuss the electronic structure of high temperature phase. In section 5.3.1, the doping effects of $Ir_{1-x}Pt_xTe_2$ are investigated. Then, we show the three-dimensional electronic structure and the roles of spin-orbit interaction of $Ir_{1-x}Pt_xTe_2$ in the high temperature phase in sections 5.3.2 and 5.3.3. Finally, the electronic structures of $IrTe_2$ in the low temperature phase are presented in section 5.3.4.

Main contexts of this chapter have been published as:

- *"Important roles of Te 5p and Ir 5d spin-orbit interactions on multi-band electronic structure of triangular Lattice superconductor $Ir_{1-x}Pt_xTe_2$"* by D. Ootsuki,T. Toriyama, M. Kobayashi, S. Pyon, K. Kudo, M. Nohara, T. Sugimoto, T. Yoshida, M. Horio, A. Fujimori, M. Arita, H. Anzai, H. Namatame, M. Taniguchi, N. L. Saini, T. Konishi, Y. Ohta, T. Mizokawa,
  Journal of Physical Society of Japan, **83**, 033704 (2014),

- *"Te 5p orbitals bring three-dimensional electronic structure to two dimensional $Ir_{0.95}Pt_{0.05}Te_2$"* by D. Ootsuki,T. Toriyama, S. Pyon, K. Kudo, M. Nohara, K. Horiba, M. Kobayashi, K. Ono, H. Kumigashira, T. Noda, T. Sugimoto, A. Fujimori, N. L. Saini, T. Konishi, Y. Ohta, T. Mizokawa,
  Physical Review B **89**, 104506 (2014).

5.1 Introduction

First, we would like to mention our previous ARPES study [9]. At $h\nu$=23 eV, the multi-band Fermi surfaces with six-fold symmetry are observed at 300K, which basically agrees with the band structure calculation. This indicates the small effect of electron correlation in $IrTe_2$. Across the structural phase transition, the inner Fermi surfaces are strongly modified and become the straight Fermi surfaces. Considering the core-level electronic structure of $Ir_{1-x}Pt_xTe_2$, as we discussed in chapter 4, and the multi-band Fermi surfaces obtained at $h\nu$=23 eV, the three-dimensional electronic structure of $Ir_{1-x}Pt_xTe_2$ is expected. However, the three-dimensional nature of the Fermi surfaces has not been investigated in $Ir_{1-x}Pt_xTe_2$. Therefore, we performed ARPES measurements of $Ir_{1-x}Pt_xTe_2$ (x= 0.00 and 0.05) at various photon energies in order to study the three-dimensional Fermi surfaces above and below the structural phase transition.

5.2 Experiment

Single crystal samples of $Ir_{1-x}Pt_xTe_2$ were prepared using a self-flux method [1, 2]. Angle-resolved photoemission spectroscopy (ARPES) measurements were performed at beamline 9A of Hiroshima Synchrotron Radiation Center (HiSOR) and beamline 28A of Photon Factry (PF). At HiSOR BL-9A, the total energy resolutions were set to 8 - 23 meV for excitation energies of $h\nu$ = 17 - 29 eV, respectively. At PF BL-28A, the total energy resolutions were set to 20-30 meV for the excitation energies from 54 - 79 eV. The base pressures of the spectrometer for HiSOR BL-9A and PF BL-28A were in the 10^{-9} Pa, range. The single crystals of $IrTe_2$ and $Ir_{0.95}Pt_{0.05}Te_2$ which were oriented by *ex situ* Laue measurements, were cleaved at 300K and 20K, respectively under the ultrahigh vacuum and the spectra were acquired within 12 hours after the cleavage. Binding energies were calibrated using the Fermi edge of gold reference samples.

5.3 Results and discussion

5.3.1 Doping effect of $Ir_{1-x}Pt_xTe_2$ at high temperature phase

Fermi surface maps and band dispersions along A-H direction for $IrTe_2$ at high temperature phase are compared with those of $Ir_{0.95}Pt_{0.05}Te_2$ in Fig. 5.1. The Fermi surface maps and band dispersions of $IrTe_2$ and $Ir_{0.95}Pt_{0.05}Te_2$ were

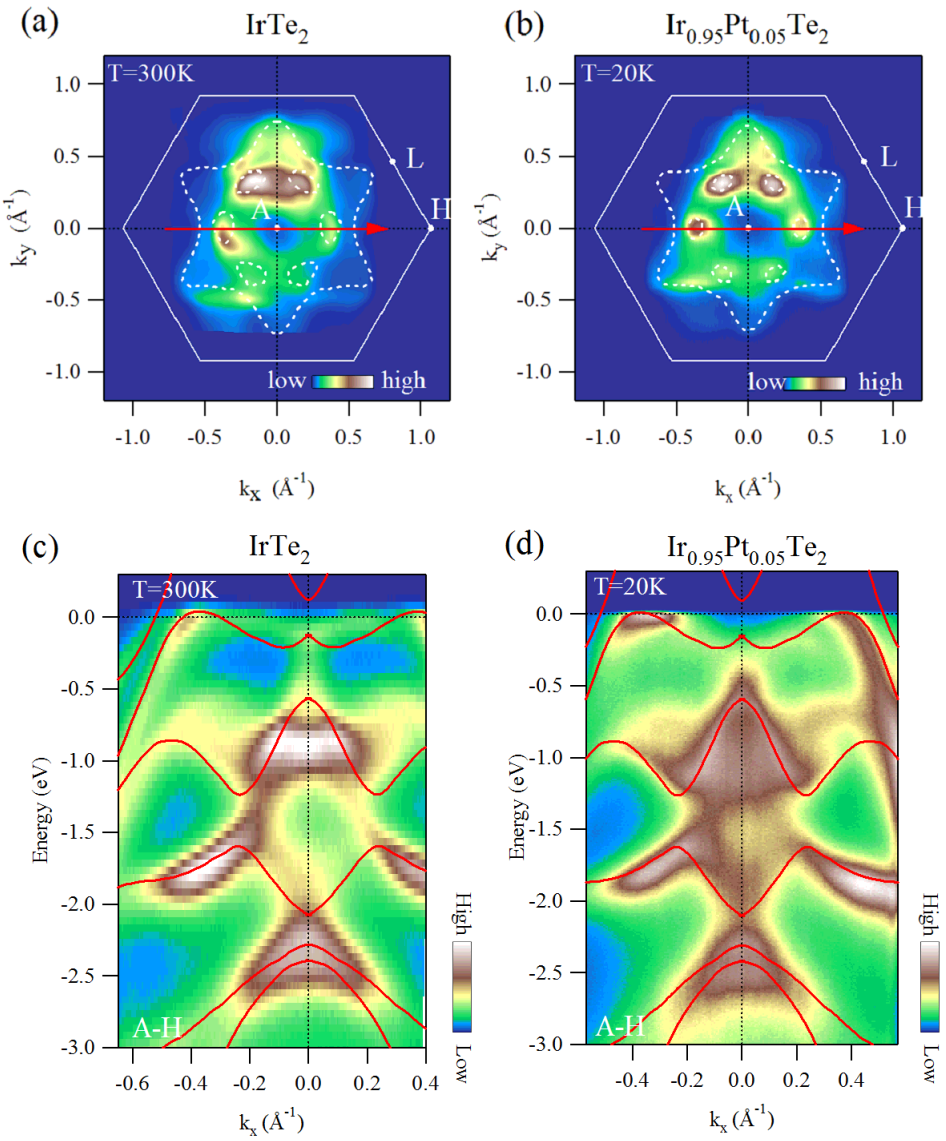

Figure 5.1: Fermi surface maps for $IrTe_2$ at 300K (a) and $Ir_{0.95}Pt_{0.05}Te_2$ at 20K (b). Dots lines indicate the Fermi surfaces obtained from the band-structure calculation with the spin-orbit interaction. Band dispersions along A-H direction for $IrTe_2$ at 300K (c) and $Ir_{0.95}Pt_{0.05}Te_2$ at 20K (d). Solid lines indicate the band dispersions obtained from the band-structure calculation with the spin-orbit interaction.

taken at 300K and 20K, respectively. The photon energy is set to hν=23 eV, corresponding to the A point. Assuming the rigid band shift, the chemical potential in $Ir_{0.95}Pt_{0.05}Te_2$ is shifted upwards in the band structure for $IrTe_2$, since the Pt substitution introduces the 0.05 electrons per Ir into the Ir 5*d* and Te 5*p* bands. The Fermi surfaces and band dispersions using the band structure calculation with the spin-orbit interaction are shown as the dot lines and solid lines, respectively in Fig. 5.1. The small hole pockets are formed by the inner hole bands, while the large Fermi surface is formed by the outer hole band. The observed inner and outer Fermi surfaces of $Ir_{0.95}Pt_{0.05}Te_2$ become smaller than that of $IrTe_2$, reflecting the electron doping, and agree very well with the band structure calculation. Indeed, the energy shift between $IrTe_2$ and $Ir_{0.95}Pt_{0.05}Te_2$ is consistent with the rigid band shift of the calculated results, indicating that the Pt doping provides electrons to the Ir 5*d* and Te 5*p* bands. It is notable that the Fermi surface and the band dispersion of the high temperature phase stably exist to low temperature in $Ir_{0.95}Pt_{0.05}Te_2$, indicating that the Fermi surface and the band dispersion of the high temperature phase are deeply related to the appearance of superconductivity.

As a result of electron doping, the inner hole pockets of $Ir_{0.95}Pt_{0.05}Te_2$ become smaller than that of $IrTe_2$. In the manner of the saddle point mechanism [6], the structural instability should be more enhanced than that of $IrTe_2$. However, the structural phase transition of $Ir_{0.95}Pt_{0.05}Te_2$ is completely suppressed. This indicates that the structural phase transition does not originate from the van Hove singularity. In addition, Kudo *et al.* have proposed that $Ir_{1-x}Rh_xTe_2$ also exhibits structural phase transition and superconductivity (T_c=2.6K) [3]. The isovalent doping can suppress the structural phase transition, suggesting that electron doping does not play a crucial role in the suppression of the structural phase transition.

In $Ir_{1-x}Rh_xTe_2$, the doping level of Rh is three times higher than that of Pt in order to suppress the structural phase transition. On the other hand, the Pt and Pd doping easily destroy the structural phase transition. Considering the lattice constant, the unit cell volume of $Ir_{1-x}Rh_xTe_2$ does not change with the doping, while the change of the unit cell volume is large in Pt doping [3–5]. Furthermore, the scanning tunneling microscopy (STM) reveals the patch structure of the superconducting samples due to the chemical strain and the local impurity state [7, 8]. Therefore, the local disorder is the key role of the suppression of the structual phase transition.

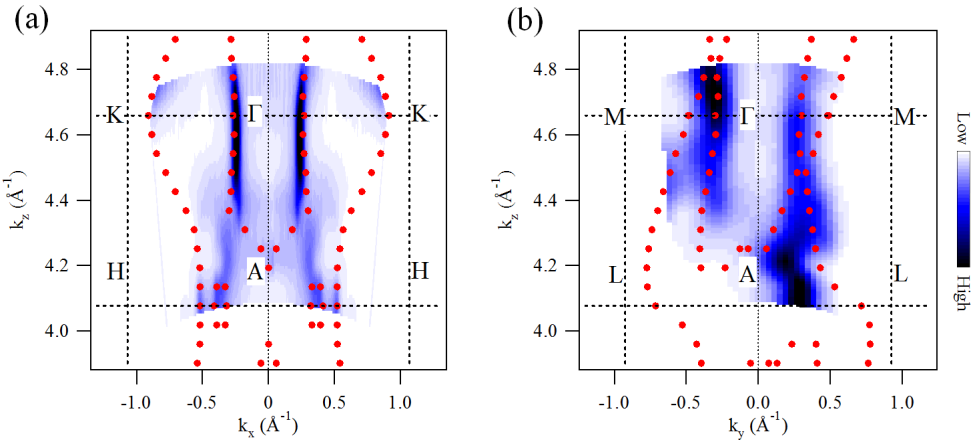

Figure 5.2: Fermi surface maps for $Ir_{0.95}Pt_{0.05}Te_2$ in (a) k_z - k_x plane and (b) k_z - k_y plane. k_x, k_y, and k_z are electron momenta along the the Γ-K or A-H direction, the Γ-M or A-L direction and the Γ-A direction, respectively. Dots lines indicate the band-structure calculations with the spin-orbit interaction.

5.3.2 Three-dimensional electronic structure at high temperature phase

At high temperature phase, as we mentioned in Chapter 2.2, the three- dimensional Fermi surfaces of $Ir_{1-x}Pt_xTe_2$ are predicted by the band structure calculation, in spite of its layered structure [2, 14, 15]. It is important to investigate the electronic structure of high temperature phase, because the high temperature phase is deeply related to the emergences of structural phase transition and superconductivity.

Figure 5.2 shows the Fermi surface maps in the k_x - k_z plane (a) and the k_y - k_z plane (b). The dots line indicates the band-structure calculation with the spin-orbit interaction. The strongly three-dimensional Fermi surfaces are observed and roughly consistent with the band-structure calculation with the spin-orbit interaction. As shown in Fig. 5.3, the photon energy dependence of the Fermi surface maps in the k_x - k_y plane is compared with the band-structure calculations for various photon energies. In going from Fig. 5.3 (c) to (g), the shape of calculated inner Fermi surface changes from the six-fold to three-fold symmetry, while the outer Fermi surfaces are insensitive. The observed Fermi surfaces are consistent with the band-structure calculation. According to the calculation, the inner Fermi surface splits into the small pockets and the shape of outer Fermi surfaces changes from the three-fold to six-fold symmetry in the region between Figs. 5.3 (h) and (i). The observed inner and outer Fermi surfaces in Figs. 5.3 (h) and (i), dramatically change with k_z and basically

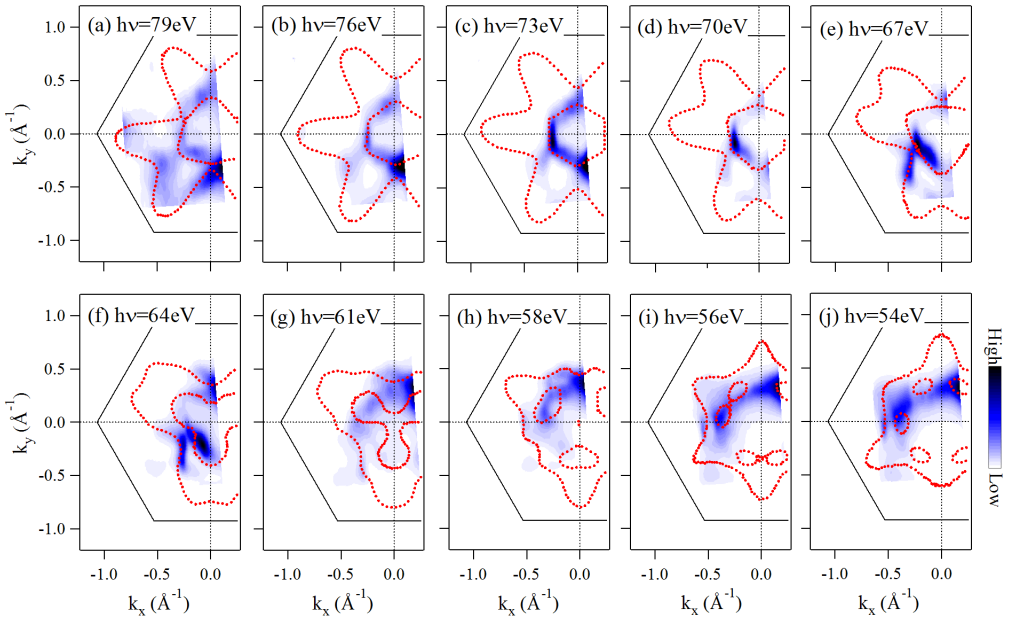

Figure 5.3: Fermi surface maps for $Ir_{0.95}Pt_{0.05}Te_2$ at $h\nu$ = (a) 79 eV, (b) 76 eV, (c) 73 eV, (d) 70 eV, (e) 67 eV, (f) 64 eV, (g) 61 eV, (h) 58 eV, (i) 56 eV and (j) 54 eV, respectively. Dots lines indicate the band-structure calculations with the spin-orbit coulpling.

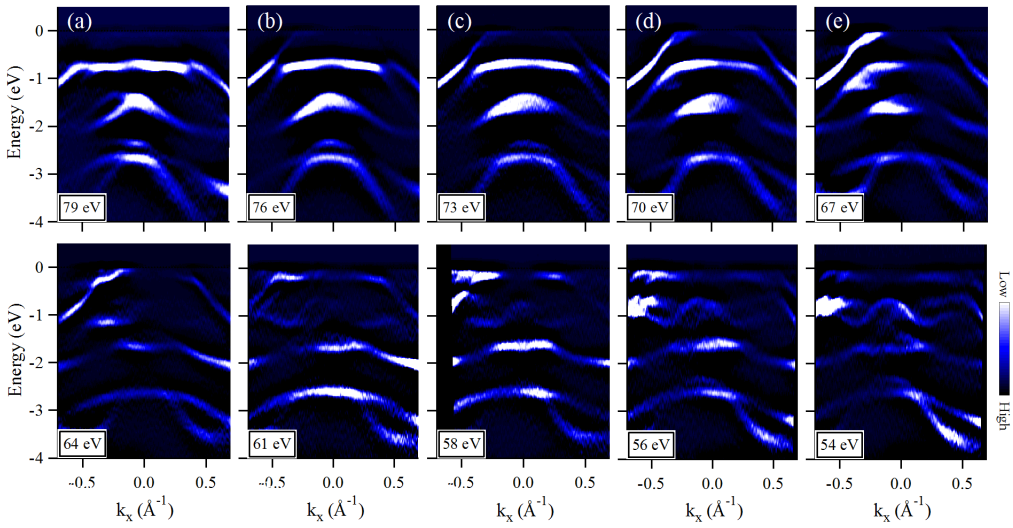

Figure 5.4: Second derivative plots of ARPES spectra for $Ir_{0.95}Pt_{0.05}Te_2$ along the cuts approximately in the Γ-K, A-H direction taken at $h\nu$ = (a) 79 eV, (b) 76 eV, (c) 73 eV, (d) 70 eV, (e) 67 eV, (f) 64 eV, (g) 61 eV, (h) 58 eV, (i) 56 eV and (j) 54 eV, respectively.

agree with the band structure calculation. The photon energy dependence of the band dispersions is displayed in Fig. 5.4. The band dispersions above -1.5 eV are sensitive to the photon energy, whereas the those below -1.5 eV do not strongly depend on the photon energy. The band structures below -1.5 eV, according to the band structure calculation, are derived from the Ir 5d t_{2g} and the Te 5p orbitals. The Ir 5d t_{2g} orbitals are split into the Ir 5d a_{1g} and Ir 5d e'_g orbitals, under the trigonal ligand field of $Ir_{1-x}Pt_xTe_2$. As shown in Fig. 5.5, the Ir 5d a_{1g} and Te 5p_z orbitals are directed in the out-of-plane (z-axis) direction. The Te - Te 5p_z orbitals have the larger Te 5p - 5p transfer integrals between the $IrTe_2$ layers. Thus, the three-dimensional Fermi surfaces and band dispersions are made by the hybridization between the Ir 5d a_{1g} orbital and the Te 5p_z orbital. On the other hand, the Ir 5d e_g^π and Te 5p_x+5p_y orbitals are expected to be two dimensional, because the Ir 5d e_g^π and Te 5p_x+5p_y orbitals are directed in the in-plane (xy-plane) direction. However, this situation is not consistent with the ARPES result. Considering the small charge-transfer energy in $Ir_{1-x}Pt_xTe_2$, the Te 5p orbitals and Ir 5d orbitals strongly hybridize to each other. Threrefore, all the Ir 5d t_{2g} and the Te 5p bands exhibit large three dimensionality in spite of the two dimensional structure of $Ir_{1-x}Pt_xTe_2$.

5.3.3 Roles of spin-orbit interaction at high temperature phase

In this section, we compare the observed Fermi surfaces of $Ir_{0.95}Pt_{0.05}Te_2$ with the band-structure calculations, including the spin-orbit interaction. Figure 5.6 shows the photon energy dependence of Fermi surface maps for $Ir_{0.95}Pt_{0.05}Te_2$ compared with the calculated Fermi surfaces with and without the spin-orbit interactions. According to the electron doping, the band dispersions with (without) spin-orbit interaction are shifted by 0.02768 eV (0.02832 eV) from the undistorted $IrTe_2$. As we mentioned above, the observed Fermi surface maps for 23, 26, 29 eV agree well with the calculated Fermi surfaces with spin-orbit interaction for $k_z = \pi/c$, $9\pi/c$, $8\pi/c$, respectively. The calculations with and without the spin-orbit interaction indicates that the effect of the spin-orbit interaction is more significant for the inner Fermi surfaces than the outer one. Compared with hν = 23 eV, the effect of spin-orbit interaction is more effective at hν = 29 eV. At hν = 29 eV, there is a big difference between the calculated Fermi surfaces without spin-orbit interactions and the ARPES results. On the other hand, the Fermi surfaces calculated with the spin-orbit interaction are consistent with the ARPES results.

Figures 5.7 (a1-3) and (b1-3) show the band dispersions along A-H and A-L

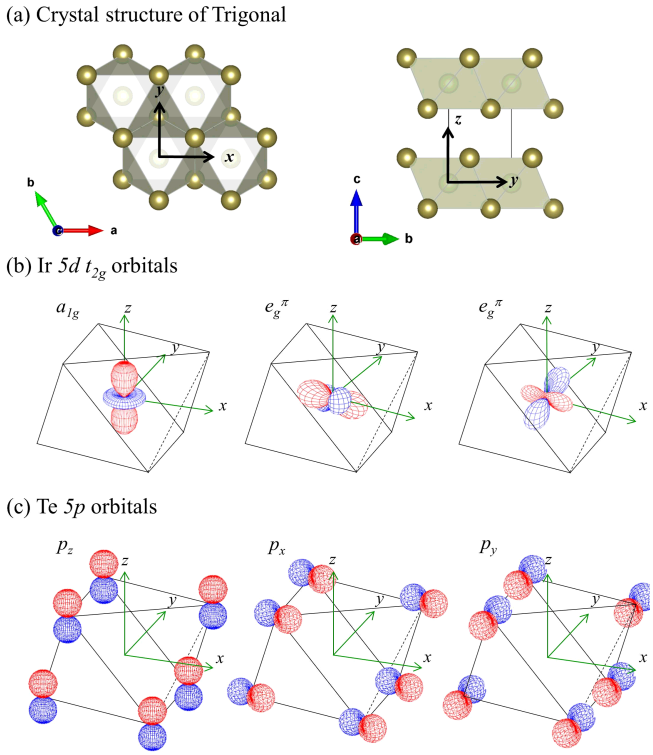

Figure 5.5: (a) Crystal strcuture of trigonal $Ir_{1-x}Pt_xTe_2$. Shapes of Ir $5d$ t_{2g} (b) and Te $5p$ orbitals (c) under trigonal ligand field of $Ir_{1-x}Pt_xTe_2$. Arrows indicate the local coordinate axes (x, y, z).

directions, compared with the band structure calculation with and without the spin-orbit interaction. The spin-orbit interaction produces the band splitting at -0.5 eV between the inner bands around the A point and that at -0.25 eV between the inner and the outer bands in the A-H direction. As a result of the band structure calculation, the inner bands near the A point are mainly constructed from Te $5p_x$ and $5p_y$ orbitals. In going from the A point to the H point, the inner bands tend to have some contribution of the Ir $5d$ e_g orbitals. On the other hand, the outer bands are derived from the Te $5p_z$ orbitals with some contribution of the Ir $5d$ a_{1g} orbitals. Therefore, the band splitting at -0.5 eV around A point and that at -0.25 eV between the outer and inner bands can be attributed from to the $p_x \pm ip_y$ type and $p_z \pm ip_x/p_z \pm ip_y$ type Te $5p$ spin-orbit coupling with some contribution Ir $5d$ spin-orbit coupling, respectively.

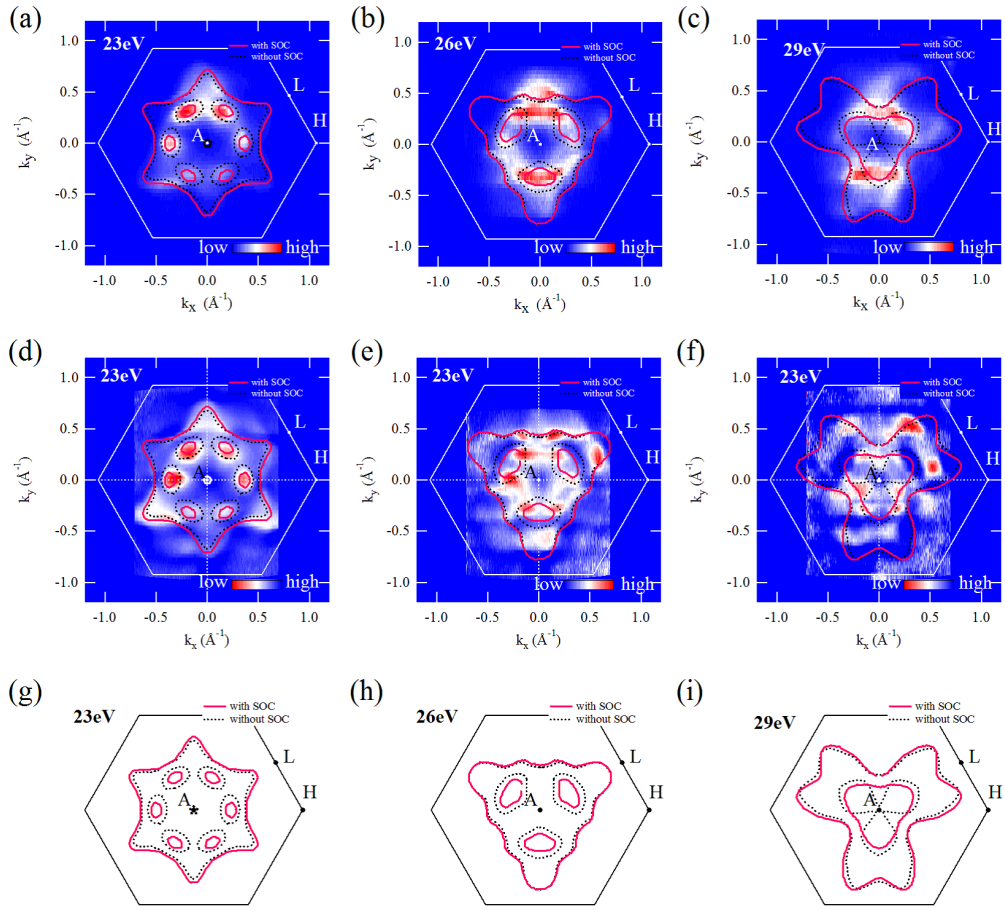

Figure 5.6: Fermi surface maps for $Ir_{0.95}Pt_{0.05}Te_2$ at (a) 23 eV, (b) 26 eV, and (c) 29 eV, respectively. Normalized Fermi surface maps for $Ir_{0.95}Pt_{0.05}Te_2$ at(d) 23 eV, (e) 26 eV, and (f) 29 eV, respectively. Solid lines and Dots lines indicate the band-structure calculations with and without the spin-orbit interaction. The band-structure calculations with and without the spin-orbit interaction for (g) 23 eV, (h) 26 eV, and (i) 29 eV.

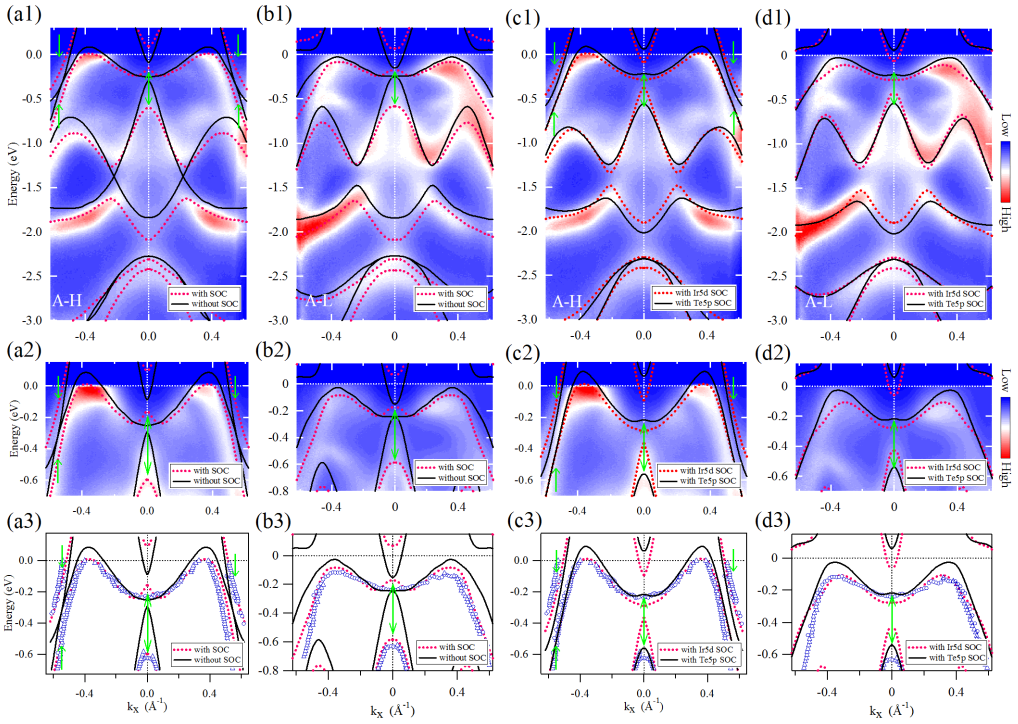

Figure 5.7: ARPES spectra of $Ir_{0.95}Pt_{0.05}Te_2$ along (a1-3) A-H direction and (b1-3) A-L direction compared with the band-structure calculations with and without the spin-orbit interaction. The red dots and black curves indicate the band dispersions calculated with and without the spin-orbit interaction, respectively. ARPES spectra of $Ir_{0.95}Pt_{0.05}Te_2$ along (c1-3) A-H direction and (d1-3) A-L direction compared with the band-structure calculations with (without) the Te 5p (Ir 5d) spin-orbit interaction and that without (with) the Te 5p (Ir 5d) spin-orbit interaction. The red dots and black curves indicate the band dispersions calculated with (without) the Te 5p (Ir 5d) spin-orbit interaction and that without (with) the Te 5p (Ir 5d) spin-orbit interaction. The green arrows indicate the spin-orbit splitting. The blue open circles and triangles indicate the peak positions of the momentum distribution curves (MDC) and the energy distribution curves (EDC), respectively.

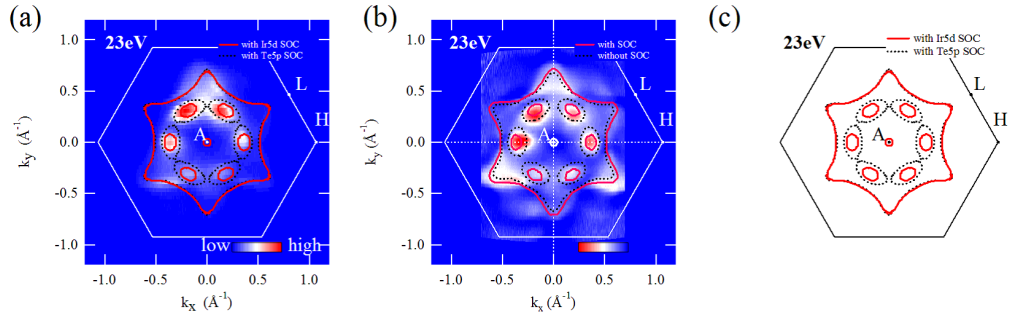

Figure 5.8: (a) Fermi surface maps for $Ir_{0.95}Pt_{0.05}Te_2$ at 23 eV, and (b) Normalized Fermi surface map for $Ir_{0.95}Pt_{0.05}Te_2$ at 23 eV. The band-structure calculation with (without) the Te 5*p* (Ir 5*d*) spin-orbit interaction and that with (without) the Ir 5*d* (Te 5*p*) compared with the Fermi surface map at 23 eV. (c) The band-structure calculation with (without) the Te 5*p* (Ir 5*d*) spin-orbit interaction and that with (without) the Ir 5*d* (Te 5*p*) for 23 eV.

In order to clarify the different roles of the Te 5*p* and Ir 5*d* spin-orbit-coupling, Figures 5.8 and 5.7 (c1-3),(d1-3) show the Fermi surface maps and the band dispersions of $Ir_{0.95}Pt_{0.05}Te_2$ along the A-H and A-L directions, compared with the band-structure calculations with (without) the Te 5*p* (Ir 5*d*) spin-orbit interaction and that without (with) the Te 5*p* (Ir 5*d*) spin-orbit interaction. The Fermi surface maps agree with the band-structure calculations with (without) the Ir 5*d* (Te 5*p*) spin-orbit interactions than that with (without) the Te 5*p* (Ir 5*d*) spin-orbit interaction in Fig. 5.8. This indicates that the Ir 5*d* spin-orbit interaction is more important for the inner Fermi surfaces. Although the Te 5*p* spin-orbit interaction induces the band splitting at -0.25 eV between the inner and outer bands in the A-H cut, the magnitude of the splitting is much more enhanced by the inclusion of the Ir 5*d* spin-orbit coupling. Therefore, the spin-orbit coupling between the Ir 5*d* a_{1g} and Ir 5*d* e_g orbitals substantially contributes to the coupling between the inner and outer bands, while the inner and outer bands are mainly characterized by the Te 5*p* orbitals.

In $Ir_{1-x}Pt_xTe_2$, the inner and outer bands are very close to each other near the Fermi level along the A-H direction, and the Te 5*p* and Ir 5*d* spin-orbit interactions introduce the strong entanglement between the spin and orbital parts of the electrons. The recent ARPES study on Sr_2RuO_4 revealed that the strong spin-orbital entanglement provides mixing of spin-singlet and spin-triplet Cooper pairs and may cause an exotic superconducting state [13]. Since the magnitude of the spin-orbit interaction in $Ir_{0.95}Pt_{0.05}Te_2$ is much stronger than that in Sr_2RuO_4, one can expect stronger mixing between spin-singlet

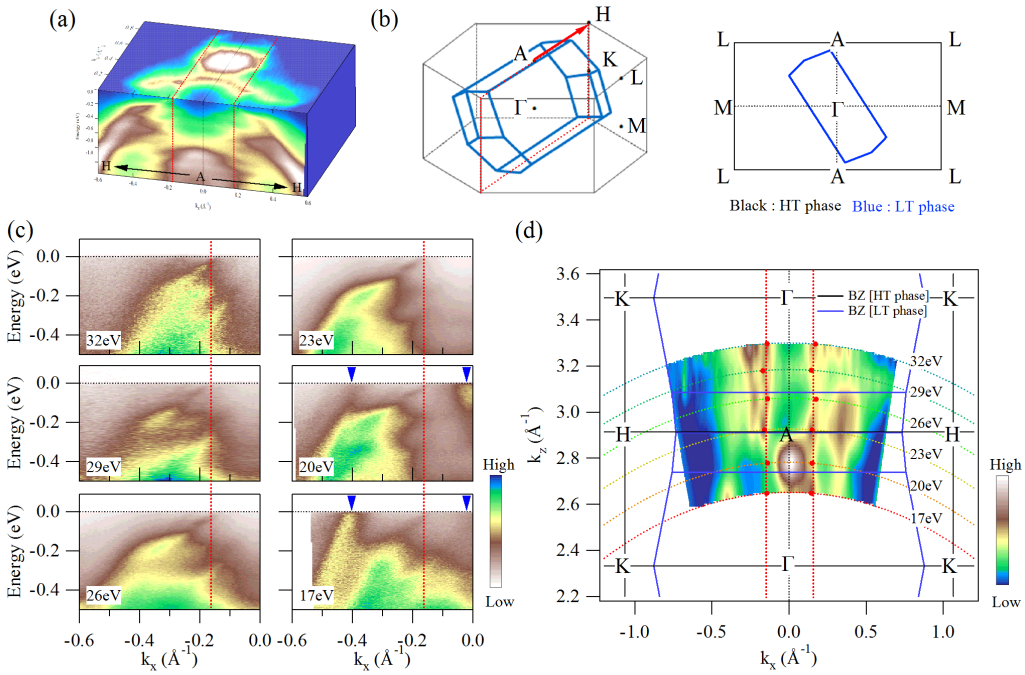

Figure 5.9: (a) Fermi surface map for $IrTe_2$ at $h\nu = 23$ eV. (b) Relation between the trigonal (black) and the triclinic (blue) Brillouin zone. (c) ARPES spectra of $IrTe_2$ along the Γ-K or A-H direction (k_x direction) taken at 20 K and $h\nu =$ 32, 29, 26, 23, 20, and 17 eV. The dotted lines roughly indicate the Fermi wave number at which the surface band crosses the Fermi level. (d) Fermi surface map in the k_x - k_z plane. k_z is the electron momentum perpendicular to the cleaved surface.

and spin-triplet Cooper pairing in $Ir_{0.95}Pt_{0.05}Te_2$.

5.3.4 Electronic structure of $IrTe_2$ at low temperature phase

We have observed the drastic change of the Fermi surface with the structural phase transition in the previous ARPES study [9]. These data were collected at the photon energy $h\nu = 23$ eV which corresponds to the A point in the hexagonal Brillouin zone. At the low temperature phase, the straight Fermi surface was observed, indicating the Ir $5d$ and/or Te $5p$ orbital symmetry breaking. This result is, however, inconsistent with the band structure calculation [10, 11]. Therefore, we have measured the photon energy dependence of ARPES in order to clarify the origin of the straight Fermi surface observed in $IrTe_2$. Figure 5.9 shows the Fermi surface map taken at $h\nu = 23$ eV and the

band dispersions along A-H (Γ-K) direction taken at $h\nu$ = 32, 29, 26, 23, 20, and 17 eV. The Fermi surface map at $h\nu$ = 23 eV exhibits the straight Fermi surface which was reported in our previous ARPES study [9] in Fig. 5.9 (a). In Fig. 5.9 (c), the one-dimensional band dispersions, which create the straight Fermi surfaces, do not depend on the photon energy, while the spectral weight depends on the photon energy. The Fermi surface map in $k_z - k_x$ plane is displayed in Fig. 5.9 (d). Here, k_x is the momentum along A-H direction, and k_z is the momentum perpendicular to the surface. The red dots represent the k_F positions corresponding to the straight Fermi surfaces taken at $h\nu$ = 32, 29, 26, 23, 20, and 17 eV. This result indicates that the straight Fermi surfaces do not change appreciably with the photon energy. In contrast, the other complicated Fermi surfaces strongly depend on the photon energy. Therefore, the straight Fermi surface originates from the surface state of $IrTe_2$. On the other hand, the complicated Fermi surfaces with the strong k_z dependence can be assigned to the bulk of $IrTe_2$ with Ir/Te orbital and charge order.

- **Surface state of $IrTe_2$ at low temperature phase**

  First, we describe the surface state of $IrTe_2$ at the low temperature phase. The straight Fermi surfaces are derived from the very one-dimensional band dispersion along the k_x direction. Here, it should be noted that the kink structures of the one-dimensional band dispersion are observed near the Fermi level in Fig. 5.10. In order to determine the energy scale of kink structures, we estimated the MDC peak width Δk and Δk multiplied by the group velocity v_G. The energy positions of the kink structures are located at ∼47 meV and ∼110 meV. Compared with the bulk sensitive Raman spectroscopy, the energy scales of the kink structures ∼47 and ∼110 meV are completely different from the reported phonon modes of ∼21.7, ∼20.5, ∼16.9, ∼16.3, ∼15.6, and 14.6 meV [12]. This result suggests that the observed kink structures originate not from the bulk state of the low temperature phase but from the surface state with the relatively large phonon modes. In addition to the main one-dimensional band dispersion, several branches are clearly observed well below the Fermi level in Fig. 5.10. Figure 5.10 shows the photon energy dependence of energy distribution curve (EDC) obtained from k_x = -0.17Å^{-1} in Fig. 5.10 (c). The peak structures of EDCs correspond to the several branches of the one dimensional band dispersion and do not depend on the photon energy. This indicates that these branches are the surface states as well as the one-dimensional band dispersion. In order to further clarify the several branches, we subtracted Shirley background

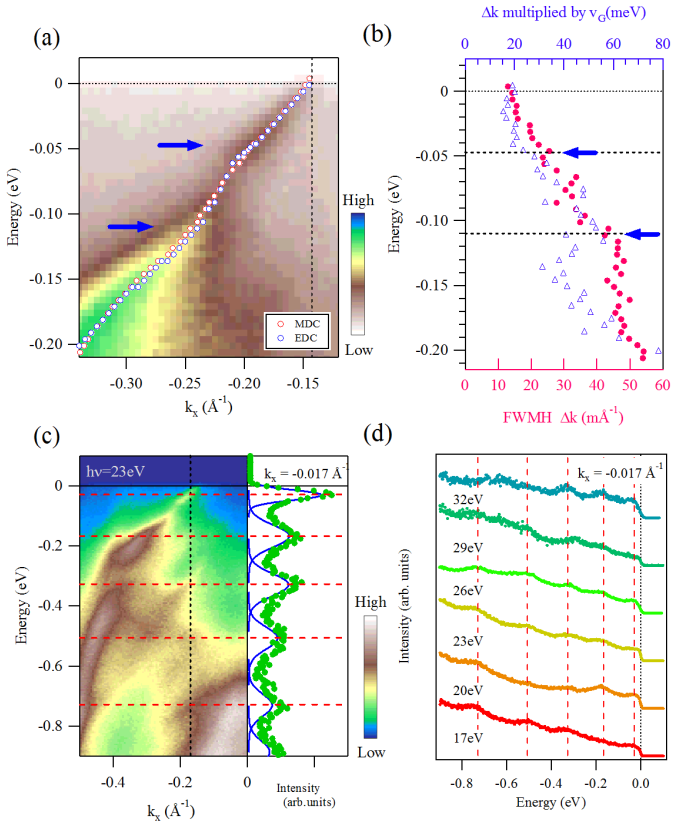

Figure 5.10: (a) One-dimensional band dispersion along the A-H direction (k_x direction) taken at $h\nu = 23$ eV. Red and blue dots represent the peak positions obtained from MDCs and EDCs, respectively. (b) MDC peak width Δk and Δk multiplied by the group velocity v_G. The positions of the kink structure at $\sim$ 47 meV and $\sim$ 110 meV are shown by the blue arrows. (c) The broad range dispersion of (a) and the background substructed EDC. (d) Photon energy dependence of EDCs obtained from k_x= -0.017Å. Red dotted lines correspond to the peak positions of EDCs.

from EDC as shown in Fig. 5.10 (b). These branches suggest that the electrons are confined along the y and z directions. Since the velocity of the confined electron V_F is $\sim$ 1 eV/Å^{-1} and the energy separation between the neighboring branches ΔE is $\sim$ 0.15 eV, the length scale of the confinement would be $\pi V_F/\Delta E \sim 21$ Å. This value is comparable to the distance between the stripes of the Ir-Ir dimers at distorted phase. Therefore, the one-dimensional band dispersion runs along the stripe of Ir-Ir dimers and is accompanied by several branches which can be derived from the quantization in the perpendicular direction to the stripe.

- **Bulk state of $IrTe_2$ at low temperature phase**
  As we mentioned above, the observed band dispersions can be distinguished into the surface state and the bulk state by using the photon energy dependence. For example, the observed band dispersions at k_x $\sim$ 0 and -0.4 Å for $h\nu$ = 17 and 20 eV (marked by the closed triangles in Fig. 5.9 (c)) disappear from the different photon energies. This indicates that the obtained band dispersions include not only the surface state but also the bulk state. Figure 5.11 shows the Fermi surface maps and band dispersions taken at $h\nu$ = (a) 32 eV, (b) 29eV , (c) 26 eV, (d) 23 eV, (e) 20 eV, and (f) 17 eV. The straight Fermi surfaces are clearly observed from $h\nu$ = 32 to 23 eV. Considering the Brillouin zone at low temperature phase as shown in Fig. 5.11, the Fermi surfaces at $h\nu$ = 20 and 17 eV should be the same Fermi surfaces at $h\nu$ = 26 eV and 29 eV, respectively. However, the shapes of Fermi surfaces of $h\nu$ = 20 and 17 eV are appreciably different from those of $h\nu$ = 32 - 23 eV. Although the several branches of the one dimensional band dispersions, as we discussed above, are observed over the whole measured photon energy as shown in Fig. 5.11, the spectral weights of the straight Fermi surface of $h\nu$ = 20 and 17 eV are relatively suppressed. The band dispersions do not change in going from $h\nu$ = 32 to 23 eV. In contrast, the band dispersions at $h\nu$ = 20 and 17 eV deviate from those of $h\nu$ = 32 to 23 eV. In particular, the electron-like band around k_x = 0 Å are observed in $h\nu$ = 20 eV (Fig. 5.11 (f3)). These results indicate that the bulk feature of Fermi surfaces is emphasized in $h\nu$ = 20 and 17 eV. Therefore, we compare the observed Fermi surfaces taken at $h\nu$ = 20 and 17 eV with the calculated Fermi surfaces in order to determine the ground state of low temperature phase. Figures 5.12 (a) and (c) show the Fermi surfaces at $h\nu$ = 20 eV and 17 eV, compared with the band structure calculation with the superstructure $q_{1/5}$ unfolded into the hexagonal Brillouin zone for different k_z in Figs. 5.12 (b) and (d) [10]. The observed Fermi surfaces maps taken at $h\nu$ = 20 eV and 17 eV are in good agreement with

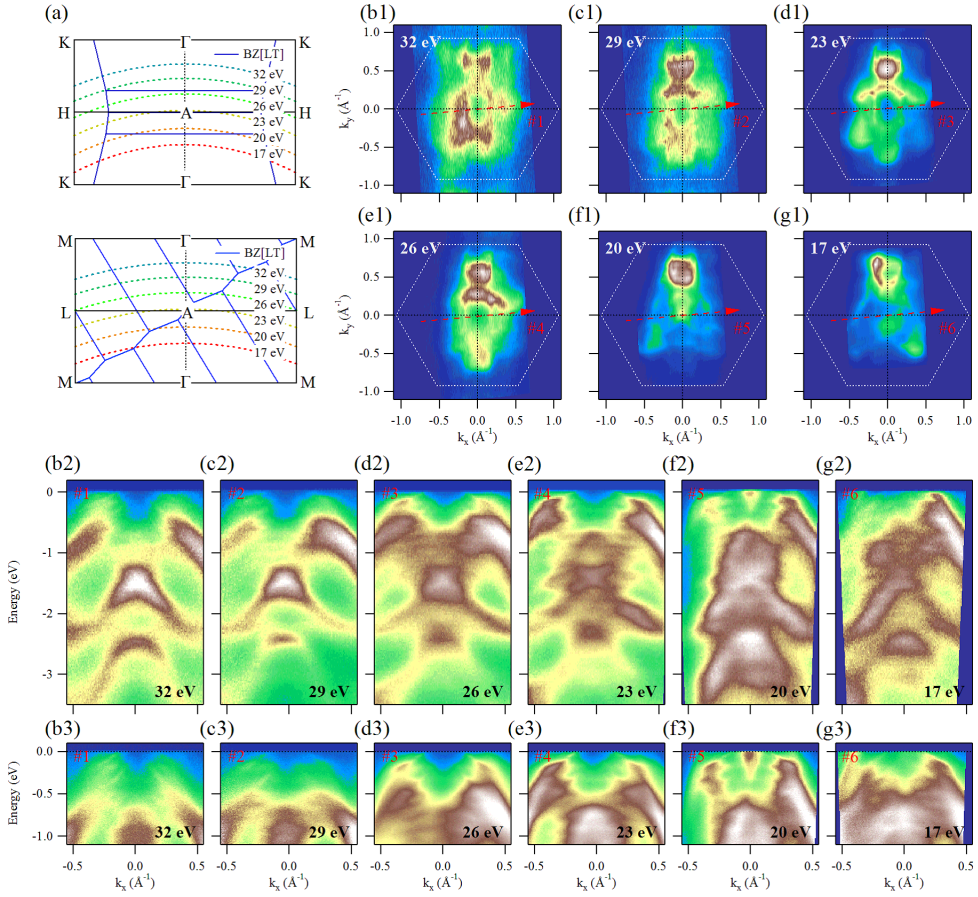

Figure 5.11: (a) Relation between the trigonal (black) and the triclinic (blue) Brillouin zone in k_z - k_x plane and k_z - k_y plane. Fermi surface maps, broad-range band dispersions, and near-E_F band dispersions taken at $h\nu$ = (b1-b3) 32 eV, (c1-c3) 29eV , (d1-d3) 26 eV, (e1-e3) 23 eV, (f1-f3) 20 eV, (g1-g3) 17 eV, respectively.

the calculated Fermi surfaces for $k_z = 0.4$ and 0.3 [10]. The ARPES data taken at $h\nu = 20$ eV and 17 eV are corresponding to the red and orange arrows in the Brillouin zone at the low temperature phase in Fig. 5.12 (f). The band structure calculation predicts that the Fermi surfaces consist of the five hole bands. The two cylindrical hole pockets are located at the Y point. The M-shaped hole band dispersions along X′-V′ direction cross the Fermi level near the X′ point and create the electron pockets. The observed band dispersions in cuts #1 and #2 clearly show the electron-like and the hole-like band dispersions. Compared to the calculated Fermi surface, the electron-like band corresponds to the electron pocket around X′ point. On the other hand, the positions of hole bands are roughly consistent with the band structure calculation. The observed Fermi surfaces and band dispersions basically agree with the band structure calculation with the superstructure $q_{1/5}$. Consequently, we conclude that the ground state at low temperature phase with the modulation vector $q_{1/5}$ is realized, which is consistent with the result of x-ray diffraction measurement by Toriyama *et al.* [15].

5.4 Summary

We have performed the photon energy dependence of angle-resolved photoemission spectroscopy using the synchrotron light source in order to investigate the electronic structure of $Ir_{1-x}Pt_xTe_2$. First, we summarize the electronic structure of the high temperature phase. At the high temperature phase, the three-dimensional Fermi surfaces and the band dispersions of $Ir_{1-x}Pt_xTe_2$ qualitatively agree with the band structure calculation with the spin-orbit interaction. The three-dimensionality comes from the strong Te $5p$ - $5p$ hybridization and the heavily mixing between the Ir $5d$ t_{2g} and Te $5p$ orbitals. The effects of the Ir $5d$ and Te $5p$ spin-orbit interactions are emphasized in the region where the inner and the outer bands close to each other, which may introduce the exotic superconducting state.

Then, we summarize the electronic structure of the low temperature phase. At the low temperature phase, the observed Fermi surfaces and band dispersions can be distinguished from the surface state and bulk state by using the photon energy dependence. The straight Fermi surface, which made by the very one-dimensional band dispersions, and the several branches do not change with the photon energy suggesting the surface state. The one-dimensional band dispersion exhibits the kink structures with the large phonon mode. In addition to the main one-dimensional band, the observed several branches suggest that the electrons are confined along the y and z directions. The bulk fea-

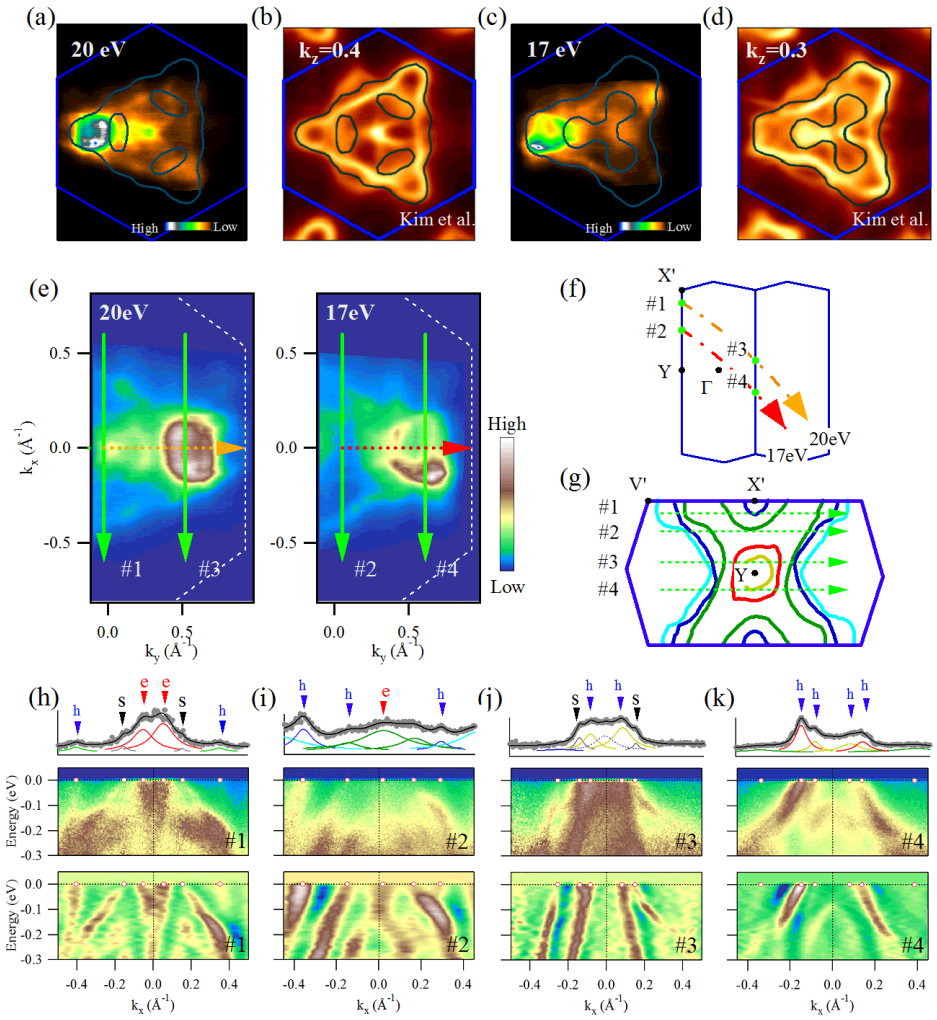

Figure 5.12: Fermi surface maps of $IrTe_2$ for (a) $h\nu = 20$ eV and (c) 17 eV taken at 20K. The photon energies of $h\nu = 20$ eV and 17 eV coressponds to k_z ~0.4 and 0.3, respectively. Band structure calculations with the superstructure $q_{1/5}$ unfolded into the hexagonal Brillouin zone (b) $k_z = 0.4$ and (d) 0.3 [10]. (e) An enlarged view of Fermi surface maps (a) and (d). (f) Brillouin zone of low temperature phase in k_z - k_y plane. Fermi surface maps for $h\nu = 20$ eV and 17 eV are corresponding to the red and orange arrows. (g) Illustration of the Fermi surface with the superstructure $q_{1/5}$ at low temperature phase. The band calculation [15] is used as reference. The green arrows correspond to the cuts #1 - 4 of (e). (h)-(k) Band dispersions and its second derivative plots along the cuts #1 - 4. The Fermi wave number k_F is marked by the closed triangle.

tures of the Fermi surfaces and band dispersions are basically consistent with the band structure calculation with the superstructure $q_{1/5}$. Therefore, the observed Fermi surfaces show the realization of a novel two-dimensional electronic structure which is totally different from the three-dimensional Fermi surfaces of the high temperature phase. The drastic change of the dimensionality indicates that the charge-orbital ordering is governed by the local Ir-Ir, Ir-Te, and Te-Te bonding.

References

[1] S. Pyon, K. Kudo, and M. Nohara, Physica C **494**, 80-84 (2013)

[2] A. F. Fang, G. Xu, T. Dong, P. Zheng, and N. L. Wang, Sci. Rep. **3**, 1153 (2013).

[3] K. Kudo, M. Kobayashi, S. Pyon, and M. Nohara, J. Phys. Soc. Jpn. **82** 085001 (2013)

[4] S. Pyon, K. Kudo, and M. Nohara, J. Phys. Soc. Jpn. **81**, 053701 (2012).

[5] J. J. Yang, Y. J. Choi, Y. S. Oh, A. Hogan, Y. Horibe, K. Kim, B. I. Min, and S-W. Cheong, Phys. Rev. Lett. **108**, 116402 (2012).

[6] T. Qian, H. Miao, Z. J. Wang, X. Shi, Y. B. Huang, P. Zhang, N. Xu, L. K. Zeng, P. Richard, M. Shi, G. Xu, X. Dai, Z. Fang, A. F. Fang, N. L. Wang, and H. Ding, New J. Phys. **16**, 123038 (2014)

[7] Y. Fujisawa, T. Machida, K. Igarashi, A. Kaneko, T. Mochiku, S. Ooi, M. Tachiki, K. Komori, K. Hirata, and H. Sakata, J. Phys. Soc. Jpn. **84**, 043706 (2015).

[8] W. Ruan, P. Tang, A. Fang, P. Cai, C. Ye, X. Li, W. Duan, N. Wang, and Y. Wang, Science Bulletin, **60**, 8, 798-805 (2015)

[9] D. Ootsuki, S. Pyon, K. Kudo, M. Nohara, M. Horio, T. Yoshida, A. Fujimori, M. Arita, H. Anzai, H. Namatame, M. Taniguchi, N. L. Saini, and T. Mizokawa, J. Phys. Soc. Jpn. **82**, 093704 (2013).

[10] Kyoo Kim, Sooran Kim, K. -T. Ko, Hwangho Lee, J. -H. Park, J. J. Yang, S. -W. Cheong, and B. I. Min, Phys. Rev. Lett. **114**, 136401(2015).

[11] Kyoo Kim, Sooran Kim, and B. I. Min, Phys. Rev. B **90**, 195136(2014).

[12] N. Lazarevič, E. S. Bozin, M. Šcepanović, M. Opačić, Hechang Lei, C. Petrovic, and Z. V. Popović, Phys. Rev. B **89**, 224301 (2014)

[13] C. N. Veenstra, Z. -H. Zhu, M. Raichle, B. M. Ludbrook, A. Nicolaou, B. Slomski, G. Landolt, S. Kittaka, Y. Maeno, J. H. Dil, I. S. Elfimov, M. W. Haverkort, and A. Damascelli, Phys. Rev. Lett. **112**, 127002 (2014)

[14] J. J. Yang, Y. J. Choi, Y. S. Oh, A. Hogan, Y. Horibe, K. Kim, B. I. Min, and S-W. Cheong, Phys. Rev. Lett. **108**, 116402 (2012).

[15] T. Toriyama, M. Kobori, T. Konishi, Y. Ohta, K. Sugimoto, J. Kim, A. Fujiwara, S. Pyon, K. Kudo, and M. Nohara, J. Phys. Soc. Jpn. **83**, 033701 (2014).

[16] G. L. Pascut, K. Haule, M. J. Gutmann, S.A. Barnett, A. Bambardi, S. Artyukhin, T. Birol, D. Vanderbilt, J. J. Yang, S-W. Cheong, and V. Kiryukhin, Phys. Rev. Lett. **112**, 086402 (2014).

Chapter 6

Angle-resolved photoemission microscopy of $IrTe_2$

In this chapter, we describe the spatial distribution of electronic structure in $IrTe_2$ using the angle-resolved photoemission microscopy.

6.1 Introduction

In chapter 5, we have investigated the electronic structures of the high temperature phase and the low temperature phase. The observed Fermi surfaces at the high and low temperature phases are basically consistent with the prediction of the band structure calculation by Toriyama *et al.* and Pascut *et al.* [1, 2]. Across the structural phase transition, $IrTe_2$ exhibits the drastic change of the conducting planes with symmetry breaking. When a solid undergoes a first order phase transition with some symmetry breaking, the high temperature phase and the low temperature phases often coexist and form domains with the finite temperature range. Therefore, we have investigated the spatial distribution of the electronic structure by angle-resolved photoemission microscopy.

6.2 Experiment

Single crystal samples of $IrTe_2$ were prepared using a self-flux method as reported in the literatures [3]. The photoemission microscopy results were obtained on the spectromicroscopy beamline at the Elettra synchrotron facility at Trieste [4]. Photons at 27 eV and 74 eV were focused through a Schwarzschild objective, to obtain a submicron size spot. This allows us to map the inhomogeneous distribution of the electronic structure at the Fermi level as well

as that of the core levels. For the present measurements the total energy resolution was about 50 meV while the angle resolution was limited to 1 degree. The measurements were performed in ultra-high vacuum on an in-situ prepared surfaces. A standard photoemission microscopy procedure was used to remove topographic features from the images presented [5]. The single crystal $IrTe_2$ was cleaved at 300K under the ultra high vacuum.

6.3 Results and discussion

Figure 6.1 shows the temperature evolution of the photoemission intensity images. Each pixel corresponds to the integrated value of the photoemission intensity. At 300K, the photoemission intensity image does not show any real-space structure as shown in Fig. 6.1 (a). When the sample was cooled to 286K, the real-space stripy structures appear in the photoemission intensity image (Fig. 6.1 (b).). The contrast between bright and the dark regions becomes clear and the stripy domains are observed in going from 279K to 267K well below the structural phase transition. The high and low intensities directly reflect the difference of the electronic structure. Figure 6.2 (a) shows the photoemission spectra at 300K and 267K. Each spectrum shows the several structures (marked by the bars in Fig. 6.2 (a)).

The photoemission spectrum of the bright region at 267K is similar to that taken at 300K. On the other hand, the photoemission spectrum at 300K is different from that of dark region at 267K. The difference between these photoemission spectra can be seen clearly. Compared with the photoemission spectrum at 300K, the structure from -0.7 eV to -1.7 eV is broadened in the photoemission spectrum of the dark region, reflecting the formation of the stripe-type charge ordering. The photoemission spectrum obtained from the dark region at 267K is roughly consistent with the previous results of the photoemission spectroscopy and the band structure calculation of the low temperature phase [1, 2, 7].

In order to discuss the detail of the difference between the bright and dark regions, we have performed the angle-resolved photoemission spectroscopy (ARPES) at 300K and 230K. Here, we prepared the new cleavage surface and confirmed the reproducibility of the photoemission spectra and the appearance of the bright and dark stripes at 230K. The band dispersions at 300K and 230K are displayed in Figs. 6.2 (b)-(d). The band dispersion at 300K qualitatively agrees with the band structure calculation [9].

Across the structural phase transition, the band dispersion of the bright region is basically similar to that of 300K. However, the difference between the band dispersions of 300K and that of the bright and dark regions at 230K

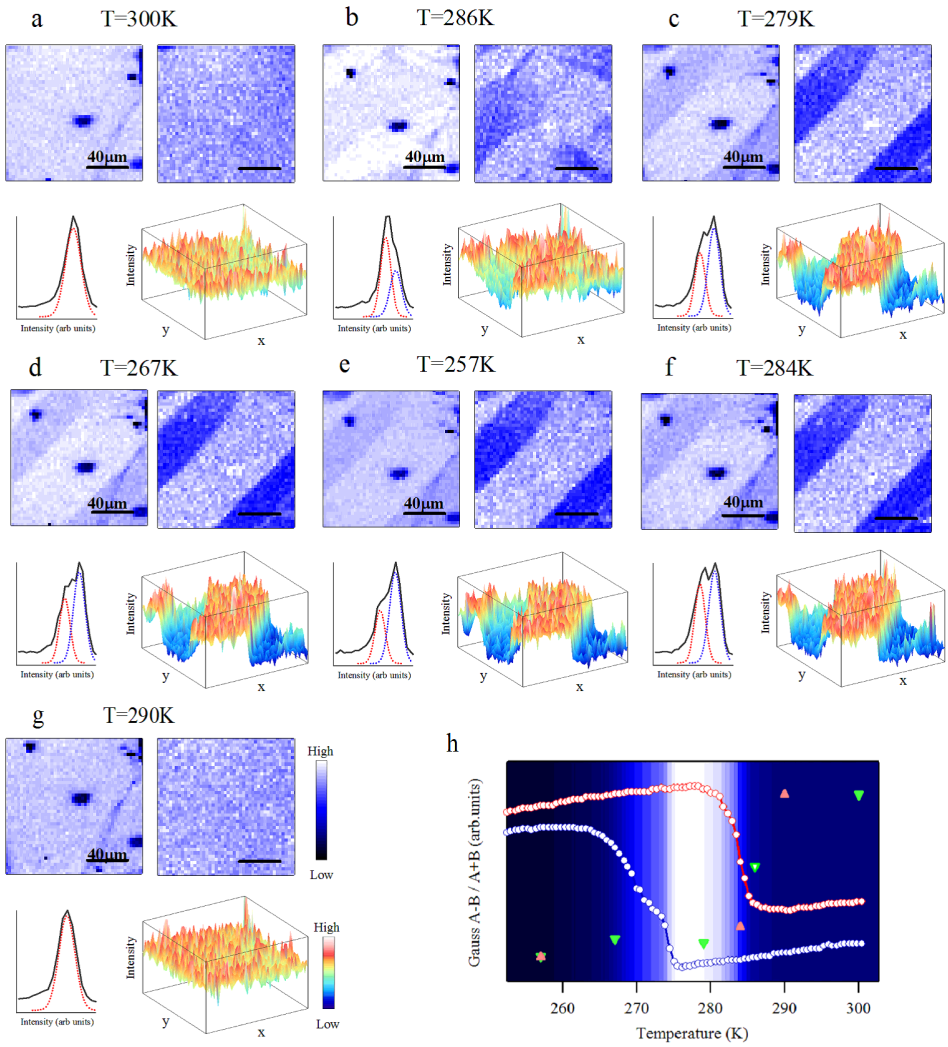

Figure 6.1: Image of photoemission intensity integrated in the energy window from 0.1 to -2.3 eV, image of normalized photoemission intensity, distribution of photoemission intensity, and volume plot of normalized photoemission intensity taken at (a) 300K, (b) 286K, (c) 279K, (d) 267K, (e) 257K, (f) 284K, and (e) 290K. (h) Temperature dependence of the relative population between the bright and dark regions. The resistivity on cooling (blue circles) and heating (Red circles) [3]. Color map indicates the difference between the resistivities on cooling and heating.

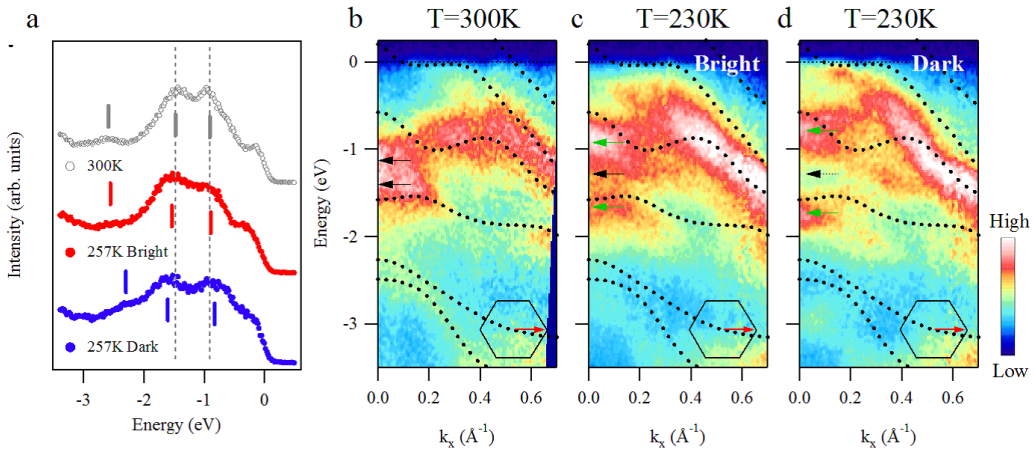

Figure 6.2: (a) Photoemission spectra at 300K and 257K. The data at 257K are obtained from the bright and dark regions in Fig. 6.1 (e). (b) Band dispersion at 300K. Band dispersions of (c) the bright region and (d) the dark region at 230K. The dots curves indicate the band strcutrue calculation for $h\nu = 27$ eV [9]

exists. The energy splitting between the two spectral peaks around -1.0 eV at the zone center increases in going from 300 K to 230 K (bright) to 230 K (dark). This behavior agrees with the prediction by the band structure calculation, reflecting the charge ordering at the low temperature phase [8]. Therefore, the bright region below the structural phase transition would be different from the high temperatrue phase, although the bright regions supposed to have the electronic structures similar to the high temperature phase.

In the bright region, the energy splitting becomes smaller in going from the dark region to the bright region marked by the green arrows in Figs. 6.2 (b)-(d). Based on this result, one can speculate the origin of the dark region. One possibility is that the coexistance of the low temperature phases with the superstructure $q_{1/5}$ and the other modulation vector such as $q_{1/8}$ induces the reduction of the splitting width. Ko *et al*. have suggested the structural phase transition from $q_{1/5}$ to $q_{1/8}$ phase with temperature by x-ray diffraction measurement and also reported the difference of the photoemission spectra according to the different superstructure [7]. However, the photoemission spectra of the $q_{1/5}$ phase and $q_{1/8}$ phase do not show the splitting as we observed. Therefore, we exclude the coexistence of the two low temperature phases. Another possibility is that the anisotropic pressure effect from the neighboring dark domains causes the splitting of the spectral weight, but the stripe-type charge order is still suppressed in the bright region.

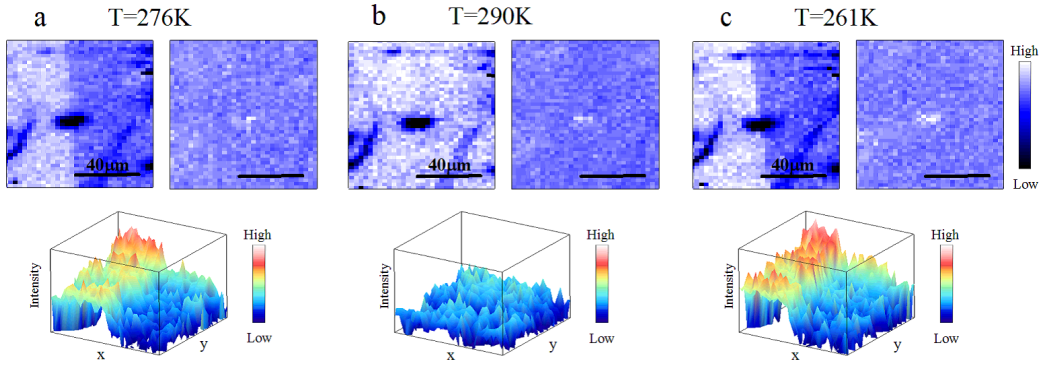

Figure 6.3: Image of photoemission intensity integrated in the energy window from 0.1 to -2.3 eV, image of normalized photoemission intensity, and volume plot of photoemission intensity taken at (a) 276K, (b) 290K,(c) 261K

In the dark region, the band dispersion is similar to the previous ARPES result in very low temperature which were discussed in chapter 5. However, it should be noticed that the observed band dispersion should contain the bulk and surface states as we mentioned in chapter 5. The surface states are relatively emphasized near the Fermi level in the photon energy $h\nu$=27 eV. However, the band structures well below the Fermi level depend on the photon energy, reflecting the bulk states. Furthermore, the effect of the surface state is avoided since the spectral features at the zone center in the dark region are away from the one-dimensional band dispersion and its branches. Therefore, the dark region corresponds to the stripe-type charge order phase with the superstructure $q_{1/5}$ which are identified by the various experiments [1, 2, 8, 10]

The direction of stripy domains can be rotated by annealing. After keeping the sample at 300K for 8 hours, the sample was cooled to 276K and the photoemission intensity image of the same region of Fig. 6.1 was taken which is displayed in Fig. 6.3. The vertical stripy domains are observed at 276K. Compared with the stripy domain in Fig. 6.1, the direction of the stripy domain is rotated by ∼120 degrees. Therefore, the direction of stripy domains is closely related to the Ir - Ir bond direction. Most probably, the rotation of the domains is governed by the rotation of the stripe-type charge order as shown in Fig. 6.4. Indeed, these stripy domains are confirmed above and below the structural phase transition in Figs. 6.3 (a)-(c). The normalized photoemission intensity images are displayed in Fig. 6.3. In the normalized images, the domains are not observed, while the raw data and the volume plots taken from the raw data clearly show the difference between the bright and dark regions. This indicates that the difference of the photoemission spectra between the

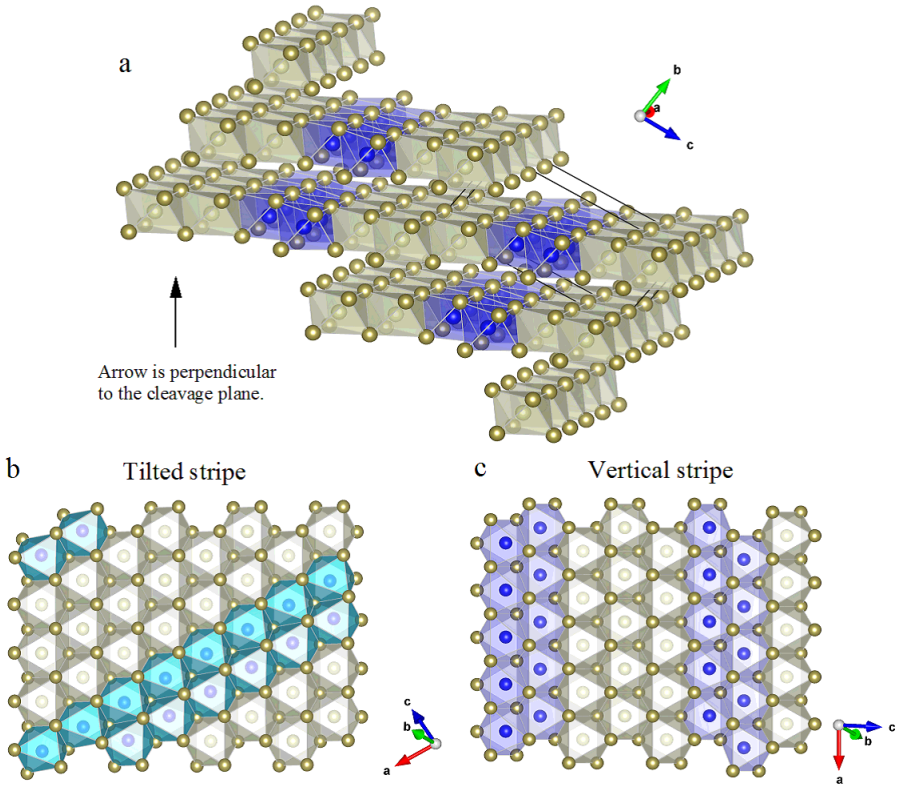

Figure 6.4: (a) Crystal structure at low temperature phase with the superstructure $q_{1/5}$. Schematic picture at the low temperature phase rotated by (b) tilted stripe and (c) vertical stripe, visualized by using the software package VESTA [11].

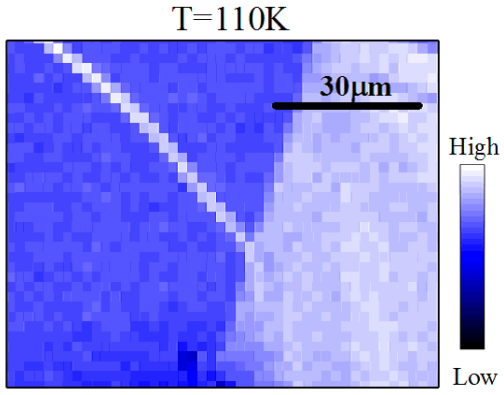

Figure 6.5: Image of photoemission intensity integrated in the energy window from 0.1 to -2.3 eV at 110K.

bright and dark regions becomes small, compared with that of the tilted stripy domains as shown in Fig. 6.1. This observation is consistent with the fact that the vertical stripes are missing in Fig. 6.1 (b), where the stripy domains along the other two directions are observed. The suppression of the difference between the bright and dark regions can be explained by the polarization dependence of the light. In the present experiment, the data were collected using the linear polarized light, which has the polarization vector in the horizontal plane. The vertical stripes are perpendicular to the polarization vector in this setup. In consequence, the difference between the bright and dark region should be small.

The photoemission intensity distribution of pixels is plotted in Fig. 6.1. In order to quantify the evolution of the stripy domains, the photoemission intensity distributions are fitted to two Gaussians, which correspond to the dark region and the bright region, respectively. Although the photoemission intensity distribution shows the single peak (red curve) at 300K in Fig. 6.1 (a), the different peak (blue curve) on the lower intensity side appears at 286K, according to the emergence of the domains in Fig. 6.1 (a). Note that the clear single domains are still not observed at 286K, while the domains start to grow.

In going from 286K to 279K (Fig. 6.1 (c)) and 257K (Fig. 6.1 (d)), the peak on the lower intensity side (blue curve) becomes dominant according to the decrease of the peak on the higher intensity side (red curve). On heating from 257K to 284K, the dominant peak on the lower intensity side decrease and disappears at 290K. Therefore, the peaks on the lower (higher) intensity side can be assigned to the dark (bright) region with (without) the stripe-type charge order. These results indicate the coexistence of the bright and dark regions. Figure 6.1 (h) shows the relative population between the bright and dark regions. The relative population between the bright and dark region clearly shows the step-like behavior just below the structural transition temperature. The stripe-type charge order of the dark region does not show hysteresis or has very small hysteresis if it exists. On the other hand, the bright region remains down to 257K without appreciable shrinking. Interestingly, the stripy domains are still observed at 110K as shown in Fig. 6.5, indicating that the two different phases coexist below the structural phase transition. Here, one can speculate that the hysteresis observed in the resistivity and the scanning tunneling microscopy is related to the robustness of the mesoscopic stripy domain.

6.4 Summary

We have performed the angle-resolved photoemission microscopy in order to investigate the spatial distribution of the electronic structure. The mesoscopic stripy domain derived from the stripe-type charge order of the low temperature phase is observed. The observed bright and dark regions can be assigned to the two phases with and without the stripe-type charge order, respectively. Interestingly, the stripy domain remains down to 110K, indicating that the two different phases coexist below the structural phase transition. The two phases with and without the stripe-type charge order have the different volumes. Therefore, the stripy domain of the stripe-charge order state is under anisotropic strain from the neighboring domains. The strain is expected to enhance the orbital anisotropy of the Te $5p$ and Ir $5d$ orbitals and to align direction of charge stripe.

References

[1] T. Toriyama, M. Kobori, T. Konishi, Y. Ohta, K. Sugimoto, J. Kim, A. Fujiwara, S. Pyon, K. Kudo, and M. Nohara, J. Phys. Soc. Jpn. **83**, 033701 (2014).

[2] G. L. Pascut, K. Haule, M. J. Gutmann, S.A. Barnett, A. Bambardi, S. Artyukhin, T. Birol, D. Vanderbilt, J. J. Yang, S-W. Cheong, and V. Kiryukhin, Phys. Rev. Lett. **112**, 086402 (2014).

[3] S. Pyon, K. Kudo, and M. Nohara, Physica C **494**, 80-84 (2013)

[4] P. Dudin, P. Lacovig, C. Fava, E. Nicolini, A. Bianco, G. Cautero, and A. Barinov, J. Synchrotron Rad. **17**, 445 (2010).

[5] M. Marsi, L. Casalis, L. Gregoratti, S. Gunther, A. Kolmakov, J. Kovac, D. Lonza, and M. Kiskinova, J. Electron Spectrosc. Relat. Phenom. **84**, 73 (1997).

[6] D. Ootsuki, S. Pyon, K. Kudo, M. Nohara, M. Horio, T. Yoshida, A. Fujimori, M. Arita, H. Anzai, H. Namatame, M. Taniguchi, N. L. Saini, and T. Mizokawa, J. Phys. Soc. Jpn. **82**, 093704 (2013).

[7] K.-T. Ko, H.-H. Lee, D.-H. Kim, J.-J. Yang, S.-W. Cheong, M.J. Eom, J.S. Kim, R. Gammag, K.-S. Kim, H.-S. Kim, T.-H. Kim, H.-W. Yeom, T.-Y. Koo, H.-D. Kim, and J.-H. Park Nature Communications **6**, 7342 (2015)

[8] Kyoo Kim, Sooran Kim, K. -T. Ko, Hwangho Lee, J. -H. Park, J. J. Yang, S. -W. Cheong, and B. I. Min, Phys. Rev. Lett. **114**, 136401(2015).

[9] T. Toriyama and Y. Ohta, private communication.

[10] T. Machida, Y. Fujisawa, K. Igarashi, A. Kaneko, S. Ooi, T. Mochiku, M. Tachiki, K. Komori, K. Hirata, and H. Sakata, Phys. Rev. B **88**, 245125 (2013).

[11] K. Homma and F. Izumi, J. Appl. Crystallogr. **44**, 1272 (2011).

Chapter 7

Anisotropic superconducting gap of $Ir_{1-x}Pt_xTe_2$

7.1 Introduction

In this section, we describe the superconducting gap properties of $Ir_{1-x}Pt_xTe_2$, which belongs to the weak-coupling regime. The geometry of Fermi surfaces for $Ir_{1-x}Pt_xTe_2$ strongly depends on the spin-orbit interaction, as we discussed in Chapter 3. The strong spin-orbit interaction induces the entanglement between the spin and orbital parts of electrons and may cause an exotic superconducting state. On the other hand, the superconductivity is deeply related to the structural phase transition, showing a dome-like phase diagram. The dome like phase diagram is also observed in the high-T_c cuprates, iron-based pnictides or chalcogenides, and heavy Fermion compounds which exhibit exotic superconductivity. The superconducting gap structure of Ir_{1-x} Pt_x Te_2 has been studied by thermal conductivity and scanning tunneling microscopy/spectroscopy (STM/STS) [1,2]. The thermal conductivity measurement shows that the field dependence of residual linear term κ_0/T is similar to that of s-wave superconductor $Cu_{0.06}TiSe_2$, suggesting nodeless superconductivity in Ir_{1-x} Pt_x Te_2 [1]. This is consistent with the superconducting gap measurement of $Ir_{0.95}Pd_{0.05}Te_2$ by the STM/STS measurements [2]. These measurements indicate a nodeless s-wave superconductivity for doped $IrTe_2$. In order to investigate the superconducting gap, we performed the low-temperature and high-energy resolution laser ARPES at Shin group in ISSP, University of Tokyo.

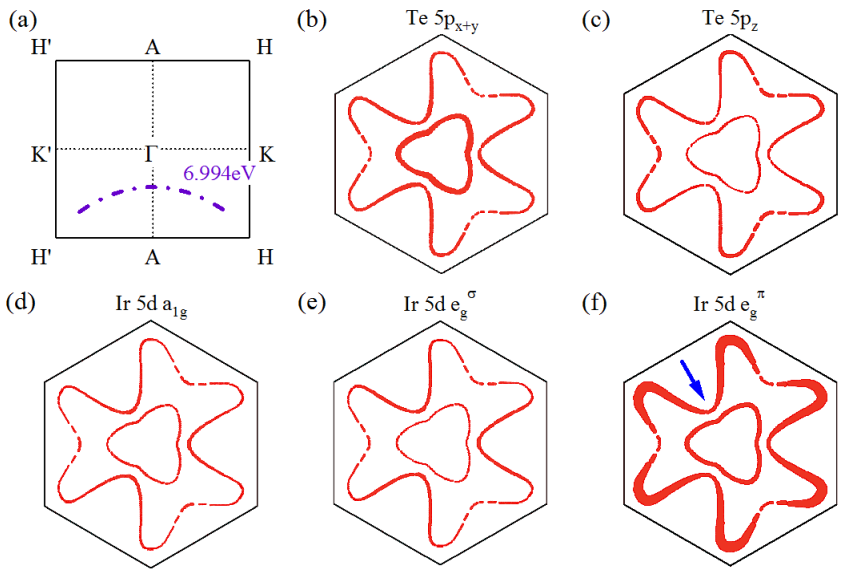

Figure 7.1: (a) Brillouin zone of high temperature phase. The dots curve corresponds to the Fermi surface map taken at $h\nu = 6.994$ eV. Orbital-resolved Fermi surface corresponding to Fermi surface map taken at $h\nu = 6.994$ eV. (b) Te $5p_{x+y}$, (c) Te $5p_z$, (d) Ir $5d$ a_{1g}, (e) Ir $5d$ e_g^σ, and (f) Ir $5d$ e_g^π, respectively [16].

7.2 Experiment

Single crystal samples of $Ir_{0.95}Pt_{0.05}Te_2$ (T_c= 3.1K) were prepared using a self-flux method [3,4]. Laser-ARPES measurements were performed at Shin group in Institute for Solid State Physics (ISSP), University of Tokyo using a VUV-laser of $h\nu = 6.994$ eV as a photon source. The photon energy $h\nu = 6.994$ eV corresponds to k_z located at the middle between Γ and A points in the Brillouin zone of the high temperature phase as shown in Fig. 7.1 (a). Figures 7.1 (b)-(f) show the orbital-resolved Fermi surfaces for the corresponding k_z value. The outer and inner Fermi surfaces mainly consist of the Ir $5d$ e_g^π and the Te $5p_{x+y}$ orbitals, respectively. The energy resolution and angular resolution were set to 470 μeV and $\sim 0.1°$, respectively. The values of energy resolution and sample temperature were confirmed from fitting the Fermi-edge of sample convoluted by a Gaussian with full width at half maximum. The base pressure of the spectrometer for Laser-ARPES instrument was in the 10^{-11} Torr range. The single crystal of $Ir_{0.95}Pt_{0.05}Te_2$ which was oriented by *ex situ* Laue measurements, was cleaved at 2.5K under the ultrahigh vacuum and the spectra were acquired within 8 hours after the cleavage.

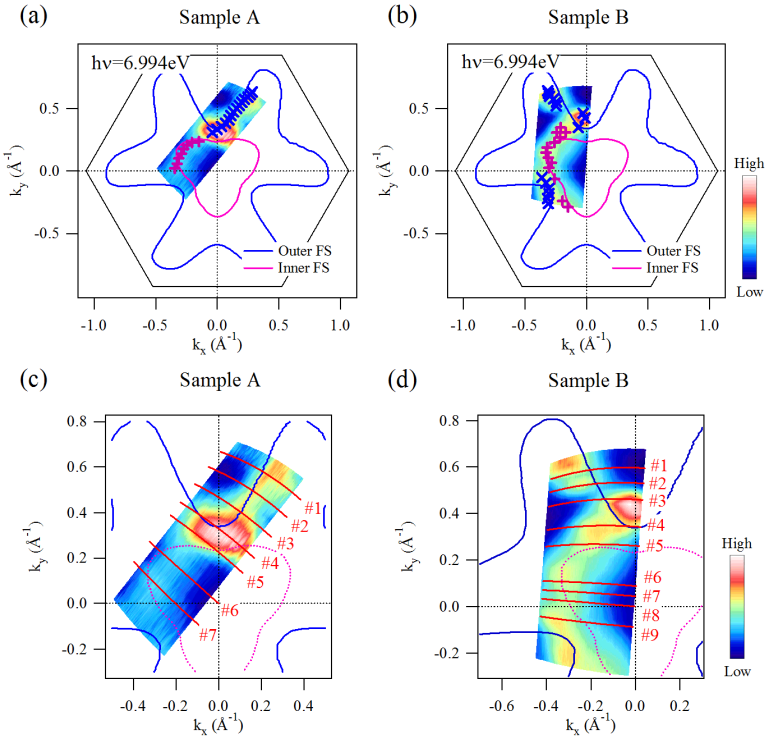

Figure 7.2: Fermi surface maps of $Ir_{0.95}Pt_{0.05}Te_2$ taken at $h\nu$ = 6.994eV for sample A (a) and sample B (b), respectively. Solid lines indicate the Fermi surfaces obtain from the band structure calculation. The blue and pink markers indicate the positions of k_F for the outer and inner Fermi surfaces, respectively. Expanded Fermi surface maps of $Ir_{0.95}Pt_{0.05}Te_2$ for sample A (c) and sample B (d), respectively. The integration energy window is ±5 meV from E_F.

7.3 Results and discussion

We performed the supercoducting gap measurements on the inner and outer Fermi surfaces to investigate Fermi surface dependence of the superconducting gap structure of $Ir_{0.95}Pt_{0.05}Te_2$. The Fermi surface maps of $Ir_{0.95}Pt_{0.05}Te_2$ taken at $h\nu$ = 6.994 eV are displayed in Figs. 7.2 (a) and (b). The pink and blue markers indicate the position of k_F for the inner and outer Fermi surfaces. The outer and inner Fermi surfaces are clearly observed, which is consistent with the prediction of band structure calculation with the spin-orbit interaction. Figure 7.3 shows the momentum distribution curves (MDCs) and the band dispersions corresponding to the cuts in Figs. 7.2 (c) and (d). The positions of Fermi momentum (k_F) for the inner and outer Fermi surfaces are determined by fitting MDCs to the Lorentzians as shown in Fig. 7.3. The energy distribution curves (EDCs) at k_F for the inner and outer Fermi surfaces

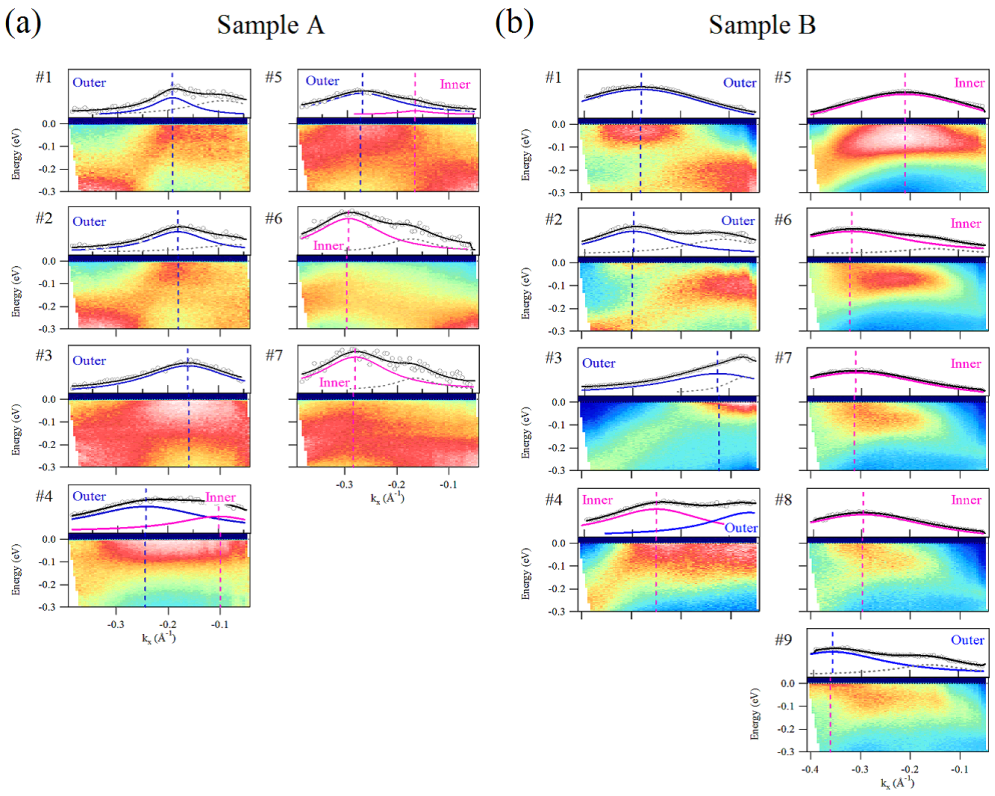

Figure 7.3: Momentum disribution curves (MDCs) at E_F and band dispersions of $Ir_{0.95}Pt_{0.05}Te_2$ taken at $h\nu = 6.994$eV for sample A (a) and sample B (b) along the cuts shown in Figs. 7.2 (c) and (d). Each MDC was fitted to Lorentzians (overlaid black lines).

taken at 1.8K and 5K are shown in Figs. 7.4 (a) and (c). The leading-edge is shifted below T_c, whereas the coherent peak of superconducting state is not obviously observed for all k_F. The EDCs were symmetrized with respect to E_F in Figs. 7.4 (c) and (e). The symmetrized EDCs of the inner and outer Fermi surfaces show the valley structures at E_F, indicating the superconducting gap opening with some anisotropy in the gap size. There are several methods for analytically determining the size of the superconducting gap in ARPES study. For example, a fitting method using Dynes' function or BCS spectral function, a symmetrization method, a leading-edge shift of EDCs, and a crossing point between the EDCs below and above T_c are well-known. However, the weak coherent peak makes it difficult to estimate the size of superconducting gap. Therefore, we examined the fitting method, the symmetrization method, and the crossing energy method in order to quantify the size of superconducting

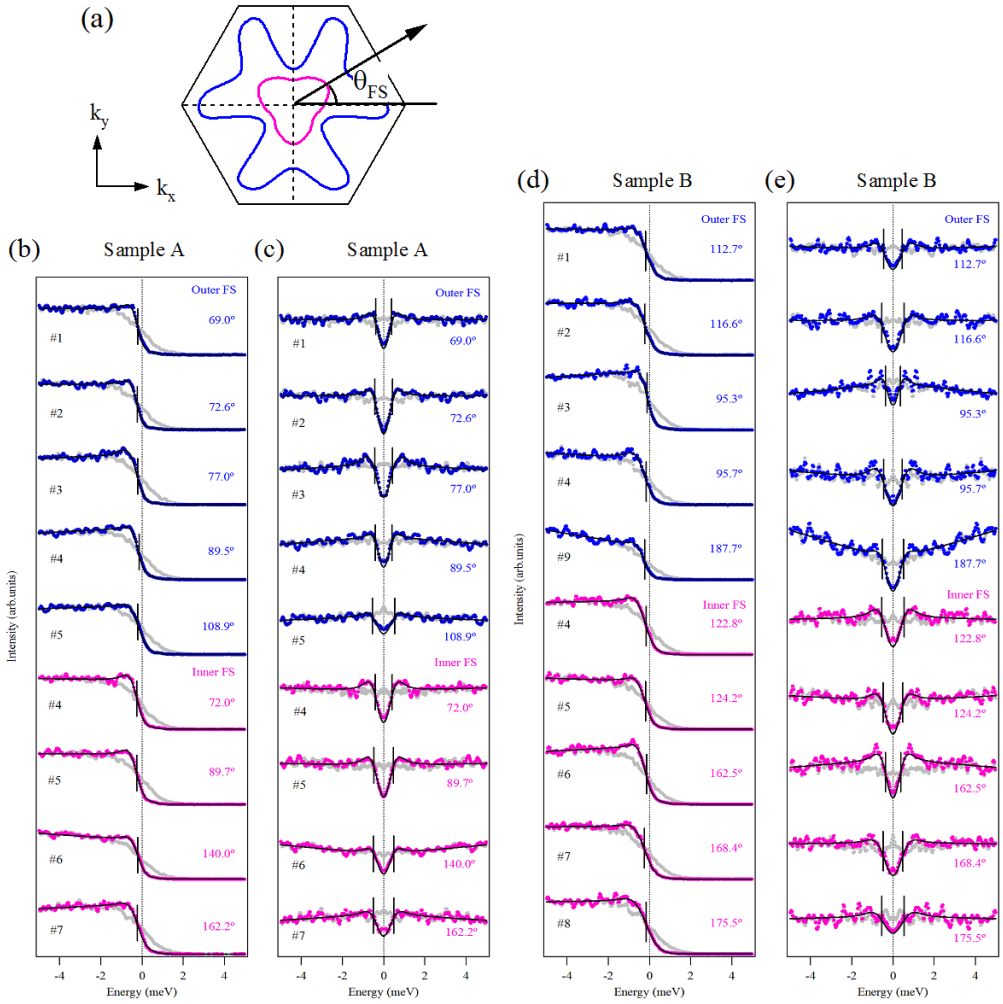

Figure 7.4: (a) Fermi angle is defined so that the Γ-K (A-H) direction is $\theta_{FS} = 0$. EDCs and symmetrised EDCs at k_F for (b),(c) sample A and (d),(e) sample B, respectively.

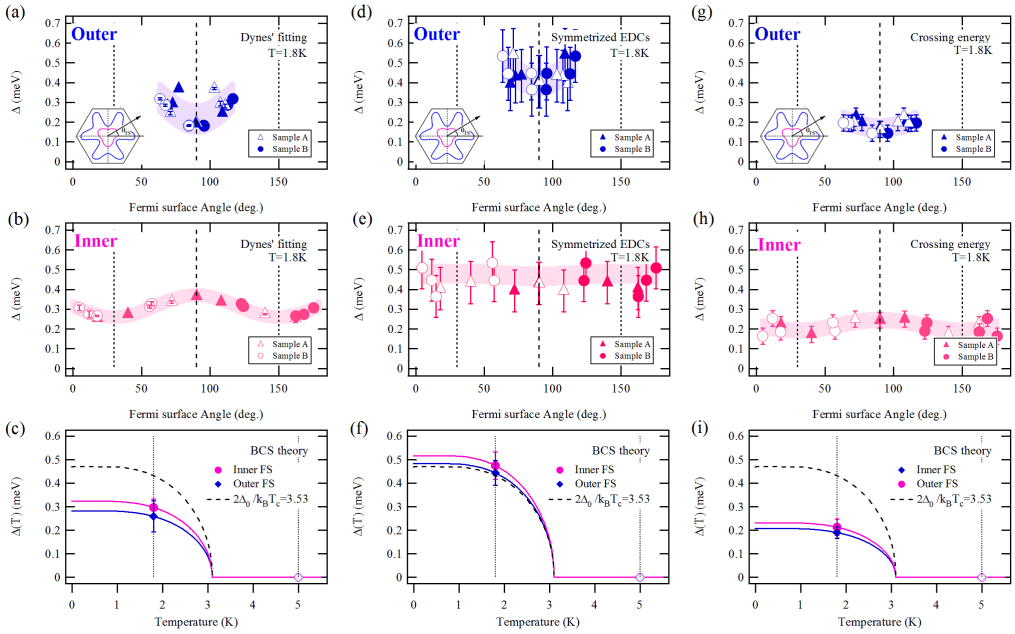

Figure 7.5: (a),(b) Superconducting gap sizes of the inner and outer Fermi surfaces derived from the fitting to Dynes' function, plotted as a function of Fermi surface angle. The solid circles are obtained from Dynes' fitting of EDCs and the open circles are symmetrized by taking into account the hexagonal symmetry. (c) Superconducting gap sizes and BCS curves for the inner and outer Fermi surfaces estimated by ARPES. The dashed line indicates the BCS curves assuming the BCS ratio $2\Delta_0/k_BT_c = 3.53$.

gap. The Dynes' function is defined by

$$D(E, \Delta, \Gamma) = Re\left[\frac{E - i\Gamma}{\sqrt{(E - i\Gamma)^2 - \Delta^2}}\right]. \tag{7.1}$$

where Δ is the superconducting gap, Γ is the phenomenological broadening factor. The Dynes' function reflects the total density of states and generally used in the STM measurement [5]. Compared with Dynes' function, the fitting result using the BCS spectral function does not converge to reasonable values. Therefore, we used Dynes' function. The results of Dynes' fitting are indicated by the solid line in Fig. 7.4. The value of fitting parameter Γ is set to $\sim 0.1\Delta$.

In Fig. 7.5, the superconducting gap sizes of the inner and outer Fermi surfaces are plotted as a function of θ_{FS} which are obtained by Dynes' fitting (a), the symmetrization method (b), and the crossing point (c), respectively. The solid circles represent the estimated values from EDCs and the open circles are symmetrized by taking into account the hexagonal symmetry. The superconducting gap sizes of the inner Fermi surface and the outer Fermi surface

Table 7.1: Superconducting gap sizes and BCS ratios for the inner and outer Fermi surfaces determined by ARPES. k_B is the Boltzmann constant.

Dynes' fitting	Inner FS	Outer FS
Δ_0(meV)	0.32 ± 0.04	0.28 ± 0.07
$2\Delta_0/k_BT_c$	2.40 ± 0.37	2.10 ± 0.75

Symmetrized EDC	Inner FS	Outer FS
Δ_0(meV)	0.52 ± 0.05	0.48 ± 0.06
$2\Delta_0/k_BT_c$	3.89 ± 0.37	3.59 ± 0.50

Crossing Energy	Inner FS	Outer FS
Δ_0(meV)	0.23 ± 0.03	0.21 ± 0.03
$2\Delta_0/k_BT_c$	1.72 ± 0.22	1.57 ± 0.22

exhibit the finite values within the measured region which sufficiently covers the inner Fermi surface. This excludes the nodal superconducting gap and is consistent with the thermal conductivity measurement [1]. Interestingly, the superconducting gap size of the outer Fermi surface is suppressed around $\theta_{FS} = 90°$, indicating the anisotropic superconducting gap. This reduction of the superconducting gap in the outer Fermi surface is reproduced in the other procedures. Here, it should noted that we cannot exclude the small anistorpic superconducting gap of the inner Fermi surface because of the finite error bar.

Considering the conventional phonon-mediated superconductivity, the superconducting gaps of the inner Fermi surface and the outer Fermi surface should be isotropic, due to the isotropic electron-phonon coupling. However, the observed superconducting gap shows anisotropy. In 2H-type transition-metal dichalcogenide $NbSe_2$, the anisotropic superconducting gap is also observed, which exhibits CDW with $T_{CDW} \sim 33$ K and superconductivity with $T_c = 7.2$ K [7–9]. The anisotropic superconducting gaps are observed in the outer Fermi surfaces derived from the Nb $4d$ orbitals. The ratio of $\Delta_{min}/\Delta_{max}$ ∼0.3 for $NbSe_2$ is larger than that of $\Delta_{min}/\Delta_{max}$ ∼0.5 for $Ir_{0.95}Pt_{0.05}Te_2$, where Δ_{min} and Δ_{max} are the minimum and maximum values of the superconducting gap, respectively. This indicates that the superconducting gap structure of $Ir_{0.95}Pt_{0.05}Te_2$ is less anisotropic than that of $NbSe_2$. Interestingly, the superconducting gap of $NbSe_2$ does not open on the inner Fermi surface derived from the Se $4p$ orbitals, which is in contrast to the finite superconducting gaps of $Ir_{0.95}Pt_{0.05}Te_2$ on the inner Fermi surface derived from the Te $5p$ orbitals.

Rahn *et al.* have suggested that the anisotropy of superconducting gap for $NbSe_2$ is partially reflected by the k-dependence of the electron-phonon coupling parameter λ, which is obtained from the kink structure of ARPES [9]. However, the kink structures of $Ir_{0.95}Pt_{0.05}Te_2$ are not observed in our ARPES measurements.

The superconducting gap measurement gives the superconducting gap sizes for the inner and outer Fermi surfaces, respectively. The estimated values using the different procedures are summarized in table 7.1. It should be noted that the estimations of the superconducting gap value are underestimated by using the Dynes' method and the crossing energy. Therefore, the superconducting gap size obtained from the symmetrized method is relatively reliable in spite of the large error bar. The large error bar is due to the absence of the sharp coherent peak. Assuming BCS theory, we estimated the superconducting gaps Δ_0. The BCS curves for each FS are displayed in Fig. 7.5 (f). The values of $2\Delta_0/k_BT_c$, which indicate the coupling strength of the Cooper pairs, are estimated for the inner Fermi surface and the outer Fermi surface, respectively. These values obtained from the symmetrized method are in agreement with the STS measurement of $Ir_{0.95}Pd_{0.05}Te_2$ [2] and comparable to the BCS ratio 3.53, indicating the weak-coupling superconductivity of $Ir_{0.95}Pt_{0.05}Te_2$.

Based on our observation, we discuss the origin of the anisotropic superconducting gap of $Ir_{0.95}Pt_{0.05}Te_2$. The superconducting gap of the inner Fermi surface is more isotropic than that of the outer Fermi surface. Cheong *et al.* have proposed that the charge susceptibility exhibits the peak structure corresponding to the nesting vector $q = (1/5, 0, -1/5)$ in order to explain the origin of the structural phase transition of $IrTe_2$ [10]. (The several experiments have pointed out that the structural phase transition of $IrTe_2$ is not driven by CDW instability [3, 11, 12].) Figure 7.6 shows the one example of the Fermi surface nesting between the inner and outer Fermi surfaces, corresponding to $q = (1/5, 0, -1/5)$. The inner Fermi surface at $k_z = 2/5$ exhibits the good nesting to the outer Fermi surface at $k_z = 4/5$. On the other hand, the outer Fermi surface at $k_z = 2/5$ is strongly warped around $\theta_{FS} = 90°$. As a result, the nesting condition of the outer Fermi surface gets worse in going from $\theta_{FS} = 0°$ to 90°. The imperfect Fermi surface nesting enhances the charge fluctuation, which induces the anisotropic superconducting gap.

Incidentally, the extended s-wave superconductivity, such as $s_{\pm}$-wave and s_{++}-wave has been discussed in the iron-based superconductor [13–15]. In $Ir_{0.95}Pt_{0.05}Te_2$, the outer and inner Fermi surfaces are also disconnected to each other, and mainly constructed from the Ir $5d$ e_g^{π} and the Te $5p_x + 5p_y$, respectively. One can speculate that the inter-orbital scattering would enhance the charge and/or orbital fluctuations and induce the anisotropic superconducting

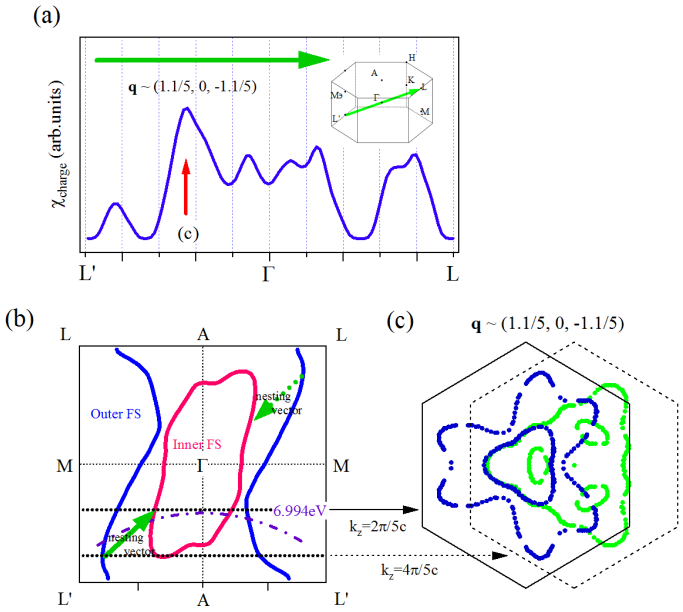

Figure 7.6: (a) Charge susceptibility $\chi_{Charge}(q)$ along L'-K-L corresponding to the superstructure (1/5, 0, -1/5) calculated by Yang *et al.* [10]. The red arrow indicates the dominant peak at q∼(1.1/5, 0, -1.1/5). (b) Fermi surface in k_z - k_y (ΓMLA) plane. The green arrow indicates the nesting vector corresponding to the dominant peak in (a). (c) The one example of the Fermi surface nesting.

gap. Furthermore, the effects of the Ir 5*d* and Te 5*p* spin-orbit interactions are emphasized in the region where the inner and outer bands close to each other as we discussed in Chapter 5. The anisotropic superconducting gap would be induced by the inter or intra band interaction and/or the spin-orbit interaction of Ir 5*d* and Te 5*p* orbitals.

7.4 Summary

We have investigated the superconducting gap structure of $Ir_{0.95}Pt_{0.05}Te_2$ using the low-temperature and high energy resolution laser angle-resolved photoemission spectroscopy. We observed the nodeless anisotropic superconducting gap of the inner and outer Fermi surfaces, which is consistent with the thermal conductivity measument [1]. The value of $2\Delta_0/k_BT_c$ is comparable to the BCS ratio, indicating the weak-coupling superconductivity. Our observation of the superdoncudicing gap structure indicates the unconventional superconductivity in $Ir_{0.95}Pt_{0.05}Te_2$.

References

[1] S. Y. Zhou, Z. L. Li, B. Y. Pan, X. Qiu, J. Pan, X. C. Hong, Z. Zhang, A. F. Fang, N. L. Wang, and S. Y. Li, EPL **104**, 27010 (2013)

[2] D. J. Yu, F. Yang, Lin Miao, C. Q. Han, Meng -Yu Yao, Fengfeng Zhu, Y. R. Song, K. F. Zhang, J. F. Ge, X.Yao, Z. Q. Zou, Z. J. Li,B. F. Gao, Canhua Liu, D. D. Guan, C. L. Gao, Dong Qian, and Jin-feng Jia, Phys. Rev. B **89**, 100501 (R) (2014)

[3] A. F. Fang, G. Xu, T. Dong, P. Zheng, and N. L. Wang, Sci. Rep. **3**, 1153 (2013).

[4] S. Pyon, K. Kudo, and M. Nohara, Physica C **494**, 80-84 (2013)

[5] R. C. Dynes, V. Narayamurti, and J. P. Garno, Phys. Rev. Lett. **41**, 1509 (1978)

[6] K. Okazaki, Y. Ota, Y. Kotani, W. Malaeb, Y. Ishida, T. Shimojima, T. Kiss, S. Watanabe, C.-T. Chen, K. Kihou, C. H. Lee, A. Iyo, H. Eisaki, T. Saito, H. Fukazawa, Y. Kohori, K. Hashimoto, T. Shibauchi, Y. Matsuda, H. Ikeda, H. Miyahara, R. Arita, A. Chainani, and S. Shin, Science **337**, 1314 (2012).

[7] T Yokoya, T Kiss, A Chainani, S Shin, M Nohara, and H Takagi, Science **294**, 5551, 2518-2520 (2001)

[8] T. Kiss, T. Yokoya, A. Chainani, S. Shin, T. Hanaguri, M. Nohara, and H. Takagi, Nature Physics **3**, 720-725 (2007)

[9] D. J. Rahn, S. Hellmann, M. Kallne, C. Sohrt, T. K. Kim, L. Kipp, and K. Rossnagel, Phys. Rev. B **85**, 224532

[10] J. J. Yang, Y. J. Choi, Y. S. Oh, A. Hogan, Y. Horibe, K. Kim, B. I. Min, and S-W. Cheong, Phys. Rev. Lett. **108**, 116402 (2012).

[11] K. Mizuno, K. Magishi, Y. Shinonome, T. Saito, K. Koyama, N. Matsumoto, and S. Nagata, Physica B **312**, 818 (2002).

[12] D. Ootsuki, S. Pyon, K. Kudo, M. Nohara, M. Horio, T. Yoshida, A. Fujimori, M. Arita, H. Anzai, H. Namatame, M. Taniguchi, N. L. Saini, and T. Mizokawa, J. Phys. Soc. Jpn. **82**, 093704 (2013).

[13] I. I. Mazin, D. J. Singh, M. D. Johannes, and M. H. Du, Phys. Rev. Lett. **101**, 057003 (2008).

[14] K. Kuroki, S. Onari, R. Arita, H. Usui, Y. Tanaka, H. Kontani, and H. Aoki, Phys. Rev. Lett. **101**, 087004 (2008).

[15] S. Onari and H. Kontani, Phys. Rev. Lett. **103** 177001 (2009).

[16] T. Toriyama and Y. Ohta. private communication.

Chapter 8

Concluding remarks

In the preceding chapters, we have presented core-level x-ray photoemission spectroscopy (XPS) and angle-resolved photoemission spectroscopy (ARPES) of $Ir_{1-x}Pt_xTe_2$, which exhibits the stripe-type charge order with Ir-Ir dimers and the superconductivity derived from Te $5p$ and Ir $5d$ orbitals.

The XPS shows that the valences of Ir and Te are close to Ir^{3+} and $Te^{1.5-}$, respectively. This indicates the strong hybridization due to the small charge transfer energy. According to the small charge transfer energy, the Te $5p$ orbitals contribute to the density of states near Fermi level as well as the Ir $5d$ orbitals. The Ir $4f$ core-level splitting is clearly observed in the low temperature phase, suggesting the Ir^{3+}/Ir^{4+} charge ordering and its complete suppression by Pt doping. Therefore, it is expected that both of the Ir $5d$ and Te $5p$ orbitals govern the physical properties of $Ir_{1-x}Pt_xTe_2$, such as the stripe-type charge order with Ir-Ir dimers and superconductivity. In fact, the photon energy dependence of ARPES shows the three-dimensional Fermi surfaces in spite of its layered structure at the high temperature phase. The three-dimensional Fermi surfaces are due to the strong Te $5p$ - $5p$ transfer integrals along the out-of-plane direction and the strong hybridization between the Te $5p$ and Ir $5d$ orbitals.

As a result of Pt doping, the structural phase transition is suppressed and superconductivity appears. The observed Fermi surfaces of $Ir_{0.95}Pt_{0.05}Te_2$ stably exist to low temperature, while Pt doping introduces the electrons into the Te $5p$ and Ir $5d$ orbitals. This indicates that the Fermi surfaces of high temperature phase derived from the Ir $5d$ and Te $5p$ orbitals are deeply related to the appearance of superconductivity. Moreover, the Te $5p$ and Ir $5d$ spin-orbit interactions are effective in the region where the inner and outer bands are close to each other and may introduce the exotic superconducting state.

At the low temperature phase, the observed Fermi surfaces and band dispersions include both the surface state and the bulk state. As for the surface

state, the one-dimensional band dispersions exhibit the kink structure and its branches, suggesting the realization of the novel one-dimensional electronic state. On the other hand, the bulk electronic structure basically agrees with the band structure calculation with superstructure $q_{1/5}$. The drastic change of the dimensionality with symmetry breaking indicates that the stripe-type charge ordering is governed by the local Ir - Ir, Ir - Te, and Te - Te bonding.

Since $IrTe_2$ undergoes a first order phase transition with symmetry breaking, domain formation is expected. We have performed angle-resolved photoemission microscopy in order to investigate the spatial distribution of the electronic structure accompanied by structural phase transition. At the low temperature phase, the novel stripy domains are clearly observed and consist of the bright and dark regions. The bright and dark regions can be assigned to the two phases with and without the stripe-type charge order, respectively. These two phases have different volumes and the stripy domains of the stripe-charge order state is under anisotropic strain from the neighboring domains. The strain is expected to enhance the orbital anisotropy of the Te $5p$ and Ir $5d$ orbitals and to align the direction of charge stripe.

Finally, we have performed the superconducting gap measurements on the inner and outer Fermi surfaces in order to investigate the Fermi surface dependence of the superconducting gap structure of $Ir_{0.95}Pt_{0.05}Te_2$. Our observation of the superconducting gap structure clearly shows the anisotropic superconducting gap of $Ir_{0.95}Pt_{0.05}Te_2$. The anisotropic superconducting gap of $Ir_{0.95}Pt_{0.05}Te_2$ would be induced by the inter or intra band interaction and/or the spin-orbit interaction of Ir $5d$ and Te $5p$ orbitals.

List of publications

1. D. Ootsuki, Y. Wakisaka, S. Pyon, K. Kudo, M. Nohara, M. Arita, H. Anzai, H. Namatame, M. Taniguchi, N. L. Saini, T. Mizokawa,
Orbital Degeneracy and Peierls Instability in Triangular Lattice Superconductor $Ir_{1-x}Pt_xTe_2$
Physical Review B **86**, 014519 (2012)

2. T. Sudayama, D. Ootsuki, Y.Wakisaka, T. Mizokawa, N. L. Saini, M. Arita, H. Namatame, M. Taniguchi, T. Noji, and Y. Koike,
Anomalous Momentum Dependence of the Multiband Electronic Structure of $FeSe_{1-x}Te_x$ *Superconductors Induced by Atomic Disorder*,
Journal of Physical Society of Japan **82**, 053705 (2013).

3. *D. Ootsuki, S. Pyon, K. Kudo, M. Nohara, M. Horio, T. Yoshida, A. Fujimori, M. Arita, H. Anzai, H. Namatame, M. Taniguchi, N. L. Saini, T. Mizokawa,
Electonic Structure Reconstruction by Orbital Symmetry Breaking in $IrTe_2$
Journal of Physical Society of Japan **82**, 0093704 (2013).

4. M. Fukuzawa, D. Ootsuki, T. Mizokawa,
Spin-Charge-Orbtal Ordering in Hollandite-Type Maganites Studied by Model Hatree-Fock Calculation,
Journal of Physical Society of Japan **82**, 074708 (2013).

5. T. Sugimoto, D. Ootsuki, T. Mizokawa,
Impact of Local Lattice Disorder on Spin and Orbital Orders in $Ca_{2-x}Sr_xRuO_4$,
Journal of Physical Society of Japan **82**, 104714 (2013)

6. M. Oiwake, D. Ootsuki, T. Noji, T. Hatakeda, Y. Koike, M. Horio, A.Fujimori, N. L.Saini, T. Mizokawa,
Electronic Structure and Phase Separation of Superconducting and Non-superconducting $K_xFe_{2-y}Se_2$ *Revealed by X-ray Photoemission spectroscopy*,
Physical Review B **88**, 224517 (2013)

7. *D. Ootsuki, T. Toriyama, M. Kobayashi, S. Pyon, K. Kudo, M. Nohara, T. Sugimoto, T. Yoshida, M. Horio, A. Fujimori, M. Arita, H. Anzai, H. Namatame, M. Taniguchi, N. L. Saini, T. Konishi, Y. Ohta, T. Mizokawa, *Important Roles of Te5p and Ir 5d Spin-orbit Interactions on Multi-band Electronic Structure of Triangular Lattice Superconductor* $Ir_{1-x}Pt_xTe_2$, Journal of Physical Society of Japan **83**, 033704 (2014)

8. *D. Ootsuki, T. Toriyama, S. Pyon, K. Kudo, M. Nohara, K. Horiba, M. Kobayashi, K. Ono, H. Kumigashira, T. Noda, T. Sugimoto, A. Fujimori, N. L. Saini, T. Konishi, Y. Ohta, T. Mizokawa
Te 5p Orbitals Bring Three-dimensional Electronic Structure to Two-dimensional $Ir_{0.95}Pt_{0.05}Te_2$,
Physical Review B **89**, 104506 (2014)

9. K. Sawada, D. Ootsuki, K. Kudo, D. Mitsuoka, M. Nohara, T. Noda, K. Horiba, M. Kobayashi, K. Ono, H. Kumigashira, N. L. Saini, T. Mizokawa,
Coexistence of Bloch Electrons and Glassy Electrons in $Ca_{10}(Ir_4As_8)(Fe_{2-x}Ir_xAs_2)_5$ *revealed by angle-resolved Photoemission Spectroscopy*,
Physical Review B (R) **89**, 220508 (R) (2014)

10. D. Ootsuki, K. Takubo, K. Kudo, H. Ishii, M. Nohara, N. L. Saini, R. Autarto, F. He, T. Z. Regier, G. Levy, G. A. Sawatzky, A. Damascelli, T. Mizokawa,
Effect of Pt Substitution on the Electronic Structure of $AuTe_2$,
Physical Review B **90**, 144515 (2014)

11. K. Takubo, R. Comin, D. Ootsuki, T. Mizokawa, H. Wadati, Y. Takahashi, G. Shibata, A. Fujimori, R. Sutarto, F. He, S. Pyon, K. Kudo, M. Nohara, G. Levy, I. Elfmov, G. A. Sawatzky, A. Damascelli,
Bond-Order and the Role of Ligand States in Stripe-Modulated $IrTe_2$,
Physical Review B **90**, 081104 (R) (2014)

12. M. Bendele, A. Barinov, B. Joseph, D. Innocenti, A. Ladecola, A. Bianconi, H. Takeya, Y. Mizuguchi, Y. Takano, T. Noji, T. Hatakeda, Y. Koike, M. Horio, A. Fujimori, D. Ootsuki, T. Mizokawa, N. L. Saini,
Spectromicroscopy of Electronic Phase Separation in $KxFe_{2-y}Se_2$ *superconductor*,
Scientific Reports **4**, 5592 (2014)

13. N. L. Saini, D. Ootsuki, E. Paris, B. Joseph, A. Barinov, M. Tanaka, Y, Takano, T. Mizokawa,

Electronic structure of $LaO_{1-x}F_xBiSe_2$ (x = 0.18) revealed by photoelectron spectromicroscopy,
Physical Review B **90**, 214517 (2014)

14. D. Ootsuki, N. L. Saini, F. Du, Y. Hirata, K. Ohgushi, Y. Ueda, T. Mizokawa
Coexistence of localized and itnerant electrons in $BaFe_2X_3$ (X=S and Se) revealed by photoemission spectroscopy,
Physical Review B **91**, 014505 (2015)

15. T. Sugimoto, D. Ootsuki, M. Takahashi, C. Morice, Emilio Artacho, S.S. Saxena, E. F. Schwier, M. Zeheng, Y. Kojima, H. Iwasawa, K. Shimada, M. Arita, H. Namatame, M. Taniguchi, N. L. Saini, T. Asano, T. Nakajima, R. Higashinaka, T. D. Matsuda, Y. Aoki, T. Mizokawa
Electronic structure of ferromagnetic and superconducting $CeO_{0.5}F_{0.5}BiS_2$ revealed by angle-resolved photoemission spectroscopy,
Physical Review B (R) **92** 041113 (2015)

16. Y. Yokoyama, D. Ootsuki, T. Sugimoto, H.Wadati, J. Okabayashi, Xu Yang, Fei Du, Gang Chen, T. Mizokawa
Electronic structure of $Li_{1+x}[Mn_{0.5}Ni_{0.5}]_{1-x}O_2$ studied by photoemission and x-ray absorption spectroscopy,
Applied Physics Letter **107**, 033903 (2015)

17. M. Horio, T. Adachi, Y. Mori, A. Takahashi, T. Yoshida, H. Suzuki, L. C. Ambolode, II, K. Okazaki, K. Ono, H. Kumigashira, H. Anzai, M. Arita, H. Namatame, M. Taniguchi, D. Ootsuki, K. Sawada, M. Takahashi, T. Mizokawa, Y. Koike, A. Fujimori
Suppression of the antiferromagnetic pseudogap in the electron-doped high-temperature superconductor by protect annealing,
Nature Communications **7**, 10567 (2016)

∗Publications related to the thesis.

Acknowledgments

Only this part, I would like to use Japanese to express my gratitude.

本学位論文は著者が東京大学大学院理学系研究科物理学専攻博士課程在学中に行った研究をまとめたものです。

指導教官である早稲田大学先進理工学部応用物理学科溝川貴司教授には修士課程からの５年間、研究の世界で右も左もわからない私に研究を一から丁寧に指導して頂き、また海外での研究をはじめとする様々な機会を与えて頂いたことに心から感謝致します。

I would like to thank Prof. Naurang L. Saini for giving me a lot of invaluable opportunities, a lot of effective advice and continuous encouragement throughout this study.

岡山大学大学院自然科学研究科野原実教授、工藤一貴准教授、本学工学系研究科助教卞舜生博士、岡山大学大学院自然科学研究科小林正和氏には私が修士課程入学時より、貴重な試料を提供して頂き、急なお願いにも迅速に対応して頂きました。深く感謝いたします。

広島大学放射光科学センター HiSOR の谷口雅樹教授、生天目博文教授、有田将司技術主任、大阪府立大学大学院工学研究科助教安齋太陽博士には角度分解光電子分光実験につきましてご助言、ご協力を頂きました。特に有田将司技術主任には実験中の要望やトラブルにつきましていつも丁寧に対応して頂き、最高の環境下で実験を行えたと思っております。有難うございました。

高エネルギー加速器研究機構物質構造科学研究所の組頭広志教授、小野寛太教授、堀場弘司准教授、助教小林正起博士には角度分解光電子分光実験につきましてご協力、ご助言を頂きました。深く感謝いたします。

The angle-resolved photoemission microscopy measurements at SPEM beamline in Elettra were supported by Dr. Alexey Barinov, Dr. Mikhail Yablon-

skikh, Dr. Viktor Kandyba, Dr. Juanjuan Jia. I am thankful to them for helping the experiments and for their valuable suggestions.

本学物性研究所辛埴教授、本学新領域創成科学研究科岡崎浩三准教授、本学物性研究所大田由一博士、山本遇哲氏、橋本嵩広氏には辛研究室の世界最高分解能極低温レーザー角度分解光電子分光装置を使用させて頂き、多大なるご協力とご助言を頂きました。T_c=3.1K の超伝導ギャップの観測に成功したときの感動は鮮明に覚えております。心より感謝いたします。

千葉大学大学院理学研究科太田幸則教授、融合科学研究科小西健久准教授、理学研究科鳥山達矢博士にはバンド計算の結果を提供して頂き、また多くのご助言を頂きました。深く感謝いたします。

本学理学系研究科藤森淳教授、京都大学人間・環境学研究科吉田鉄平准教授、本学理学系研究科堀尾眞史氏には投稿論文や広島大学放射光科学センターの実験で多くのご助言とご協力を頂き、投稿論文執筆では多くのコメントを頂きました。深く感謝いたします。

本学物性研究所和達大樹准教授には研究室の移転に伴い本学での指導教官を引き受けて頂き、深く感謝いたします。
また、本学物性研究所田久保耕博士にはカナダでの実験や共同研究で多くのご協力やご助言を頂きました。心より感謝いたします。

溝川研究室の脇坂祐輝博士 (分子科学研究所)、加藤航矢氏、佐藤聖峰氏、追分美代子氏、杉本拓也氏、福沢真氏、李惺薫氏、野田智博氏、横山優一氏、小宮山潤氏、高橋雅也氏、千葉優氏、早稲田大学の学生たちには研究室生活におきまして大変お世話になりました。特に、脇坂祐輝博士には実験や解析手法など様々なことを丁寧に教えて頂きました。深く感謝いたします。本学新領域創成科学研究科福谷文子様、本学物性研究所吉澤泉子様には研究に関わる様々な事務の対応をして頂きました。有難うございました。

I would like to thank all the members of Saini group, Mr. Eugenio Paris, Dr. Boby Joseph, Dr. Antonella Iadecola for a lot of their experimental supports, discussions, and encouragement. I really enjoyed the time I spent with them in Trieste, Rome, Gronoble, and Giove.

学部生のときに物理学の基礎を教えて頂いた東京理科大学理学部和達三樹教授、光電子分光に興味を持つきっかけを与えて頂いた東京理科大学理学部齋藤智彦教授、そして学部から大学院まで物性物理学のゼミの指導役を学外の学生であるにも関わらず快く引き受け、指導して頂いた東京理科大学研究推進機

構総合研究院福山秀敏教授、助教横山健氏に心から感謝致します。特に、横山健氏には週に一度行われるゼミで何時間も私たち学生に親身になって付き合って頂き、私事で悩んでいたときにも気を配って頂きました。この場でお礼申し上げます。本当にお世話になりました。ありがとうございました。

本研究は、日本学術振興会特別研究員制度 DC1 による研究活動費及び経済的支援のもと行われた。

ご多忙にもかかわらず本論文の審査をお引き受け下さった本学物性研究所近藤猛准教授、上床美也教授、理学系研究科小形正男教授、長谷川修司教授、北川健太郎講師に深く感謝いたします。

最後に、自分の進む道を温かく見守り、長い学生生活を支えてくれた家族に心より感謝いたします

平成 28 年 2 月　西早稲田にて
大槻太毅